IPP-Report

MAX-PLANCK-INSTITUT
FÜR PLASMAPHYSIK

Marco Muraca

Reduced Transport Models for a Tokamak Flight Simulator

IPP 2023-03
April 2023

Reduced Transport Models for a Tokamak Flight Simulator

Marco Muraca

München 2023

Reduced Transport Models for a Tokamak Flight Simulator

Marco Muraca

Dissertation
an der Fakultät für Physik
der Ludwig–Maximilians–Universität
München

vorgelegt von
Marco Muraca
aus Rom

München, den 24.02.2023

Erstgutachter: Prof Dr Hartmut Zohm
Zweitgutachter: Prof Dr Harald Lesch
Tag der mündlichen Prüfung: 24.04.2023

Contents

List of Figures

List of Tables

Zusammenfassung

In dieser Arbeit wurde ein schnelles integriertes Transportmodell des Tokamaks entwickelt, das alle relevanten Regionen einbezieht, die an seiner Entwicklung beteiligt sind. Die verwendeten Modelle sind wegen zwei Hauptaspekten attraktiv: Sie basieren auf physikalische Prinzipien, um ihre Zuverlässigkeit zu erhöhen, und sie sind analytisch und erfordern daher eine geringe Rechenzeit. Darüber hinaus stützen sie sich nicht auf vorhandene experimentelle Daten der zu simulierenden Entladung, wodurch man auch neue Entladungen vorhersagen kann. Dennoch werden zum Aufbau der Modelle einige wenige empirische Beobachtungen herangezogen, vor allem im äußeren Plasmabereich, während der Kernbereich vollständig nach First-Principles behandelt wird. Der eingegrenzte Bereich ist in 1,5 D modelliert, während die Scrape-Off-Layer (SOL) eine 0 D-Struktur hat.
Für die Kernregion wurde eine physikbasierte analytische Regression verwendet, basierend auf einer Reihe von Simulationen mit dem Transportmodell TGLF [Staebler 2005 Phys. Plasmas 12 102508]. Die in der Anpassung verwendeten analytischen Formeln basieren auf den bekannten relevanten Mikroinstabilitäten.
Um die Sättigung des Pedestaldrucks im Bereich hohen Confinements zu modellieren, wird ein Modell mit durchschnittlichen Edge-Localized-Modes im Pedestalbereich angewendet, wobei eine feste Pedestalbreite beibehalten wird. Um den L-H-Übergang zu bestimmen, wird eine Skalierung der Ionenleistung, die die Separatrix überquert, verwendet.
Im SOL wurden ein Zweipunktmodell für die Elektronentemperatur und eine 0 D Partikelbilanz für die Speziesdichte an der Separatrix implementiert. In der Partikelbilanz wurde die SOL virtuell in 6 benachbarte Regionen aufgeteilt. In jeder dieser Regionen können lokale Effekte modelliert werden.
Alle Modelle wurden zunächst einzeln in einer eigenständigen Umgebung validiert. Schließlich wurden im Flugsimulator Fenix [Janky et al 2019 Fusion Eng. Des. 146 1926, Fable et al. 2022 Plasma Phys. Control Fusion 64 044002] sechs vollständig integrierte Simulationen eines Low-Confinement-Szenarios (#38898) und fünf High-Confinement-Entladungen (#40446, #40009, #40254, #39977, #39967) durchgeführt, einschließlich Transienten, passend zu den experimentellen Trajektorien. Die beobachteten Unterschiede werden beschrieben. Der Vergleich zwischen simulierten und gemessenen globalen Parametern und der Entwicklung kinetischer Profile zeigt die Qualität der erzeugten Wärmetransportmodelle, die für alle simulierten Fälle gut funktionieren. Diskrepanzen in den Dichteprofilen werden unter bestimmten Bedingungen beobachtet, deren Ursprünge und mögliche Lösungen diskutiert werden.

Abstract

In this thesis, a fast integrated transport model of the tokamak has been developed, involving all the relevant regions that participate in its evolution. The models employed are attractive for two main aspects: they are based on first principles, in order to increase their reliability, and they are analytical, requiring therefore small calculation time. Moreover, they do not rely on existing experimental data of the discharge that needs to be simulated, therefore making it a predictive tool for new discharges. Nevertheless, to build up the models, a few empirical observations are employed, more so in the outer plasma region, whereas the core region is treated fully on first-principles. The confined region is modeled in 1.5D, while the scrape-off layer (SOL) has a 0D structure.
For the core region, a physics-based analytical regression based on a set of simulations with the transport model TGLF [Staebler 2005 Phys. Plasmas 12 102508] has been produced. The analytical formulae used in the fitting are based on the known relevant micro-instabilities.
In order to model the saturation of the pedestal pressure in the high confinement regime, an average edge-localized-modes model is applied in the pedestal region, keeping a fixed pedestal width, and a scaling on the ion power crossing the separatrix is used to determine the L-H transition.
In the SOL, a two-point model for electron temperature and a 0D particle balance for the species density at the separatrix have been implemented. In the particle balance, the SOL has been virtually split in 6 neighbouring regions. In each of these regions local effects can be modeled.
All the models have first been validated individually in a standalone setting. Finally, six fully integrated simulations of a low confinement scenario (#38898), and five high confinement discharges (#40446, #40009, #40254, #39977, #39967), have been performed in the Fenix flight simulator [Janky et al 2019 Fusion Eng. Des. 146 1926, Fable et al 2022 Plasma Phys. Control. Fusion 64 044002], including transients, matching the experimental trajectories. The observed differences are discussed. The comparison between simulated and measured global parameters and kinetic profiles evolution displays the quality of the produced heat transport models, which work well for all the simulated cases. Discrepancies are observed in specific conditions for the density profile, whose origins and possible solutions are discussed.

Chapter 1

Introduction

1.1 Social Context

Most of the human activities have a double face: one is the progress and the continuous pursue of better standard of life; the other one is the cost of it. The distinction between progress and development is a crucial key to understand when the negative consequences of something overcome the benefits. In fact the former leads to improvement of life's conditions or to a society commonly felt as more advanced in a conscious and controlled way, while the latter is a frenetic usage of already existing techniques aimed to the optimization of the common gain [1]. The problem arises from the fact that while the benefits of a specific activity or strategy are immediately evident, the negative consequences due to its unlimited usage are often not known a priori. Therefore the human being has always to find new solutions for new different problems. This applies to some extent also in the scientific research. While a specific theory can successfully explain a series of phenomena, it needs just one case to be proved wrong, so with new conditions a new theory has to be created. In a less abstract way this can apply also to technologies of energy production: while fossil fuels where found to be the best solution during the Industrial Revolution, an integrated scenario which gets different solutions for different purposes is more adapt to modern problems.
One of the most critical issues of the last century is the steep increase of world's population and the consumption-oriented life-style. The solution to the first problem is morally unacceptable. The second problem is really hard to be solved, and it could be not possible or take really long time, so an immediate intervention is necessary, to mitigate its effects. One of the bad consequences of increasing consumption is related to the electrical power that it needs. This is provided from different power plants based on different working principles, but a strong percentage of it is furnished by fossil fuels like carbon, oil and natural gas. These sources produce a strong amount of carbon dioxide, which retains the heat that would otherwise leave the Earth. This has an effect on the power balance of our planet and it could lead in future to an uncontrolled increase of the temperature. A plot of the temporal increase in temperature of the Earth's surface in the last century is

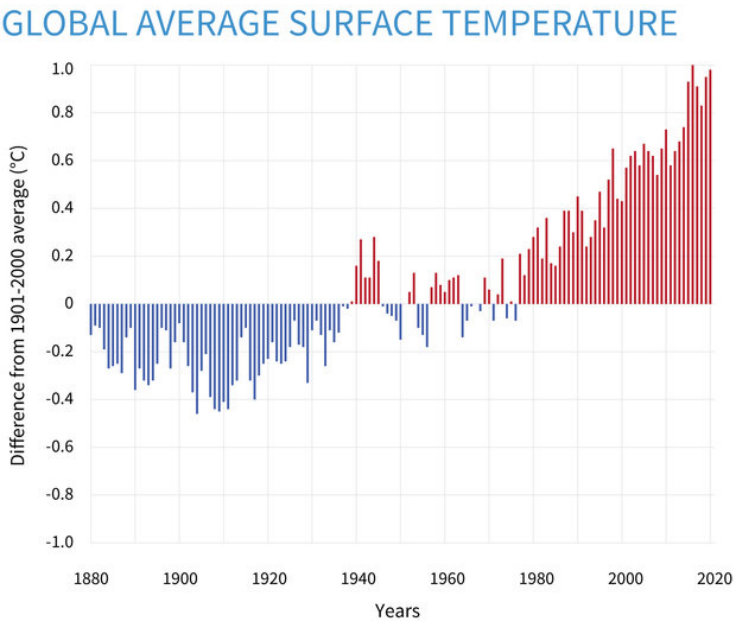

Figure 1.1: Temporal evolution of the averaged temperature of the Earth's surface.

shown in figure 1.1. This process is addressed as Global Warming. In order to avoid this the fossil fuels should be replaced by new sources. However, different technologies show different limitations and problems (e.g. renewable energy can not assure predictable and continuous power production and nuclear fission generates long-term radioactive waste). This means that an integrated scenario of power production based on the coordination of different technologies for different purposes is necessary. In future, inside this scenario, a power plant that could overcome some of the problems related to modern technologies could be based on nuclear fusion. In particular it could get rid of the long-time decaying nuclear waste and improve safety. If some techniques will take place successfully (i.e. T breeding) also the fuel availability will not be a problem. Nuclear Fusion is still in the research phase, so it is hard to realistically predict what will be the issues introduced by it, but it is sure that if correctly developed it will be crucial to reduce the damages related to the increasing consumption and Global Warming.
The "energy problem" is a very complex topic, which includes science, technology, politics, sociology and biology, and the best approach to reduce the negative effects or cut the root of the problem is absolutely not obvious. However, two points require a major focus. First, the nuclear fusion is a solution which should be integrated inside a realistic scenario of different systems for power production, each with its delays related to design and building. Second, the discovery of new strategies to produce electrical power should not promote the increase of the consumption, which is the main problem hidden behind the Global Warming.

1.2 Scientific Context

Nuclear fusion is a process which is known since almost 100 years. The first time it was experimentally reproduced was in 1932 by Mark Oliphant and since then several different technologies based on this reaction were conceived to produce energy in a controlled way. What is the most efficient technology and how to deal with it is still object of study, but the improvements reached along the years are clear. The number of combinations of elements which could generate fusion reactions is wide, but the most known are:

$$D + D = T\,(1.01MeV) + p\,(3.02MeV), \tag{1.1}$$
$$D + D = {}^3He\,(0.82MeV) + n\,(2.45MeV), \tag{1.2}$$

$$D + T = {}^4He\,(3.5MeV) + n\,(14.1MeV), \tag{1.3}$$

$$T + T = {}^4He + 2\,n\,(11.3MeV). \tag{1.4}$$

Any of these reactions has a different threshold of energy which has to be overcome for the nuclear fusion to happen. The reactions $D + D$ and $T + T$ have a lower cross section and a higher energy threshold to be overcome, respect to the case with a mixture of D and T (whose maximum cross section is 2 order of magnitude bigger). This is why this last reaction is more foreseen for future reactors, where the conditions necessary to generate fusion are challenging. Another fusion reaction is between protons, like the one which takes place in the Sun, but this is not relevant in fusion devices because the cross section is negligible respect to the other listed reactions.
In figure 1.2 the cross sections from different nuclear fusion reactions are shown. As one can see the cross section increases with the energy. This means that a future power plant should work at high pressure, then high density and/or high temperature (millions of K). In this condition a state of matter composed by free charges is present, which is called plasma. In a reactor it is hard to sustain such pressure for long time, because there are phenomena which drive energy out from the system. Then one needs to confine the plasma inside the device to mitigate the loss of energy. This confinement can be established through different mechanisms. In the Sun the gravitational field keeps the plasma together, thus favouring the constant happening of fusion reactions. On the Earth this field can not be reproduced, so other techniques have been developed: for example the magnetic confinement is based on a complex configuration of magnetic fields which keeps the plasma in equilibrium. This condition is reached when the radial forces applied on the plasma balance each other; another approach is the inertial confinement, which keeps the plasma energy enclosed in a shock-wave which travels inward single pellets. An important parameter to measure the performance of the plasma is the confinement time, that takes into account the dispersions which affect the plasma. It is the defined as the time by which the energy of the plasma is lost. Its value, multiplied by the ion density, has to overcome a specific threshold given by

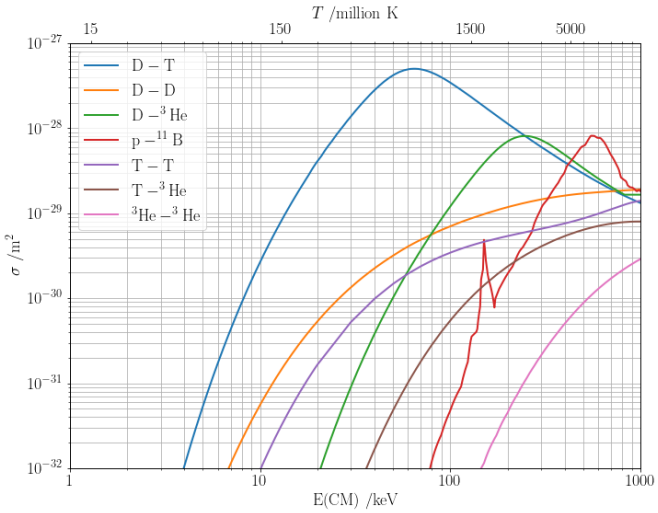

Figure 1.2: Cross sections of nuclear fusion reaction for different reagents mixtures. On x-axis is the energy in keV. The D-T mixture is the most effective, because for the smallest temperature the cross section is already appreciable.

the Lawson's criteria to produce net energy. This threshold is a function of temperature. Thus, by considering the energy of the plasma mainly due to the pressure energy, one can consider the triple product between density, temperature and confinement time as a figure of merit for the fusion performances. A series of configurations and devices were conceived aimed to maximize this product. A plot with different values of the triple product for different temperatures is shown for various experiments in figure 1.3. In the inertial confined system the nT product is maximized (the pellets used as fuel reach densities of the order of $10^{31}m^{-3}$), while the confinement time is really small (the phenomenon is of the order of $10^{-10}s$). The magnetic confinement maximizes the confinement time (of the order of seconds), while the density has a low value ($10^{20}m^{-3}$). This second approach is easier to integrate in a real reactor, because its nature goes in the direction of a stationary system, which can be more easily used to produce constant electrical power.
The main devices based on magnetic confinement are the tokamak, which is shown in figure 1.4, and the stellarator. These devices differ mainly for the fact that the former is axisymmetric, while the latter has no simple symmetry and needs to be modeled in 3D. Also other devices based on different mechanisms exist, but they are not mentioned here. A tokamak is a device with toroidal shape, which aims at containing a plasma undergoing fusion reactions for the longest time possible. In order to do this, the particles have to be confined. As already mentioned, this is done by a complex system of magnetic fields which keeps the plasma compressed radially with respect to the center of the poloidal cross sections of the tokamak. The confinement is assured if the forces induced by the magnetic fields are able to counteract the force exerted by the pressure gradient. This equilibrium condition can be described by the Grad-Shafranov equation [2]. The total magnetic field

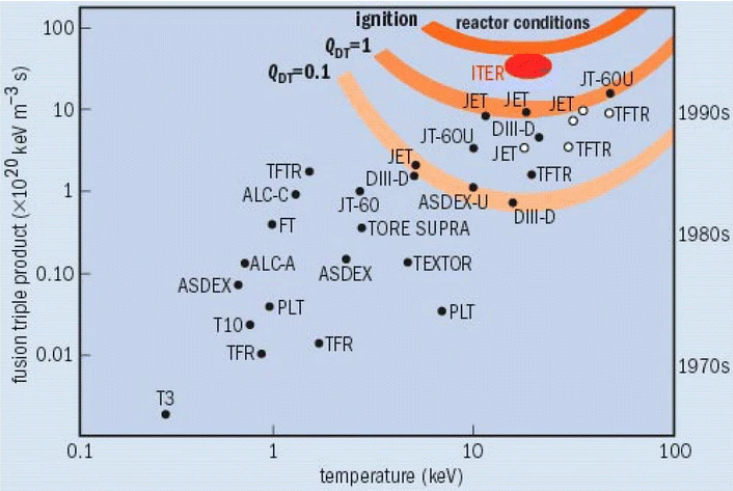

Figure 1.3: Triple product for different experiments. On x-axis is the temperature in keV. Q is the fusion gain, which is defined as the ratio between the produced fusion power and the input power used to obtain it.

can be decomposed in 2 main components, the toroidal field, which is produced by coils wrapped around the torus, and the poloidal field which is arising from the current induced in the tokamak, which is driven inductively by a solenoid, combined with other currents which are driven or arise in the plasma. Due to the radial variation of the toroidal magnetic field, during the toroidal revolution the particles experience a drift in the vertical direction together with the spiral motion around the magnetic field lines, which is caused by the Lorentz force applied in presence of a magnetic field. This drift has opposite directions for ions and electrons, thus it generates an electric field, which combined with the toroidal magnetic field, drives the plasma flux outwards. The poloidal component of the magnetic field is here crucial, because it counteracts this effect, that would otherwise cause a loss of the particle confinement. Other components of the magnetic field are generated by the poloidal control coils, which are wrapped toroidally around the torus. These generate a vertical magnetic field to counteract radial differences in the poloidal magnetic field and control the position of the plasma. Such control coils prevent also the plasma from touching the plasma facing components (PFCs). These are technological components which face the plasma inside the vacuum vessel, which is the shell that contains the system. An illustration of the tokamak with the magnetic fields is shown in figure 1.4.

Inside the tokamak, the volume occupied by the plasma can be generally split in two parts, which are the confined and unconfined region. The former refers to the area of the tokamak where the magnetic field lines are closed, keeping the plasma compressed in a toroidal shaped tube. Inside this region there is a more internal zone, usually addressed as core, followed radially by a small zone, called edge. The confined region is crucial because it is where the energy of the plasma is the highest and it generates nuclear fusion. Moreover, if the plasma is well confined in this region for a sufficiently long time, the output

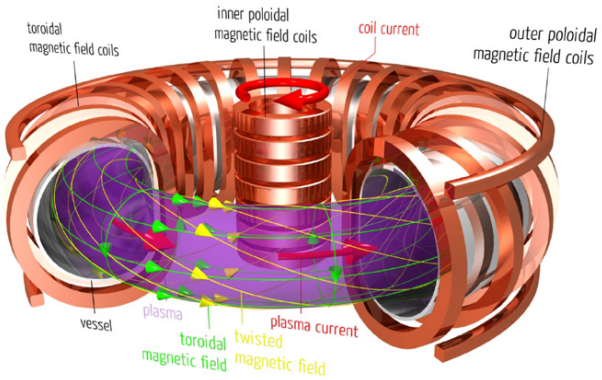

Figure 1.4: Tokamak

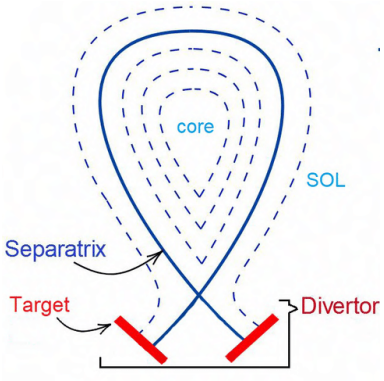

Figure 1.5: Poloidal cross section of a tokamak

power and energy is bigger, which is a crucial thing for a reactor. The unconfined region is the zone which surrounds this tube, where the magnetic field lines are open and terminate on the PFCs. This region is also called scrape-off-layer (SOL). The main PFCs are the wall of the vacuum vessel and the divertor, which is a material whose role is to collect the particles and the heat expelled from the plasma. The magnetic surface which separates the confined region and the SOL is called last closed flux surface (LCFS), or separatrix. A picture of the described geometry with its components in the poloidal cross section is shown in figure 1.5.

Depending on the specific regime and shape of the plasma, the wall or the divertor can collect most of the plasma exhaust, which is the plasma coming out from the confined region. The limiter is a configuration in which the region of the closed flux surfaces intercepts the wall (i.e. the confined region become unconfined). Due to its high temperature the plasma sputters the wall, which releases impurity particles, which can in turn strongly radiate from the plasma, leading to a reduction of the plasma energy content, or in the worst case to a disruption, which is an abrupt interruption of the plasma evolution with almost immediate and complete loss of energy. This configuration is usually followed by

another one, where on the LCFS an X-point is formed [3], [4], which is the point where the poloidal magnetic field is null. Outside the LCFS the field lines are open and they collect the particles and the heat, driving them to the divertor. This is the reason why such condition is known as divertor configuration. The point hit from the particles is called strike point or target. Even though a residual amount of transport perpendicular to the field line is carried out, driving particles to the wall, most of the heat and the particles are transported in the parallel direction. Then the targets receive most of the heat and particle exhaust in a really narrow region around the strike point. These conditions are challenging for the divertor, because the power density which hits the surface of it can exceed a technological limit of the material ($\sim 10\frac{MW}{m^2}$). This constraint is more restrictive for future machines, where the heat flux hitting the divertor is expected to overcome this value. This implies that this component needs a material which can resist to very high temperature, typically tungsten, and the plasma must be in a regime in which the heat flux is reduced (e.g. detachment), in order not to be damaged.
To create the plasma an electric field is generated toroidally by a temporal variation of the current in the central solenoid of the tokamak. When a threshold in such parameter is exceeded, the plasma is generated. Such condition is known as breakdown. A useful parameter called toroidal loop voltage is defined as $V_{loop} = E_\phi 2\pi R$, where E_ϕ is the toroidal electric field, and R is the major radius of the tokamak. Generally, after the breakdown, the plasma current is increased by changing V_{loop} up to a certain value. This phase is called ramp-up. In this phase, in order to increase the density of the plasma, neutral gas is puffed inside the confined region (i.e. gas puff, or GP), while to sustain the temperature auxiliary power can be injected from the outside using additional systems. These are the Neutral Beam Injection (NBI), Electron Cyclotron Resonance Heating (ECRH) and Ion Cyclotron Resonance Heating (ICRH). The first consists of high energy neutral beams which are collimated into the plasma. The neutrals react with the ions by charge exchange and collision, releasing energy to the plasma. This system represents also a source of energetic particles, which can interact in different ways with the background plasma. ECRH and ICRH heat respectively electrons or ions by resonance with the frequency of gyromotion of the particles around the magnetic field by Lorentz force. By using these heating systems the stored energy of the plasma is increased. After the ramp-up a phase with constant plasma current, called flattop, is initiated, during which the heating system is kept or increased and the fuel is pumped inside in order to obtain fusion reactions. Finally it follows a phase in which the plasma current is decreased, which is called ramp-down. The typical run of an experiment with the described phases is shown in figure 1.6. This is how is normally run an experiment, but sometimes phenomena which deviate the plasma by the desired evolution appear. The run of an experiment will be referred as discharge or pulse in the following.

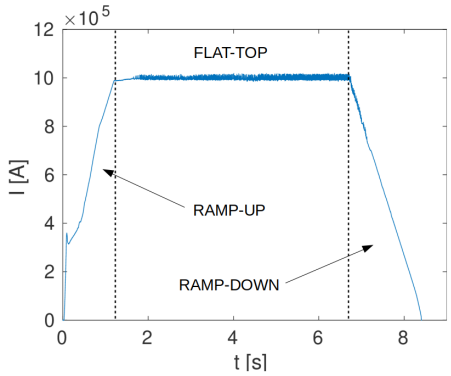

Figure 1.6: Typical evolution of a plasma discharge in a tokamak. The first phase with increasing plasma current is called ramp-up, then it follows the flat-top with constant plasma current, finally there is the ramp-down phase with decreasing plasma current.

1.3 Motivation

During the increase of the energy content of the plasma in a discharge several instabilities may develop, which could destabilize the plasma and can possibly cause a loss of confinement or disruption. This event is potentially catastrophical for future reactors and must be avoided, because the consequent release of energy on the PFCs could create severe damages, with following expensive reparations and long delays. In order to prevent disruptions of the plasma during a discharge it is necessary to correctly predict its behaviour in advance. Moreover, the capability to predict the evolution of a new plasma discharge can allow to improve the efficiency of the pulse. Several ways to perform these predictions already exist and they differ in level of detail and time expense. The easiest formulae available are the scaling laws [5], [6]. These calculate the confinement time taking into account physical and engineering parameters. They have been obtained by fitting experimental results. They have led to a development of a confinement trend, but they are 0-dimensional and miss a physics based nature, so their applicability and trustability is reduced. Moreover, they miss the profiles effects, which can be very important in several situations. An example is the value of the current near the LCFS, which affects the shape of the plasma. The predictions need to be more accurate to take into account these and other local effects. To this purpose, a set of different suites or codes can guarantee the most advanced physical description available. In fact, the complex models employed in gyrokinetic or fluid codes simulate the physics at a fundamental level, but they are time-consuming, thus they can not be run between discharges. This represents a limit, considering that during experimental campaigns "last-minute" changes in the planned evolution of the discharge could be applied due to technical reasons just before running it. This heavy time consumption can be overcome by making use of models based on a Neural Network (NN) framework [7]. NNs use nonlinear algorithms which take as input a big number of parameters and fit a wide experimental database employing different relations. The disadvantage associated with these models is that they need a wide database, against which they have to be

trained, and this is not always possible. Moreover, they provide good predictions when the parameters lay inside the range of variation of the database, but this is not always the case when a new discharge is executed. Finally they do not offer physics insights, because the algorithms work as a black box, and the interplays between different dependencies are not transparent to the user.
It is therefore necessary an approach based on a compromise between low time-consumption and reliable predictive power. This can be obtained by fast simulations based on first principles. A predictive tool which meets these prerogatives is the tokamak flight simulator Fenix [8, 9]. This is a numerical tool which predicts the plasma behavior using the discharge program as input. The discharge program is a set of planned time traces of parameters, which are supposed to be followed during the run of a specific pulse. The flight simulator verifies if the actuators or plasma parameters trajectories respect the earlier planned evolution. This allows the experimental leader to satisfy the experimental goals, avoid the exceeding of the operational limits and reduce the probability of plasma disruptions. The flight simulator is based on the interaction between the control system, that is the group of diagnostics and actuators which manipulate the plasma, the equilibrium and the transport, which are the main ingredients necessary to describe a tokamak. The plasma equilibrium can already be described analytically, through the implementation of a Grad-Shafranov solver. The Plasma Control System Simulation Platform (PCSSP) [10], which is an architecture developed for ITER, has been adapted in Fenix, together with a model of the Discharge Control System (DCS) [11], in order to simulate the control system of AUG. A fully integrated analytical transport model is instead still missing. Such transport model has to be physics based to be realistic, but also fast enough to be used as an inter-discharge prediction tool. This compromise can be reached by employing analytical models which are derived from first principles. An important task in the development of these models is to include as few experimental input as possible to strengthen the prediction capability, so that a new discharge without previous experimental bias or expectations can be designed. The work performed during this thesis has led to a new set of physics-based transport models, which were particularly adapt to be used in the context of the flight simulator. These models must not be thought as potential substitute of the models listed previously (e.g. gyrokinetic codes or NNs), but as alternative solutions to be used with different purposes. In fact the long-term planning of an experimental campaign should be still driven by integrated modeling with high-fidelity codes, which justify more the choice of a specific strategy with respect to another. Moreover the first-principle-based nature of the models developed in this thesis wants to offer a different approach to the user, in which the transparency of the physics is prioritized, so that an alternative solution to NNs can be offered. In addiction, the physics-based origin of these models should be valid regardless the size of the machine, therefore such models could in principle be extrapolated to future devices. The structure of the integrated model developed here is the following: two models are applied in the confined region of the tokamak, depending on the regime of the plasma, while another one acts in the SOL. These models give boundary conditions to each other through the parameters at the LCFS, which is the position where they are linked. In particular the model developed for the SOL gives boundary conditions for the confined region, taking as

input engineering parameters, which can be scheduled during the discharge's plan, reducing thus the amount of experimental input needed for the simulation to zero. The models are all based on analytical coefficients derived with different approaches: in the core a fitting of the transport coefficients obtained by simulating different flattop phases of a wide database of discharges with an existing validated transport code has been used; the edge has been modeled with a heuristic formula to take into account the main instability which affects this region when a pedestal is formed; the SOL model adopts a particle balance to calculate the density boundary conditions at the separatrix.
In this thesis 6 discharges have been validated in the framework of Fenix by using the newly developed transport models. The further description of the models requires a more detailed introduction of the physics involved. To this purpose the background theory is described in detail in the next chapter.

Chapter 2

Theoretical background

2.1 Equilibrium

The tokamak is based on a toroidally symmetric configuration (a "donut"), the bulk of which is where the plasma is formed and its dynamics takes place. The high temperature which is necessary to sustain the thermonuclear reactions inside it requires to confine the plasma, avoiding contact with the wall. Since the plasma is ionized, the magnetic field constrains the particles to move around its lines, due to the magnetic part of the Lorentz force $F = q\boldsymbol{v} \times \boldsymbol{B}$, where q is the particle charge, $\boldsymbol{v}$ is its velocity and $\boldsymbol{B}$ is the magnetic field. This provides a first essential confinement of the particles. The toroidal shape of the tokamak provides a magnetic configuration with closed field lines which constrains the plasma particles to follow $\boldsymbol{B}$. At this stage it is necessary to define several geometrical quantities which will be largely used in this thesis:

- R and Z are the radial and vertical coordinates of the torus;
- R_0 is the reference major radius, which is defined as the distance between the toroidal centre of the tokamak and a reference point
- a is the minor radius, which is defined as $a = \frac{R_{max} - R_{min}}{2}$, where R_{max} and R_{min} are the outermost and innermost positions of the plasma;
- the outer midplane (OMP) is the position of the LCFS found horizontally with respect to the magnetic axis;
- the poloidal plane is the cross section parallel to the R, Z plane;
- θ is the poloidal angle with respect to the OMP;
- ϕ is the toroidal angle.

The geometrical variables are shown in figure 2.1. The resulting magnetic field winds along the toroidal direction with particles moving in spiral around it. As opposed to the

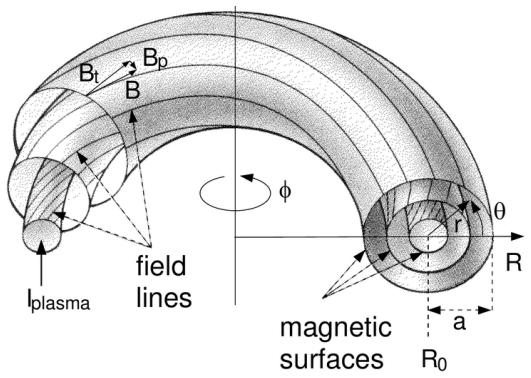

Figure 2.1: Geometry of the magnetic field lines in a tokamak and main geometrical parameters. B_t and B_p are the toroidal and poloidal magnetic fields. R_0 is the major radius, a is the minor radius, θ is the poloidal angle and ϕ is the toroidal angle.

stellarator the tokamak is toroidally symmetric, thus it is useful to refer to its poloidal cross section to describe the physics. This is shown in figure 2.2, for a typical shape of the plasma. In this picture the different red closed lines identify regions where the toroidal (or poloidal) magnetic flux is constant, as a consequence of the combination of the magnetic fields imposed by the coils and the plasma. These lines represent the toroidal (or poloidal) magnetic flux surfaces.

As already mentioned, a necessary condition for the plasma to be sustained in a tokamak is the equilibrium, which assures that the forces perpendicular to the magnetic flux surfaces are overall null. The magnetostatic force balance is

$$\nabla p = \mathbf{j} \times \mathbf{B}, \tag{2.1}$$

where p is the pressure and $\mathbf{j}$ is the current density. From this equation one can see that the current and the pressure gradient are perpendicular. Considering that the electron dynamic parallel to the magnetic field is much faster than the perpendicular one, the parallel pressure gradient can be neglected. Therefore, taking the radial component of equation 2.1 and using Maxwell equations, one can derive the Grad-Shafranov equation [2], under the assumption of ideal magnetohydrodynamic (MHD) fluid in a toroidally symmetric system:

$$\Delta^{\star}\mathbf{\Psi} = -4\pi \left(\mu_0 r^2 \frac{\partial p}{\partial \mathbf{\Psi}} + I \frac{\partial I}{\partial \mathbf{\Psi}} \right), \tag{2.2}$$

where $\Delta^{\star}\mathbf{\Psi} = R^2 \nabla \cdot (R^{-2} \nabla \mathbf{\Psi})$, $\mathbf{\Psi}$ is the poloidal magnetic flux, μ_0 is the vacuum magnetic permeability, I is the toroidal current and r is the radial coordinate as in figure 2.1. This equation determines the equilibrium of the plasma.

The assumption of $v_{e,\parallel} >> v_{e,radial}$, where $v_{e,\parallel}$ and $v_{e,radial}$ are respectively the electron velocity parallel to the magnetic field and the radial velocity, implies that ∇p is radial and $\mathbf{j}$ is parallel to the magnetic surfaces. Under these conditions the magnetic field lines are embedded into concentric magnetic surfaces, each with constant pressure. A picture of

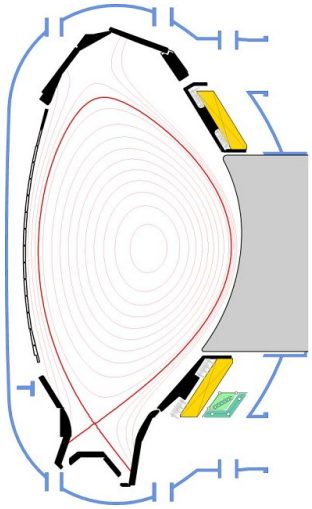

Figure 2.2: Poloidal cross section of a tokamak. The thicker red line identifies the magnetic surface of the LCFS. Within the LCFS, there are the closed magnetic field lines, which describe surfaces at constant magnetic flux. Outside the LCFS the lines are open and the particles are not confined.

the nested flux surfaces is shown in figure 2.1, while its poloidal projection can be seen in figure 2.2.
Together with the pressure, also the density and temperature can be assumed constant on the magnetic flux surfaces. Therefore these parameters are often described with 1D radial profiles, labeled with flux coordinates like

$$\rho_p = \sqrt{\frac{\Psi - \Psi_{axis}}{\Psi_{LCFS} - \Psi_{axis}}}, \tag{2.3}$$

$$\rho_t = \sqrt{\frac{\Phi - \Phi_{axis}}{\Phi_{LCFS} - \Phi_{axis}}}, \tag{2.4}$$

where Φ is the toroidal magnetic flux. These coordinates are defined so that they are null at the magnetic axis and equal to 1 at the LCFS.
An important parameter which is often used in plasma physics is the ratio between kinetic and magnetic pressure, namely

$$\beta = \frac{2\mu_0 p}{B^2}. \tag{2.5}$$

β is a key parameter for the stability and the performance of the plasma.
Another crucial parameter that affects the stability of the plasma is the safety factor q. This is defined as the ratio between the toroidal and the poloidal angle traveled by a magnetic field line during one turn in the toroidal direction. In a tokamak with a simple circular poloidal cross section, under the approximation of large aspect ratio, it can be calculated as

$$q = \frac{rB_t}{RB_p}, \tag{2.6}$$

where r is the minor radius. This quantity is important for the stability, because depending on its value different MHD instabilities can develop, like sawteeth or kink modes. A q-derived parameter called q_{95} is used. It consists of the value of q at 95% of the magnetic flux. This parameter is used because the value of q at the separatrix diverges. A plasma is usually unstable for $q_{95} < 2$ or $q < 1$. In fact, even when the equilibrium is reached, other dynamic can drive loss of energy and particles. This dynamic can be roughly splitted in MHD instabilities, which can set soft or hard limits to the operation of the machine, and transport. The former can be extremely abrupt, especially in case of hard limits, therefore it is better to try to avoid it. The latter is instead always present and it represents a constant output of energy from the plasma, but usually does not imply potential damages of the experiment, thus the correct approach is to try to mitigate it. Both the dynamics are explained in the next sections.

2.2 Transport

Transport physics describes the evolution of a system at the macroscopic (i.e. thermodynamical) level. The theory of transport can be used to simulate the kinetic profiles by including sources and sinks. In order to do this one has to correctly predict how particles, energy and momentum are retained or expelled in the plasma. In the past it has been conjectured that the radial transport was mainly dominated by the collisions which are produced by Coulomb scattering between charged particles. This source of transport is addressed as *collisional* or *classical* (neoclassical, in the case of a tokamak) [12]. However the transport measured experimentally was found substantially higher than the one formally referred to the collisions, up to 2 order of magnitudes. The residual transport was then addressed as *anomalous*. This remaining piece of transport has been found to be caused by micro-turbulence, which derives from the fluctuations of the particle distribution function in the plasma. In fluid theory these fluctuations generate perturbations of an interface between 2 regions of the plasma which have different conditions (e.g. different density or temperature). For example in a tokamak plasma these perturbations, triggered by the particle drifts, can be affected by the kinetic profile gradients [13]. Under specific conditions these perturbations are amplified and that is what causes most of the radial cross-field transport. The description of turbulent transport is non-trivial due to the nonlinear dependence of the amplitude of the radial diffusion on the plasma equilibrium quantities and the magnetic geometry. Moreover, the properties of turbulent transport can change significantly from the core to the edge of the plasma, depending on the different regimes of the plasma, due to strong changes in the plasma parameters. While the core turbulent transport is well understood, the turbulent transport in the edge of the plasma depends on the different confinement regimes (L-mode, ELM-free regimes, and H-mode), and thus the correct modeling of it still represents a challenge.

2.2.1 Collisional transport

As already mentioned the collisional transport arises from collisions which affect the charged particles gyromotion around the field lines. This is also called classical transport. For this process the characteristic radial step length is the Larmor radius, which is the radius of the trajectory traveled by a particle around a magnetic field line, $r_{L,s} = \frac{m_s v_{\perp,s}}{qB}$, where the subscript s indicates a specific species, m_s is the species mass and $v_{\perp,s}$ is the velocity perpendicular to the magnetic field lines, and the frequency is given by the collision frequency ν. Employing random motion arguments, one can define a diffusion coefficient for species s as

$$D_{cl,s} = r_{L,s}^2 \nu. \tag{2.7}$$

This formula can be used for both particle and heat diffusivity. The latter will be referred in the following as χ. Because the perpendicular velocity is proportional to $\sqrt{\frac{T_s}{m_s}}$, it follows that $r_{L,s}^2 \propto m_s$. The collision frequency between species a and b is proportional to $\nu_{ab} = \frac{\sqrt{m_{ab}}}{m_a} Z_a^2 Z_b^2$ where Z is the charge of the different species, and m_{ab} is the reduced mass, which is defined as $m_{ab} = \frac{m_a m_b}{m_a + m_b}$, and is approximately m_e for electron-ion collisions and $m_{ii} = \frac{m_i}{2}$ for ion-ion collisions. Thus, $\nu_{ii} \propto \frac{1}{\sqrt{m_i}}$ and $\nu_{ei} \propto \frac{1}{\sqrt{m_e}}$. The classical heat conductivity is therefore much higher for ion-ion collisions due to their much higher mass:

$$\chi_{ii} = \frac{\sqrt{m_i}}{\sqrt{m_e}} \chi_{ei}. \tag{2.8}$$

It is worth to notice that the higher is the charge of the ion species the stronger is its associated classical transport, which makes it particularly important for heavy impurities. In terms of particle transport instead the ambipolarity must be fulfilled, that means that in absence of impurities the ion particle diffusivity must equal the electron one.
Within a tokamak the situation is more complicated, because its geometry implies modifications of the particles dynamic. Then the classical transport in the tokamak is called *neoclassical transport*. In a tokamak the toroidal magnetic field varies radially, according to Ampère's circuital law

$$B_T = \frac{\mu I}{2\pi R}, \tag{2.9}$$

where R is the major radius and I is the poloidal current, which in the vacuum is approximately equal to the current of the toroidal coils. This implies a gradient of the toroidal magnetic field along the field lines, which generates a magnetic mirror. This mirror inverts the trajectory of some particles generating the banana orbits, which can be seen in figure 2.3. Such particles are called trapped particles and they represent the main novelty of the neoclassical transport. Also for this transport one can find a characteristic scale-length, which comes from the combination of the passing and trapped particles. The former is still the Larmor radius, while the second is the banana width, which can be expressed as

$$w_b = \frac{r_L q}{\sqrt{\epsilon}}, \tag{2.10}$$

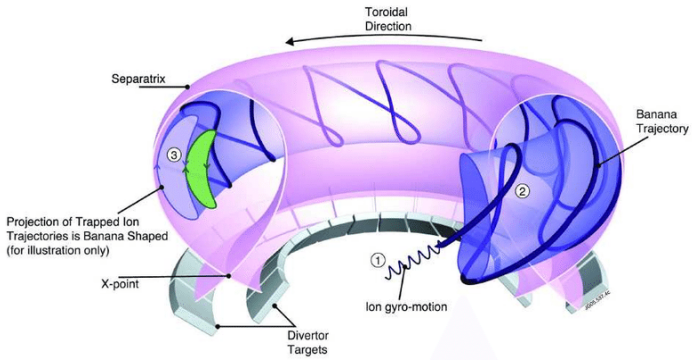

Figure 2.3: Trajectory of particles around the field lines (gyromotion) and geometrical representation of the banana orbits. The banana orbits (in green) experience a slow toroidal precession, due to the differential $\nabla B \times B$ drift along the radius.

where $\epsilon = \frac{r}{R}$ is the inverse of aspect ratio. Considering that the banana width is much bigger then the Larmor radius, it can be used as characteristic scale-length to quantify a diffusion coefficient, as made earlier. To this purpose also another collision frequency for the trapped particles must be derived. One can prove that for banana orbits this is $\nu_{nc} = \frac{\nu_{cl}}{2\epsilon}$. In a similar way to what has been done for classical transport, the neoclassical diffusivity from trapped particles can then be expressed as

$$D_{nc} = w_b^2 \nu_{nc} = \frac{q^2}{\epsilon^{1.5}} D_{cl}. \tag{2.11}$$

The neoclassical particle flux associated with this diffusivity is proportional to $f_t = \frac{n_t}{n}$, that is the fraction of trapped particles on the entire species population, which are the one driving the transport in the banana orbits, and can be expressed through a geometrical factor as $\sqrt{2\epsilon}$. D_{nc} is usually found around 1-2 order of magnitudes bigger than D_{cl}.
The neoclassical transport can be split in 3 different regimes depending on the value of a normalized collisionality, defined as

$$\nu_\star = \frac{\nu_{nc}}{\omega_b} = \frac{\nu q R}{2\epsilon^{1.5} v_{th}}, \tag{2.12}$$

where ω_b is the bounce frequency of the banana orbits. The dependence of the neoclassical transport on the collisionality is related to the contribution from trapped particles, which is lower for high collisionality regime, due its associated detrapping collisions. Three different regimes can be identified: the banana regime for $\nu_\star < 1$, the plateau regime for $1 < \nu_\star < \epsilon^{-1.5}$ and the Pfirsch-Schlüter regime for $\nu > \epsilon^{-1.5}$. Depending on the different regime of the neoclassical transport one can find different dependencies of the transport coefficients on collisionality. In the banana regime, where the collisionality is too low to determine a considerable detrapping, the transport increases with collisionality, following the general trend of classical theory (i.e. by collisions of free particles). In the plateau regime the dependence on $\nu_\star$ is weak, because this is a transition region where the transport

contribution due to the trapped particles is reduced, due to the detrapping collisions, while the contribution from free particles is increased, according to the classical transport. This is why this regime is called *plateau*. Finally in the Pfirsch-Schlüter regime the transport increases again with collisionality, because the effect of increased free particles associated transport is bigger than the reduction of trapped particle contribution. However, the increase rate is smaller with respect to the banana regime, where the contribution due to the detrapping particles is smaller.
Neoclassical transport is in general found to be lower than turbulent transport in the direction perpendicolar to the magnetic field lines. However, there are configurations of the plasma (e.g. the edge transport barrier in H-mode, ETB, or the internal transport barriers, ITB [14]) where the radial turbulent transport is suppressed or reduced. There, the neoclassical transport is dominant. As the classical transport, the neoclassical one is always much stronger for the ions with respect to the electrons. Moreover, since the collision frequency has a dependence on Z^2 the neoclassical transport is often dominant for heavy impurities. Several codes have been developed during the years to compute the neoclassical transport coefficients, like NCLASS [15] or NEO [16]. In [17] simplified formulae for the neoclassical ion heat diffusivity have been derived for the banana regime, fitting the results of CQL3D [18] simulations, and through a generalization they have been extended to the other neoclassical regimes. Coefficients for the neoclassical transport of impurities have been obtained in [19].
While the neoclassical transport is two order of magnitude bigger than the classical one, it is still often found lower than the total transport. As already said the missing part is provided by turbulence-driven *transport*, which is described in detail in the next section.

2.2.2 Turbulent transport

Turbulent transport is in general the dominant transport mechanism in the tokamak plasma core, especially for low levels of collisionality. It is driven by linearly unstable modes on small scales which grow and saturate, by nonlinear interactions with other modes. The first step to describe the turbulent transport is to identify its origin. The fundamental origin of such transport in the core is the fluctuation of the kinetic profiles in the tokamak. In fact, the particles normally move around the magnetic field lines, but due to the curvature and the gradient of the magnetic field the particles experience drifts, which amplify the fluctuations, leading to regions of the tokamak where the concentration of a specific species is increased. If there is a background temperature or density gradient in presence of these drifts, under specific conditions a big amount of heat and particle transport can be driven radially outwards. These mechanisms are known as micro-instabilities (in particular interchange instabilities). They are similar to the Raylegh-Taylor instability. One example is the ion temperature gradient (ITG) mode, which is sketched in figure 2.4. A local ion temperature fluctuation on a flux surface, related to the curvature and ∇B drifts, leads to an opposed local ion density fluctuation, if the pressure does not change. This inhomogeneous density distribution causes a poloidal electric field. In a pure plasma, the fluctuation of the ion density is followed by a fluctuation of the electron density, to conserve

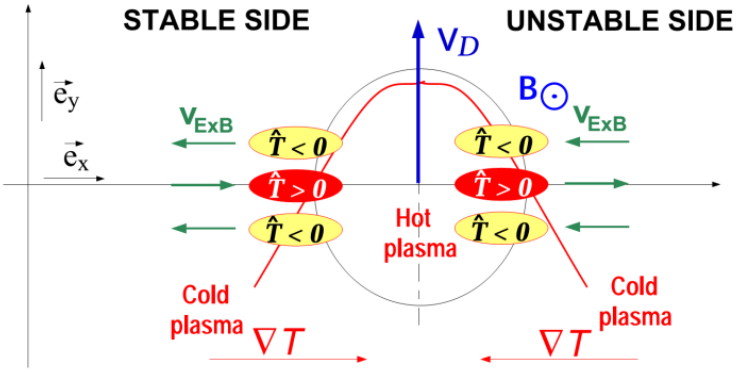

Figure 2.4: Mechanism which leads to the ITG mode in the poloidal cross section of a plasma. A temperature perturbation causes different radial drift velocities of the local ions, which leads to the creation of an electric field that results in an E×B flow that amplifies the original perturbation. Figure from C. Angioni, *Advanced Courses on Fusion Plasma Physics* (2018), Max-Planck-Institut für Plasma Physik, Garching bei Muïchen.

the quasi-neutrality

$$Z_i \tilde{n}_i \approx \tilde{n}_e. \tag{2.13}$$

The difference between $Z_i\tilde{n}_i$ and $\tilde{n}_e$ is due to the polarization charge. Supposing that the electrons are adiabatic (i.e. the electron response to the ion density fluctuation is immediate), one has a parallel unbalance of the electron density. The parallel force balance implies an electric field parallel to the magnetic field lines to counteract the pressure gradient

$$\nabla_\parallel p_e = n \nabla_\parallel \phi. \tag{2.14}$$

The resulting electric field E, coupled with the magnetic field leads to an $E \times B$ drift which can either increase or reduce the initial perturbation by driving the hot ions outwards or inwards and the cold ions inwards or outwards. The conditions for which the instability is destabilized or stabilized depend on several parameters, but a threshold nature on the temperature gradient has been derived theoretically and then observed experimentally. If the instability is destabilized, then the background ion temperature gradient is reduced and an amount of energy is lost. This can only happen in the low field side (LFS) of the tokamak, where ∇B and ∇T have the same direction, while in the high field side (HFS) the different direction of the gradients does not allow the instability to grow. However, the total radial transport comes from an average between the contributions at different poloidal localizations. This instability, which is called ITG, takes his name from the fact that it is triggered by the ion temperature gradient. As already mentioned, its associated transport shows a threshold nature, that means that below a critical value of the normalized gradient $-R\frac{\nabla_r T_i}{T_i}$ the mode is stable (i.e. negative growth rate), while above this threshold the instability is destabilized. The value of the threshold depends on several parameters and its determination is non-trivial. The transport coefficient increases with a power law

of the difference between the normalized gradient and its threshold value, according to

$$\chi_i = H_{\nabla_r T_i} \cdot \left[-R\frac{\nabla_r T_i}{T_i} - R\left(\frac{\nabla_r T_i}{T_i}\right)_{crit} \right]^{\epsilon}, \tag{2.15}$$

where $H_{\nabla_r T_i}$ is

$$H_{\nabla_r T_i} = H\left[-R\frac{\nabla_r T_i}{T_i} - R\left(\frac{\nabla_r T_i}{T_i}\right)_{crit} \right], \tag{2.16}$$

H is the heaviside function, whose argument is shown between brackets in equation 2.16. H shows the threshold nature, $R\left(\frac{\nabla_r T_i}{T_i}\right)_{crit}$ is the threshold value of the normalized temperature gradient, and ϵ is typically not null. The proportionality between the heat diffusivity and the power law shown in equation 2.15 is known as *stiffness* [21], and is the reason why the temperature profiles can not increase to an arbitrary level, regardless the input power inserted in the tokamak. Its effect is more pronounced in the inner confined region (i.e. core), while in its external part (i.e. edge) the physical picture is more complicated and a transport model based on the stiffness is not exhaustive. This implies that the maximum achievable temperature at the center of the plasma can strongly depend on the edge value. In particular, if one could in principle enhance the temperature in the edge, that could lead to lower local temperature normalized gradient in the core. In other words most of the energy contained in the plasma would be sustained by the edge. This is what happens in the high-confinement mode (H-mode), where a pedestal arises in the edge. In this condition the energy contained in the core would strongly depend on the edge performance.
A similar treatment can be done for the trapped electron mode (TEM) and the electron temperature gradient (ETG) mode. The former is driven by the electron temperature and density gradient, while the latter only by the electron temperature gradient.
The turbulent transport driven by plasma micro-turbulence can be calculated through the usage of different codes, which need different computational costs and contain different amounts of physics ingredients. Before introducing them, it is important to discuss about the timescales and the lengthscales of the turbulence. The typical timescale of the microinstabilities previously discussed is of the order of the ion sound transit time ($\sim \frac{R}{v_{th,i}}$), which is smaller than the energy confinement time τ_E, meaning that the turbulence is an important and non-negligible phenomenon for the confinement of the plasma. Moreover, the smaller time scale allows to calculate the turbulence assuming stationary macroscopic conditions, because the background quantities of the plasma vary slower than the turbulence itself. The lengthscale of the turbulence is the ion gyroradius, which is normally much shorter than the characteristic length of the tokamak (e.g. local gradient scale length). The turbulence frequency is generally much smaller than the cyclotron one (i.e. the time needed to perform one revolution around a magnetic field line). This allows us to take an average of the position of the electron in the gyromotion trajectory and treat it as a "charged ring", known as gyrocentre. In other words this means that the dynamic of a single particle, which was initially developed in 6 dimensions (3 in velocity and 3 in space) can be reduced to 5 (2 in velocity and 3 in space), because the Larmor gyration time-scale

is much shorter than the turbulence one. This is the simplification introduced by the gyrokinetic codes with respect to the kinetic codes (which are 6D). In fact, the gyrokinetic codes solve the kinetic equation in a specific form, which is derived with the assumption of the gyrocentre, coupled with the Maxwell equations. The simulations performed with these codes can be distinguished mainly in linear and nonlinear. While the first allows only to find which modes are unstable (i.e. what are the growth rates of the instabilities and for which length-scales), the second can also describe the evolution of these modes, based on the interaction with other modes and other physical features like zonal flows and MHD waves. This interplay leads in general to a level of saturation of the instability and consequentially of the associated transport. The nonlinear gyrokinetic simulations have the highest content of physics but they are the most expensive in terms of computational time (up to months). The computational time of the gyrokinetic simulations is increased also when they are global, which means that they take into account finite Larmor radius (FLR) effects. This in turn means that the gyroradius is non-negligible respect to the normalized gradient length-scale (i.e. $\rho_L \approx L_T$). This treatment is necessary in specific configurations in which the gradients are really steep (like in the pedestal region of a H-mode), leading to small length-scales.
Starting from the gyrokinetic equation, one can also develop an alternative description, trying to represent the plasma as a fluid. This is done in the gyrofluid codes, where a set of moments of the gyrokinetic equation is taken. One should in principle take infinite moments of the kinetic equation to reach the same level of detailed physical description. However, this is obviously not feasible, so the set of moments is truncated at a low number (usually 4-12) and a closure of the equations must be introduced. The formulation of this closure is the biggest and often most delicate assumption made in a gyrofluid code. The CPU time consumption is usually smaller than a gyrokinetic nonlinear simulation, but there are less physics insights, due to the reduction or lack of kinetic effects and description of nonlinear evolution of the modes. Gyrokinetic and fluid codes can calculate the turbulence spectra (e.g. length-scale vs frequency or length-scale vs growth rate), and then derive consistently the associated level of transport. Considering that the gyrokinetic nonlinear simulations have a strong CPU time consumption, reduced gyrofluid models can be used as alternative. For example the quasilinear transport models are adapt to mimic nonlinear corrections to linear gyrofluid codes. These models solve moments of the linearized kinetic equations with a fluid closure to find the growth rate and characteristic scalelength of the unstable modes, and they use a saturation rule to represent the saturation of the turbulence. This means that the electric potential which initially drives the instability is assumed proportional to $\frac{\gamma}{k_y^2}$, where γ is the growth rate and k_y is the characteristic scalelength perpendicular to the magnetic field lines. From a fluctuating potential $\tilde{\phi}_k$ arises an $\mathbf{E} \times \mathbf{B}$ perpendicular drift which can drive particle and heat fluxes through the following

relations

$$\boldsymbol{\Gamma} = \left\langle \int \tilde{f} \frac{\boldsymbol{B} \times \nabla \tilde{\phi}}{B^2} \cdot \boldsymbol{e_r} d^3 v \right\rangle, \tag{2.17}$$

$$\boldsymbol{Q} = \left\langle \int E \tilde{f} \frac{\boldsymbol{B} \times \nabla \tilde{\phi}}{B^2} \cdot \boldsymbol{e_r} d^3 v \right\rangle, \tag{2.18}$$

where $\mathbf{e_r}$ is the radial versor and $\tilde{f}$ is the perturbed distribution function. Averaging over time and spatial scales the fluxes can be expressed in Fourier space as

$$\Gamma = \left\langle \sum_{k\omega} Re \left[\frac{i k_y \tilde{n}_{k\omega} \tilde{\phi}^{\star}_{k\omega}}{B \left| \tilde{\phi}_{k\omega} \right|^2} \right] \left| \tilde{\phi}_{k\omega} \right|^2 \right\rangle, \tag{2.19}$$

$$Q = \left\langle \sum_{k\omega} Re \left[\frac{3}{2} \frac{i k_y \tilde{p}_{k\omega} \tilde{\phi}^{\star}_{k\omega}}{B \left| \tilde{\phi}_{k\omega} \right|^2} \right] \left| \tilde{\phi}_{k\omega} \right|^2 \right\rangle, \tag{2.20}$$

where ω is the frequency and k the radial scale of the mode. The terms in the square brackets are the quasilinear weights, which are the proportionality coefficients between the fluxes and the potential fluctuations. The expression of the potential $\tilde{\phi}$, which sets the different contributions from different scales, is described by the saturation rule, which is obtained by fitting a wide database of nonlinear gyrokinetic simulations.
An example of quasilinear gyrofluid code is TGLF [22], [23]. The acronym stands for trapped-gyro-Landau-fluid. In fact, in this code the Landau damping is used to close the fluid equations, considering resonances with the passing electrons, and the trapped particle treatment is included (trapped particle fraction is estimated via a geometrical factor). TGLF solves a set of eigenvalue equations composed by 12 moments for the passing particles and 3 moments for the trapped particles for each species. This is done by decomposing the fields in Hermit polynomials, to take into account poloidal variations. TGLF includes also the modeling of other additional physics (e.g. $E \times B$ shear, zonal flows, electromagnetic effects) and its interaction with the turbulence. This code has been used in this work to create a database which has been used in the transport model for the core. To summarize, TGLF can calculate the turbulent fluxes taking as input different parameters (e.g. the kinetic gradients, the collisionality, the equilibrium of the plasma). TGLF gives a spectrum of modes with specific ω and k values, which can identify different micro-instabilities. The separation between different modes is based on different ranges of frequency and lengthscale and different drives. In fact, the microinstabilities affecting the core transport can be driven from different parameters. While ITG, ETG, and TEM are usually driven by gradients of the temperature (and density in the case of TEM), other electromagnetic instabilities exist for high pressure, which are the micro tearing mode (MTM) and the kinetic ballooning mode (KBM), which are driven by terms proportional

to β or β'. Regarding the ranges of spatial scales in which the instabilities exist, one rough distinction can be done to approximately split them: most of the ITGs, TEMs, MTMs and KBMs appear for $k_y\rho < 1$, while ETGs exist for $k_y\rho > 1$. The first range is representative of the ion scales, while the second range belongs to the mixed or electron scales. Different micro-instabilities have also different stabilizing parameters. In particular ETG is stabilized by the density gradient and $\frac{T_e}{T_i}$, ITG by the density gradient and $\frac{T_i}{T_e}$ and TEM by the collisions and $\frac{T_i}{T_e}$.

2.2.3 Edge Transport

As already said the micro-instabilities which mainly affect the core are ITG, TEM and ETG. Which instability is dominant depends on the combination of driving mechanisms and stabilizing effects, while from an engineering perspective, the specific heating system used, injection of pellets and fuel from outside, etc, will determine the self-consistent state of the plasma and the characteristics of the underlying turbulence. Regarding the edge the situation can be completely different, depending on the specific configuration of the plasma. For example in the H-mode the $E \times B$ shear reduces strongly the turbulence [24], especially for the ion scale instabilities (ITG). This phenomenon is a possible origin of the pedestal formation in the edge of a H-mode. In fact, in this region the profile of E_r shows a strong gradient, as can be seen in figure 2.5. This translates in a strong $E \times B$ gradient, which

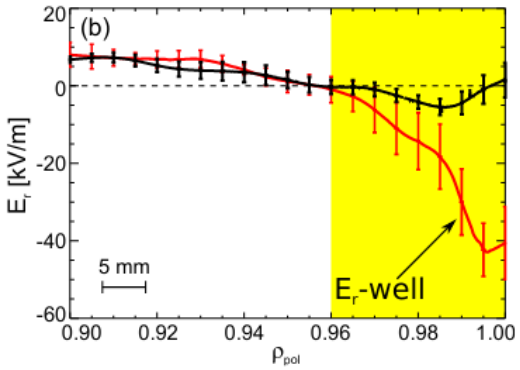

Figure 2.5: Radial profile of E_r for an L-mode (black) and H-mode (red). Figure from "U. Plank, *The effect of the radial electric field around the separatrix on the access to the high confinement mode at ASDEX upgrade*, PhD thesis (2022)".

drives the particles in a direction perpendicular to the magnetic field lines, with an intensity that varies radially. Such differential movement of the particles stretches the turbulent structures, decorrelating and tearing apart the eddies. This in turn reduces the radial scale of the turbulence, enhancing then the pressure gradient. The suppression of turbulence by the shear flows is shown in figure 2.6. However, a minimum amount of turbulent transport via ETG, MTM, KBM and/or TEM persists, due to the smaller effectiveness of sheared flows in the reduction of turbulence for the electronic scales. TGLF does not contain enough

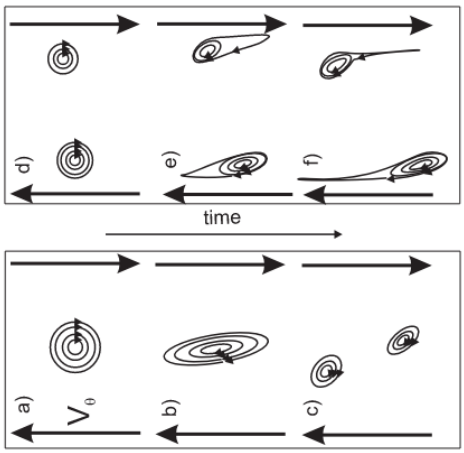

Figure 2.6: Decorrelation and tearing apart of the turbulence eddies due to the shear flows. A difference in the shear flows generate a stretching of the eddies, decorrelating them and reducing the radial space scale of associated transport. Figure from "P. Manz et al., *Phys. Rev. Lett. 103*, 165004 (2009)"

physical ingredients to describe this specific region of the plasma under these conditions (multiple instabilities, with electromagnetic nature and complicated nonlinear interaction leading to non-trivial saturation). To this purpose nonlinear gyrokinetic codes are more adapt, but considering the configuration of the field lines and the steep gradients in the pedestal of a H-mode a fit dense grid must be used in global simulations, which is strongly time consuming. The interaction between a wide group of instabilities sometimes imposes also multiscale simulations to correctly predict the plasma behaviour, which also increases the computational time. In the edge experimental measurements have shown consistence with MTM [25], [26], [27], KBM [25], [27], [28], [29] and TEM [25]. Linear gyrokinetic simulations have identified MTM [30], [31], [32], [33], [34], TEM [34], [35], ETG [33], [34], [36], [37], and KBM [29], [30], [32], [33], [34], [38]. Other nonlinear gyrokinetic simulations show that MTM is the main instability which can quantitatively justify the experimental transport in the pedestal of JET discharges [39], [40].
The structure and the physics of the pedestal is related to the combination of turbulence and MHD stability, which is described in the next section.

2.3 MHD stability

MHD in tokamak represents an extremely important dynamic, because it limits several global parameters of the plasma (e.g. average density, β), which should not be exceeded, because they can affect the plasma performance. Such limits are known as soft and hard limits. While the former can in principle be tolerated and do not imply major damages, the latter must absolutely be avoided, because they can cause a disruption and terminate the plasma in such a way that could severely damage the device. An example is the

Greenwald density limit [41], which has been found experimentally and is suspected to be due to a complicated interplay between radiative instabilities and MHD modes. A correct prediction of MHD stability is then necessary to take into account these important effects. MHD theory describes the equilibrium of the plasma through macroscopic quantities like mass density ρ, fluid velocity $\boldsymbol{v}$ and current density $\boldsymbol{j}$. As opposed to micro-instabilities MHD is developed to treat instabilities with long wavelength and high frequency. An additional typical assumption is to combine all species in a single fluid. MHD theory can be developed starting from the hydrodynamic equations (where the force balance includes electromagnetic forces) and Maxwell's equations. These are listed here:

$$\frac{\partial \rho}{\partial t} + \nabla \cdot (\rho \boldsymbol{v}) = 0, \qquad \rho \frac{d\boldsymbol{v}}{dt} = \boldsymbol{j} \times \boldsymbol{B} - \nabla p, \qquad \frac{d}{dt}\left(\frac{p}{\rho^{\gamma}}\right) = 0, \tag{2.21}$$

$$\nabla \times \boldsymbol{E} = -\frac{\partial \boldsymbol{B}}{\partial t}, \qquad \nabla \times \boldsymbol{B} = \mu_0 \boldsymbol{j}, \qquad \nabla \cdot \boldsymbol{B} = 0, \qquad \boldsymbol{E} + \boldsymbol{v} \times \boldsymbol{B} = \eta \boldsymbol{j}, \tag{2.22}$$

where η is the plasma resistivity. Based on the assumptions made on η one can derive ideal or resistive MHD. In fact when η is non-negligible it means that the magnetic flux is not conserved. This condition leads to magnetic reconnection processes which can generate magnetic islands and drive several instabilities. For example sawteeth can strongly affect the confinement when a high current discharge is run and the safety factor reaches local values below 1. When resistivity can be neglected, one can derive ideal MHD theory. By combining these equations one can derive the Grad-Shafranov equation [2], which calculates the equilibrium of the plasma with all the associated macroscopic parameters. In this condition there are no instabilities. If a linear perturbation takes place (generated by fluctuations of the macroscopic parameters or the magnetic field) the response of the plasma can decrease (stable equilibrium) or increase (unstable equilibrium) the initial perturbation. The latter represents the effect of MHD instabilities.

There are two main procedures to describe MHD instabilities. The first is similar to the one used in the fluid codes to calculate micro-instabilities and consists in calculating the eigenvalues derived from the solution of the perturbed part of the linearized MHD equations. Depending on the sign of the solutions one can have growing (unstable) and decaying (stable) instabilities of different time and length scales. As in the gyrokinetic codes, linear simulations allow to calculate only the trigger of instabilities, without any clue on their development, while to describe the evolution of the different modes and the associated transport nonlinear calculations are necessary. Such simulations are really expensive in terms of computational time and therefore are not always possible.

Another approach to characterize the linear stability of MHD modes is the variational energy principle. This is based on the definition of a displacement vector of the plasma $\boldsymbol{\xi}$. When this small displacement generates a reduction of the potential energy of the system the plasma is unstable. This theory is based on an analogy with gravitational potential energy, and it represents a simpler approach to linear stability than solving the linearized

eigenvalue equations. The equation which describes the change of the potential energy is

$$\begin{aligned}\delta W_F = \frac{1}{2}\int_F \Bigg[\left(\frac{|B_{1,\perp}|^2}{\mu_0} + \frac{B_0^2}{\mu_0}|\nabla\cdot\boldsymbol{\xi}_\perp + 2\boldsymbol{\xi}_\perp\cdot\boldsymbol{k}|^2\right) + \gamma p_0|\nabla\cdot\boldsymbol{\xi}|^2 \\ -2(\boldsymbol{\xi}_\perp\cdot\nabla p_0)(\boldsymbol{k}\cdot\xi_\perp^\star) - \frac{j_{0\parallel}}{B_0}(\boldsymbol{\xi}_\perp^\star\times\boldsymbol{B_0})\cdot\boldsymbol{B_1}\Bigg]\,dV,\end{aligned} \tag{2.23}$$

where 0 and 1 denote equilibrium and perturbed values, $\boldsymbol{k}$ is the curvature vector, $\perp$ indicates quantities perpendicular to the magnetic field lines and $\star$ indicates the complex conjugate. The index F refers to the plasma component of the energy change, because the vacuum part is usually stabilizing. The terms which make this integral negative are the destabilizing ones. The first two terms in the integral are related to the magnetic and fluid wave energy and are always positive, which means that they stabilize the plasma. They are Alfven and acoustic waves [42]. The last two terms can instead be negative and destabilize the system, depending on their sign:

- the term $-2(\boldsymbol{\xi}_\perp\cdot\nabla p_0)(\boldsymbol{k}\cdot\xi_\perp^\star)$ includes a pressure gradient, which is the driving force of the instability. In particular when the pressure gradient is parallel to the curvature vector then the term is negative and destabilizing. Therefore, like for the interchange instability, there is a good curvature region in the HFS, where the pressure gradient is stabilizing, and a bad curvature region in the LFS, where it is destabilizing. The instability which grows in the bad curvature region is known as ballooning instability, due to the shape that the magnetic surfaces in the LFS can show when a strong ∇p_0 destabilizes the plasma;

- the term $j_{0\parallel}B_0^{-1}(\boldsymbol{\xi}_\perp^\star\times\boldsymbol{B_0})\cdot\boldsymbol{B_1}$ is driven by the current density parallel to the magnetic field $j_{0\parallel}$. These instabilities are due to the kink of the magnetic surfaces and then are called kink instabilities. To visualize the evolution of the plasma affected by this instability one can imagine the kink of a towel when it is twisted. When they appear in the edge these modes are called peeling modes.

These instabilities are related to high values of pressure gradient and current density, which are conditions that are often found in different configurations of the plasma, like in the edge of a H-mode. In this regime the kinetic profiles at the edge increase, forming a pedestal. In these conditions there is a big bootstrap current, which is due to the collisions between passing and trapped particles. In particular, the strong pressure gradient implies a difference between the amount of particles traveling along two banana orbits in different radial positions. Such difference generates a net differential velocity along an orbit. This velocity interacts with the passing electrons by collisions and creates an additional current. A sketch of such phenomenon is shown in figure 2.7.

As already mentioned, in the edge of a H-mode strong pressure gradient and high parallel bootstrap current are present. Thus, a model called peeling-ballooning (PBM), which has to take into account both the related instabilities, has been derived. In particular for every geometry of the plasma a plot with the stable and unstable regions and the

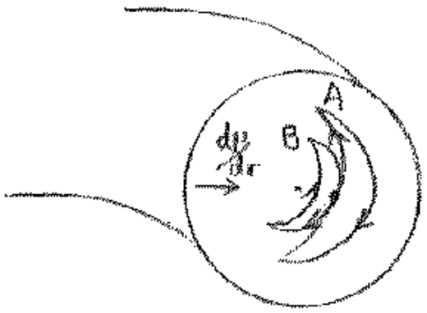

Figure 2.7: Picture of the bootstrap current generation. The particles A and B have different pressures. This means that B will pass more frequently than A in the point where their trajectories meet. This generates a net downwards current in that point. This current has a toroidal extension and can interact with the passing electrons by collisions generating an additional current called *bootstrap current*.

marginal stability can be drawn assuming different combination of ∇p_0 and $j_{0\|}$. This plot together with a schematic evolution of the pedestal in a H-mode is shown in figure 2.8, for a standard shape of the plasma. Depending on the shape of the plasma one can intervene

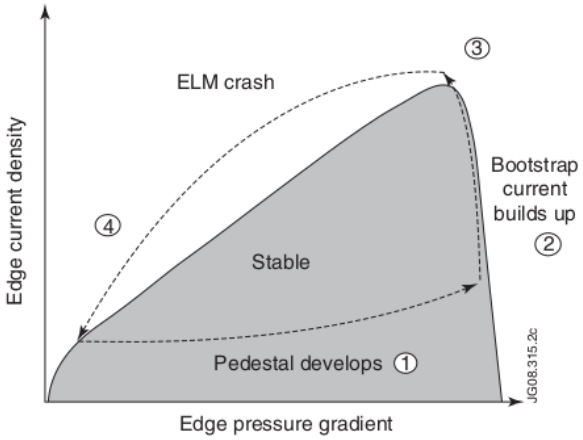

Figure 2.8: Peeling ballooning diagram for tokamak edge stability. The evolution of the pedestal follows 3 phases: in the first the pedestal develops, increasing the pressure gradient, this drives an increase of the bootstrap current in the second step; finally in the third step the marginal stability is reached, which is usually due to a combination of peeling and ballooning unstable plasma, and an ELM crash restores the initial conditions of the plasma. Figure from "Magnetohydrodynamic Stability of Tokamaks", by Hartmut Zohm (2014), in turns derived by a figure from J. W. Connor, Plasma Phys. Control. Fusion 40 531 (1998)

on the value of the first two terms of the δW_f integral and access also a secondary stability

region where the plasma is ballooning-stable [43]. The PBM sets a boundary of stability. When the plasma crosses this boundary passing from stable to unstable the edge localized modes (ELMs) arise, and a further transport of particle and energy is triggered, leading to a decrease of the plasma energy content. Even though this has also a beneficial effect (flushing out the impurities from the core and sometimes avoiding the plasma to reach hard limits), it is a major problem from the technological point of view. In fact, the strong release of energy carried by an ELM reaches the divertor, which is a protective material that collects the heat and particles which are expelled from the plasma, with an amount of heat that can irreversibly damage the component. To avoid this, there is a technological limit of the power density which can impact the PFCs, over which melting and erosion increase strongly. This limit is roughly $10\frac{MW}{m^2}$ and the ELMs, if not mitigated, are expected to strongly exceed it in future devices [44]. Several plasma configurations (called ELM-free scenarios) have been developed to try to avoid or mitigate the presence of the ELMs in H-mode. A correct modeling of the ELMs is necessary to perform any theoretical study. To this purpose there are linear codes which solve the linearized MHD equations, like MISHKA [45] or ELITE, and furnish the structure of unstable modes. To calculate the transport associated one has to use nonlinear codes, like JOREK [46], which needs huge calculation time resources, or to use hybrid models like IMEP [47], which couples linear analysis of the stability with an algorithm for the turbulent transport model. The latter is much faster, but uses experimental observations, therefore it is not completely based on theory. EPED [48] is another hybrid model which couples the analysis of the MHD stability with a turbulent transport model, making assumptions on the pedestal width, based on experimental observations.

2.4 Transport in the SOL

In a tokamak the boundary conditions at the separatrix are determined by the transport in the SOL. This region is characterized by a complex dynamic, which arises from the interaction between the plasma and the materials which face it. Moreover, here the transport description needs a 2D treatment and the inclusion of neutral atom/molecule species. The main difference between the transport which takes place here and the one in the confined region is the presence of open magnetic field lines. This implies that the particles do not move periodically around a specific closed trajectory but impact on PFCs, delivering heat and particles. Moreover, the temperature of the SOL, which is lower than in the confined plasma, allows lower levels of parallel transport, which are then closer to the perpendicular ones. This does not allow us to treat the perpendicular transport as an average over the magnetic field lines, as it was done in the confined region with the averaged flux surfaces. Nevertheless, experimental observations have shown that physical parameters like collisionality can determine the ratio between perpendicular and parallel transport [49]. It has been observed that the perpendicular transport in this region is associated with the formation of blobs (or filaments) [50], [51], which diffuse radially. These features are still object of study and it is not easy to model them. While these geometrical and physical

aspects represent the main differences with the transport in the confined region, there are several other aspects which make the SOL description complicated. These are explained in the next sections.

2.4.1 Effect of actuators

The actuators can have a strong impact on the evolution of the SOL. For example, changing the species or intensity of the gas puff one can produce different levels of radiation, which can lead to different regimes of the plasma. Then, if this radiation is strong enough, it can in turn lower the temperature near the divertor, increasing the rate of recombination of charged particles. This creates a layer of neutrals in front of the divertor that separates it from the incoming heat and particle flux, which is carried by the open field lines. This phenomenon is known as *detachment*, and it will be necessary in future machine to protect the divertor from the impinging heat fluxes. A picture which shows its front in the HFS (inner divertor) is shown in figure 2.9. In presence of the detachment, the treatment of the

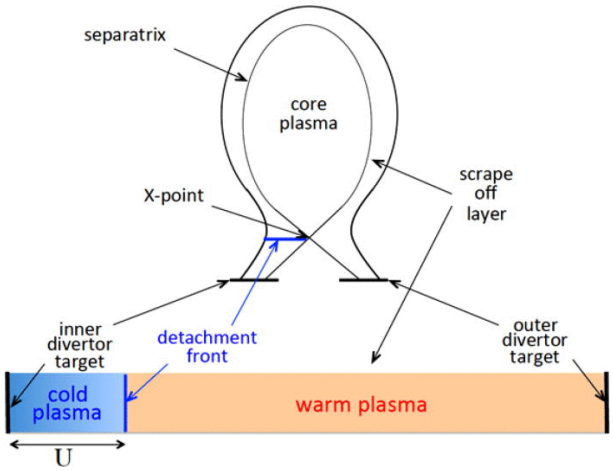

Figure 2.9: Sketch of the detachment in the inner divertor (i.e. in the HFS). The detachment front is shown in blue and it represents the region where a bearing of neutrals is generated, because the radiation front reduces strongly the temperature and increases the recombination rate. This bearing of neutral protects the inner divertor target from heat and particles fluxes. Figure from "S. I. Krasheninnikov and A. I. Smolyakov, Physics of Plasmas 23, 092505 (2016)"

heat transfer is complicated and shows different regions where different mechanisms are dominant. In particular, closer to the separatrix, radiation and convection are dominant, due to the low gradients along the open field lines. A second region is then formed where the radiation is saturated and due to the bearing of neutrals, which physically hampers the passage of charged particles, the conduction is the dominant heating channel.
The detachment is an example of the different regimes which can exist in the SOL during a discharge. As previously mentioned, in order to access such regimes and control them an

important role is played by the manipulation of the engineering parameters. For example, the detachment is obtained experimentally by puffing a large amount of fuel or impurity gas in the SOL. The gas puff can also influence the level of recycling, which is a process that converts charged particles hitting the wall in neutrals and it send them back in the SOL. In particular, the general trend is that increasing the gas puff the plasma goes from low to high recycling regime, and this can generate a high density front in the HFS of the SOL (HFSHDF) [52], [53], [54], around the height of the X-point. In steady-state conditions the percentage of particles which are recycled as neutrals is close to 100%, because the retention of the wall has already reached a saturation and there is no further absorption of particles on it. This means that to control the particle input one must vary the gas puff, so that a balance with the vacuum pump is obtained, without the further sink due to the wall retention. Such control can be used to fix a certain density at the separatrix. This procedure is non-trivial, because there are various recycling regimes of the plasma in the SOL. Another example of the influence of the engineering parameters on the SOL dynamic is the relative sign of I_p and B_t. This affects the drifts, because a change of the sign of B_t will change the sign of the $\boldsymbol{E} \times \boldsymbol{B}$ drift, redistributing the particles along the open field lines in the SOL. This has been found to influence also the performance of the confined plasma, by changing the threshold of the power crossing the separatrix which must be exceeded in order to achieve a H-mode regime [55], [56].

2.4.2 Effects of materials

The dynamic of the SOL is influenced not only by physical parameters and actuators, but also by the material which faces the plasma. For example the level of impurity sputtering, which is the release of material due to the hot ions which hit the wall, depends on the species that hits the PFCs and the material which is hit from these particles. Another example is the initial retention of particles during the ramp-up phase of AUG [57], which is material- and machine-related. Moreover, important instabilities, which set a hard limit for the experiment, are indirectly affected by the wall material. This is the case of the *multifaceted asymmetric radiation from the edge* (MARFE) [58], which drives a radiative collapse with consequent disruption. The detailed evolution of the radiation which leads to this collapse is related to the radiating species, which in turn depends on the material of the PFCs.

2.4.3 Local effects

It has been shown how physical and engineering parameters and PFCs can determine different regimes. This leads to a complexity in the description of the SOL. Another element which complicates the picture is the presence of local phenomena. For example the HFSHDF appears in the HFS and can change in time due to local dynamic and interaction with the surrounding plasma, showing then an asymmetry with respect to the LFS. Moreover, from the technological point of view, the SOL shows different components facing the plasma from different positions (e.g. vacuum pump below the outer divertor leg), which

can vary depending on the machine or the divertor configuration. This supports that the local effects must be taken into account.

2.4.4 General picture

All the explained phenomena show that the SOL dynamic depends on the specific physical and technological peculiarities of an experiment. These aspects can vary between different machines, therefore it is difficult to build a framework general enough to describe the physics of the SOL based on first principles and which does not depend on the specific device. Moreover, within the same experiment there can be different regimes which lead to different evolution of the SOL, affecting also the performance of the confined region. All this evidence suggests that modeling the SOL is a major task which should include a huge amount of technological and physical ingredients, and no complete and unified self-consistent theory exists so far. Despite this, there are several codes which can calculate the transport in this region with assumptions on the physics included (e.g. kinetic drifts, HFSHDF position, radial transport). Such assumptions have often an experimental nature. The most known code is SOLPS-ITER [59], [60], which couples a 2D solver of Braginskii [61] equations (fluid equations, as described in the section of transport, with a specific closure) with a Montecarlo code (EIRENE), which generates a distribution of neutral particles. The simulations performed with these codes have a strong CPU time consumption, due to the complexity of the physics in it, which requires a small time step to reach convergence, especially if the particle drifts are included.
A different treatment of the SOL which includes less physics but can be used to obtain general information about global quantities or boundary condition at the SOL can be a power and/or particle balance. This model has the advantage of being several order of magnitudes faster than the fluid codes. The heat and particle balance is described in the next section.

2.4.5 Heat and particle balance

One possible approach to describe the transport in the SOL is by using an analytical fluid one-dimensional model. In order to simplify the treatment one can neglect sources and sinks of momentum and energy, and cross field transport. However, these assumptions are strong (e.g. because the radiation power in the SOL is non-negligible), therefore the following treatment is an academic derivation, useful to understand the basic principles. The starting point of the model are the equations for the conservation of particles, momentum, and energy, in steady-state conditions:

$$\nabla \cdot \boldsymbol{\Gamma_p} = S, \tag{2.24}$$

$$p_{tot} = m_i n v^2 + p_{stat} = const, \tag{2.25}$$

$$\nabla \cdot \boldsymbol{q} = 0, \tag{2.26}$$

where Γ_p is the particle flux, S is the particle source, n is the plasma density, v is the plasma fluid velocity parallel to the magnetic field lines, the static pressure p_{stat} is equal to $n_e T_e + n_i T_i$ and m_i is the ion mass. The conservation laws describe the dynamic along the magnetic field lines. The conservation of the energy implies that no radiation is present. This is a strong assumption for the SOL, which usually displays the majority of the radiation emitted by the plasma, but it is a good simplified starting point for the development of a theory. The other conservation equations are usually respected but there are cases in which they fail to describe the reality (e.g. in the detached configuration the pressure loss due to the recombination of the ions is non-negligible, i.e. sinks of particles, momentum and energy are relevant).
Due to the fact that the electron mass is much lower than the ion mass, if the temperatures are similar, the velocity is much higher for the electrons and they arrive faster at the target. This implies that the electrons build a negatively charged surface on the target, which hampers the arrival of new electrons until the fluxes of ions and electrons are ambipolar. This generates a change of the electrostatic potential approaching the target from the separatrix. The region in which such potential changes is called sheath. The parallel heat flux at the sheath entrance q_{se} can be expressed as

$$q_{se} = (\gamma_i T_i + \gamma_e T_e)\Gamma_{se}, \tag{2.27}$$

where Γ_{se} is the particle flux at the sheath entrance, and γ_i and γ_e are the ion and electron sheath heat transmission factors. Assuming equal temperature between ion and electrons, and introducing a total sheat heat transmission factor $\gamma = \gamma_i + \gamma_e$ the equation can be reduced in

$$q_{se} = \gamma T \Gamma_t, \tag{2.28}$$

where $\Gamma_t = \Gamma_{se}$. The electric potential, together with the ion inertia, connects the ion and the electron dynamics, through the condition of ambipolarity, which means that the electron and ion particle fluxes must be equal. This condition arises from the combination of particle momentum conservation and quasi-neutrality.
It is useful to define two crucial points in the SOL to set a balance and calculate quantities which can determine the regime of the plasma and the boundary conditions for the confined region. These are the upstream point, which is the outer-mid-plane (OMP, i.e. the position which is found crossing the separatrix horizontally from the magnetic axis), and the target point (i.e. the striking point of the divertor). To refer to the former the index (u) is used, while for the latter (t) is used. Under the assumption of null upstream plasma velocity, sound speed at the target and equal temperature for electrons and ions, from the conservation equations (and ambipolarity condition) a relation between upstream and target static total pressure can be found:

$$p_{stat,u} = n_u T_u = 2 n_t T_t = 2 p_{stat,t}. \tag{2.29}$$

The parallel heat flux can instead be decomposed into convective and conductive terms for ions and electrons. The former can be expressed as

$$q_{i,e,conv} = \left(\frac{1}{2} m_{i,e} v_{i,e}^2 + \frac{3}{2} k T_{i,e} \right) n_{i,e} v_{i,e}, \tag{2.30}$$

where the subscript i, e refers to either ions or electrons, while the latter is given by Spitzer-Härm conductivity [62]

$$q_{i,e,cond} = -k_{i,e} T_{i,e}^{\frac{5}{2}} \frac{dT_{i,e}}{dx}, \tag{2.31}$$

where $k_i = 60\, W(eV)^{-\frac{7}{2}} m$ and $k_e = 2300\, W(eV)^{-\frac{7}{2}} m$. The assumption of null upstream plasma velocity made earlier to obtain equation 2.29 translates in null particle flux in the same point. In the absence of particle sources (i.e. stationary case without sources and sinks) this would mean that there is no particle flux along the field lines. We remind also that in absence of radiation the parallel heat flux is conserved. Under these conditions the heat flux is carried only by conduction through the temperature gradient, thus one can integrate equation 2.31, and relate T_u and T_t with the equation

$$q_{\parallel} L = k_e \frac{2}{7} (T_u^{\frac{7}{2}} - T_t^{\frac{7}{2}}), \tag{2.32}$$

where L is the length of the magnetic field line from the OMP to the divertor. The conductive ion heat flux has been neglected due to the much lower value of k_i respect to k_e. This treatment with these specific hypothesis is known as *2-point model* and it is well established in the literature [63], [64]. In many cases one can assume T_t negligible with respect to T_u. This means that the equation 2.32 can simply be expressed as

$$T_u = \left(\frac{7 q_{\parallel} L}{2 k_e} \right)^{\frac{2}{7}}. \tag{2.33}$$

The upstream temperature T_u has a weak dependence on the parallel heat flux and the connection length. This means that the upstream temperature changes slightly depending on the operating conditions, that has been also verified experimentally. Typical AUG upstream temperatures are usually measured in the order of $T_{e,u} = 100eV$ for plasmas in H-mode and $50eV$ in L-mode. In order to estimate the separatrix density $n_{e,u}$ an extension of the two point model can be used [65] with the following formula

$$\begin{aligned} n_{e,u} =& 0.35 \frac{2}{e} \left(\frac{2}{7} \frac{k_0 k_z}{\pi q_{cyl}} \right)^{\frac{2}{7}} \left(\frac{m_D}{2} \right)^{0.5} R^{-0.5} \left(\frac{P_{SEP} B}{3\pi < \lambda_{q,HD} >< B_p >} \right)^{\frac{3}{14}} \\ & [\gamma sin(\alpha)]^{-0.5} p_0^{0.25} (1.5 \cdot 10^{23} \frac{Pa}{atm^{-2} s^{-1}})^{0.5}, \end{aligned} \tag{2.34}$$

where $k_z = (0.672 + 0.076 Z_{eff}^{0.5} + 0.252 Z_{eff})^{-1}$ is the finite-Z correction of the electron parallel conductivity [66], P_{SEP} is the power which crosses the separatrix, m_D is the main ion mass (D was used in the derivation of this formula), $< \lambda_{q,HD} >$ is the power decay length from [67] (which is the length by which heat flux is reduced by a factor e), α is the impact angle of the magnetic field lines at the outer target and p_0 is the divertor neutral pressure. Its value, which is the dominant in the formula, can be considered as an engineering parameter, because it is determined by the balance between gas puff and vacuum pump, when the wall retention is saturated.

The main limit of the 2-point model is the assumption of no radiation between OMP and the target. This implies that configurations like high recycling regime or detachment can not be reproduced. Also, the assumption of conservation of momentum is limiting the description of the detached regime. Moreover, the assumption of a pure conduction between the separatrix and the divertor is restrictive. A similar but more detailed 0D model based on a power balance between OMP and target, including radiation and a convection-dominated region close to the divertor has been developed in [68]. Nevertheless, few coefficients have been calibrated in this model, that means that it is not completely physics-based. Finally, this model is widely used for AUG in stationary conditions (e.g. during a flattop), but the hypothesis made are too restrictive to allow its usage in any transient condition (e.g. ramp-up), or in the modeling of the SOL of a different machine. For this reason, in this thesis a new model, which will be described later, is developed to be employed in the Fenix flight simulator.

Chapter 3

ASDEX Upgrade

ASDEX Upgrade (AUG) is a medium-sized tokamak located at the Max-Planck-Institute for Plasma Physics in Garching. Its wall is made of Tungsten coated tiles and it has a lower divertor. A picture of it is shown in figure 3.1. AUG started operating in 1991,

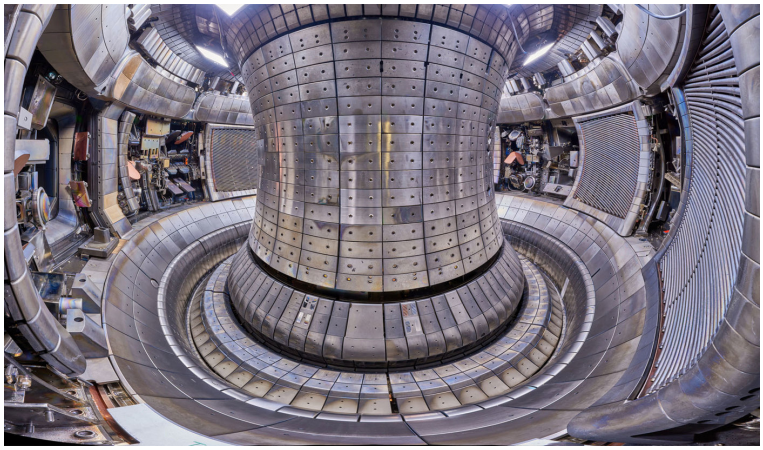

Figure 3.1: ASDEX Upgrade vessel.

after the end of the experiment of the ASDEX tokamak, which was operating from 1980 to 1990. Several typical AUG operational parameters are listed in table 3.1. The AUG tokamak has the highest ratio of the heating power to the size of the machine, which makes it an important experiment for the plasma scenario development of future reactors [3]. The heating systems consist of ECRH, NBI and ICRH. In particular there are 8 ECRH gyrotrons, each delivering maximum 0.6 MW of heating power for a total of 5 MW, 8 NBI boxes, which can provide up to 2.5 MW each for a total of 20 MW, and 4 ICRH generators, heating the plasma with 1 MW each for a total of 4 MW. The NBI boxes have different orientations, so that they can release the power in different radial position (in particular 4 beams provide heating power on-axis and 4 off-axis). The ECRH system uses metallic mirrors which can change the heating positions by deflecting the angle of the beam. The position of the ICRH antennas is fixed and the location of heating power deposition can

Parameter	Value
major radius (R)	1.65 m
minor radius (a)	0.5 m
plasma current (I_P)	0.6 - 1.2 MA
toroidal magnetic field (B_T)	1.5 - 3.2 T
maximum ECRH power	5 MW
maximum NBI power	20 MW
maximum ICRH power	4 MW

Table 3.1: Typical operational parameters of AUG.

vary depending on the frequency of the wave and the magnetic field.
In AUG several scenarios can be explored by running discharges during the experimental sessions. Within the experimental day, a typical discharge which is always executed is the *standard H-mode*, which is a long stationary H-mode without seeding (i.e. puffing of species different from the main ions). This pulse is always run with very similar parameters, in order to test the various systems and calibrate the diagnostics.

3.1 Diagnostics

In AUG there are several available diagnostics to measure different plasma parameters. In particular in this thesis it has been made use of the density and temperature measurements in order to validate the integrated transport model. For the electrons the Integrated-Data-Analysis (IDA) [69] has been used to fit the profiles of density and temperature through a collection of signals from different diagnostics. IDA consists in an algorithm which uses Bayesian inference to set a criteria through which a priority of signals is built and a hierarchy of them returns a specific profile. The main diagnostic involved in the IDA fitting procedure is the Thomson Scattering signal (VTA) [70]. Its working principle is the scattering of electromagnetic waves emitted by a laser on charged particles. The frequency of the scattered radiations is shifted due to double Doppler effects, and the information about it can be related to density and temperature values. In particular, from a specific line of sight the scattered radiation will show two main gaussians around two frequency peaks, which are due to the collisions with particles going in the same and in the opposite direction of the radiation beam. The velocities of such particles will cause a Doppler effect on the scattered radiation, which will shift the peaks of the frequencies. If the temperature is high, the thermal velocity of the particles is high, therefore the frequency shift related to the Doppler effect increases. By considering different lines of sight one can build the profile of electron temperature.
For the ions the main diagnostic involved to measure the temperature profile is the Charge-Exchange Recombination Spectroscopy (CXRS) [71]. This diagnostic is based on the charge exchange processes between neutral atoms, injected by NBI, and ions present in the plasma. The electron captured by the impurity during this reaction stays for a short time in the

excited state and then has a radiative decay during which the light emitted is analyzed spectroscopically, with the same procedure explained for the VTA (Doppler effect).
The measurement of the main ion density is a complicated task, and can be obtained only indirectly through measurements of impurities and Z_{eff}. However, Z_{eff} can be measured only as radial average. Therefore, in order to derive the main ion density a constant Z_{eff} profile must be assumed. This implies that the main ion density profile measurement is not always realistic.
Other fundamental diagnostics of a tokamak are the magnetic probes, which provide information on the magnetic field, from which it is possible to reconstruct the magnetic flux surfaces. The equilibrium codes often use as input the measurements of the magnetic probes located in the vacuum vessel surrounding the plasma to calculate the solution of the Grad-Shafranov equation. This technique provides also information on other important quantities, like the plasma current, shape and stored energy W_{MHD}.
There are many others diagnostics available (e.g. Helium and Lithium beams, electron cyclotron emission, interferometer and bolometer), which are particularly important to measure other quantities (e.g. rotation, radiation or energy) or in specific regions (e.g. the edge). However, their description is well beyond the scope of the thesis, because the prediction of the parameters evolution in the flight simulator should be done without experimental input. The role of the measurements in this thesis is therefore reduced to the validation of the theoretical model, but it is not important for the flight simulator itself.

3.2 Control system

A tokamak is a complex system which involves a high number of variables and processes, that can interact and influence each other. Therefore, a deep physical knowledge of such processes is not enough to run an experiment, but a sophisticated control system is also necessary to handle them in a safe way. This control system is necessary not only to coordinate the different systems involved in the experiment, but also to have stable operation and to protect the device from the hot plasma or the actual heating system (e.g. when the plasma has too low density, the heating systems are shut off automatically). ASDEX Upgrade has its own system, which is called Discharge Control System DCS [11]. The DCS provides all the necessary functions to run discharges, coordinating measurements and actuators to control the evolution of the plasma and optimise its behaviour. These functions include classical feedback controllers, which are based on ad-hoc parameter corrections to follow a prescribed quantity of a variable. The pulse supervisor has the role of handling the exceptional situation (e.g. Shattered Pellet Injection, SPI, which is a system that injects a big quantity of pellets to reduce the impact of disruptions on the machine). Therefore, the control system and the pulse supervisor rule how the conditions of the experiment must be dynamically changed to meet physical goals and correctly reproduce the expected trajectories of the global parameters during a discharge. Modeling this task is the main application of the flight simulator and must be correctly done to reproduce the evolution of a tokamak discharge.

3.2.1 Feedback Controller

The task of a feedback controller is to keep a process variable close to a fixed value, called setpoint. In order to do this the controller takes as input the difference between the actual value of the variable and its setpoint and intervenes on the process through an actuator to reduce this difference. Other controllers can include more sophisticated algorithms like the Partial-Integrated-Derivative (PID). This algorithm looks at the current value of the error $e(t)$ (i.e. the difference between the actual value of the process variable and its setpoint), its integral over a recent time interval, and its time derivative to determine not only how much of a correction to apply, but for how long. Those three quantities are multiplied by tuning constants, which are K_P, K_I and K_D, and summed together to calculate the output of the controller $u(t)$ according to equation 3.1.

$$u(t) = K_P e(t) + K_T \int_0^t e(t)dt + K_D \frac{de(t)}{dt} \tag{3.1}$$

If the current error is large or has been sustained for long time or it is changing fast suddenly, the controller will apply a large correction by generating a large output respectively due to the proportional, integral or derivative part, to regulate the process in a more advanced way respect to the simple proportional case. Conversely, if the variable has matched the setpoint for some time, the controller will have memory of it and will not act for a small and/or slow disturbance. A picture of the working principle of PID controller is shown in figure 3.2. Most of the controllers in AUG have only a proportional and integral part, i.e. they are PI controllers.

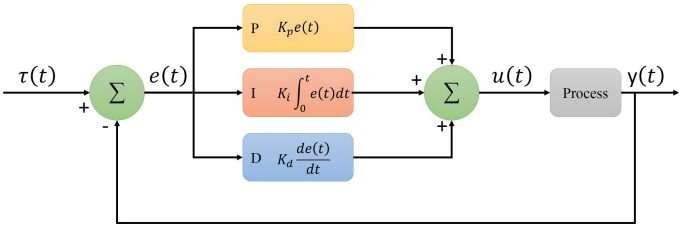

Figure 3.2: Sketch of the working principle of the PID controller. The variable process $\tau(t)$ is compared with the setpoint to obtain an error $e(t)$. This error is then fed to the PID algorithm, which calculates the sum of the proportional part (yellow box), the integral part (red box) and the derivative part (blue box), whose result is the controller output $u(t)$. This is then fed to the actuator and if it exceeds a value fixed by a criteria the actuator acts on the process, trying to modify the process variable, which is then compared back with the setpoint value in a loop.

3.2.2 DCS

The working principle of the DCS is described in the following. A certain wide collection of signals is obtained and elaborated by different diagnostics, leading to information about

the plasma, like the geometry of the separatrix, the radiation or the heat flux profiles. These signals are then compared with the expected/prescribed quantities (i.e. setpoints), within a certain tolerable range. This comparison takes place through control algorithms, which set the rules by which the quantities are acceptable or must be changed in specific ways. The output of these algorithms decides the action on the actuators, which through different mechanisms adjust the engineering parameters (e.g. GP, heating, pellet injection) to make the initial measured quantities closer to the setpoints. Then the sensors measure the new values of these quantities after the regulation and close the loop with eventual new changes. Therefore, the feedback loop is a system which takes several measured outputs of the plasma and compare them overall with the requested values, adjusting them via actuators, according to the control algorithms. The scheme of DCS is shown in figure 3.3. Here one can see the measured values from the diagnostics in the blue boxes, the con-

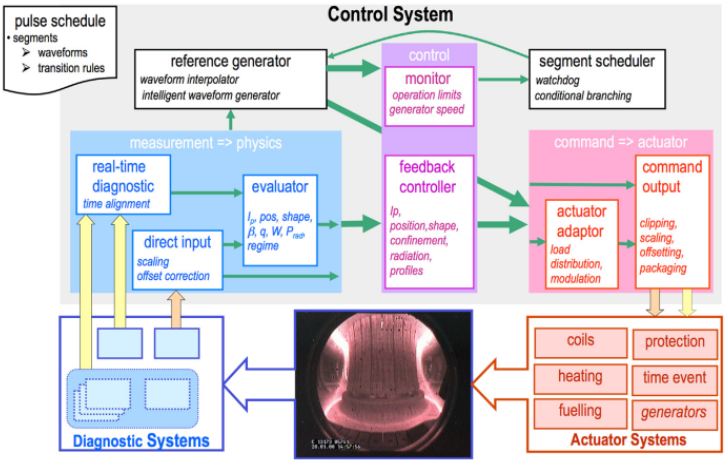

Figure 3.3: Block scheme of the working principle of the AUG DCS. Figure by *W. Treutterer et al. Fusion Engineering and Design 89 (2014) 146–154*

trol algorithms in the magenta boxes and the actuators in the red boxes. Another group of boxes is shown in white and this represents the reference generator and the segment scheduler. These last tools, in the standard conditions of a discharge, have the function to translate the information to make them readable by the control algorithms, but in unexpected situations (e.g. an unpredicted MHD activity) or identified events it can change the pulse schedule (i.e. the previously planned temporal trajectory of the parameters involved in the discharge), selecting other segments which lead to a new state of the machine, in order to reduce eventual damages or terminate the discharge earlier. The input data of the DCS are collected and elaborated by diagnostics in parallel to increase the speed (i.e. must be in real-time). Then the control of elementary plasma parameters like current, position, shape, pressure, density and radiated power provide the fundamental ingredients to obtain stable experimental conditions in the presence of external perturbations. There are also nested control schemes for advanced tasks like plasma current shaping or MHD stabilisation [72, 73, 74]. The DCS allows also usage of feed-forward, that is based on a

different approach, in which the evolution of a specific actuator is not varied to actuate control on other parameters, but it is prescribed. The presence of limits on the maximum or minimum achievable value of different crucial parameters are also included in the DCS, in order to increase the level of safety and to reduce eventual damages. The complexity of the plasma makes particularly hard its control, especially when different operational regimes take place during the same discharge, but the modularity of the DCS opens up the possibility to develop new control algorithms which can be implemented and connected with each other without changing the background infrastructure. In fact the plasma can experience different states (e.g. L-mode, H-mode) which can need control on different parameters or through different criteria. This is the reason why the control system of the plasma includes from simple proportional to highly nonlinear controllers, based on the different assigned tasks and states of the machine, which can alternatively work within the same pulse schedule. Including the features described previously, the DCS has been tested and validated in AUG [75].
In [76] details about how DCS has been generalized to simulate the control system of any thermonuclear fusion experiment are described. In order to do this, one needs to switch between different ad-hoc features, which are related to different devices. This last role is absolved by the Application Processes (APs), which have a costum domain (i.e. they contain machine related aspects which can be specified by the users, e.g. feedback controllers or plasma reconstructors). These can elaborate the data input, which can be customized depending on the machine in which the control system is implemented. At the same time APs use and access common resources like time, protection system, memory storage or networks only via abstract framework interfaces. However, the APs alone are not enough to generalize the control system to any device, because some common resources of the abstract framework interfaces are not valid for all the machines. Moreover, the pre and post discharge procedures can differ a lot between different experiments. Through a segregation of site-specific aspects of APs and background framework interfaces, together with the definition of new flexible interfaces which can adapt to different experiments, there is a possibility to extrapolate the control system to other machines. This is particularly attractive in the prospective of devices of new generation, like DEMO, and it opens up the possibility to set up a flight simulator also for such devices.
In [75] it is also mentioned the possibility to design the control system evolution of a discharge through the implementation of a block diagram programming tool, like Simulink®. This is particularly interesting for the purpose of this thesis, because it has proved the feasibility of a tokamak flight simulator. More details about how its control system is modeled are given in the next chapter, together with the description of the framework in which the physics models are developed.

Chapter 4

The Tokamak Flight Simulator

In order to describe the tokamak flight simulator, it is useful to look at an analogy, for example the usual flight simulator employed for planes. Its many uses can be summarised as: training, checking the flight plan, testing new flight modes. In our case, in a similar way, the tokamak simulator can be validated on existing discharges, checking the evolution of the plasma parameters, and it can be tested on new pulses.
Experimentally, a tokamak plasma is executed using a Discharge Program (DP), that is a list of instruction that the machine processes to create the plasma conditions and perform the discharge, optimally achieving the foreseen physics goals. Typically, parts of older discharge programs from previous pulses, which describe a similar scenario, are recycled, in order to assemble a new discharge program. Sometimes these DPs come from pulses performed years earlier. This process is error prone. In fact, a wrong configuration can cause a lack of plasma performance, a deviation from experimental goals or a plasma disruption. If this happens, the discharge has to be analysed, refined and run again. Moreover, if there are damages, the machine must be shut down to be repaired. Therefore, a tool which can validate by a simulation a designed and prepared scenario is necessary to reduce the loss of experimental time.
This can be done by the tokamak flight simulator Fenix [8, 9], which is a suite that calculates the evolution of a plasma discharge by coupling a model that simulates the control system with a transport code. These two models interact by giving input to each other. The former is simulated in the framework of the PCSSP [10], which is being developed for ITER, while the latter is calculated in ASTRA [77, 78]. Fenix gives to a session leader the possibility to check whether the pulse will meet experimental goals before its execution. A secondary role is also to develop the control system and to validate physical models. It takes as input the AUG discharge program and checks if the limits on specific parameters are reached during the execution of the pulse. ASTRA describes physically the plasma inside the tokamak (in our case AUG) and simulates idealised diagnostic signals (e.g. temperatures and densities). The code calculates these data from the particle and energy transport in the confined region, but other routines can be used to mimic the dynamic in the SOL and divertor. ASTRA is equipped with the 2D equilibrium reconstruction code SPIDER [79]. The ASTRA framework is an open environment where additional routines can be

developed to simulate other processes (e.g. L-H transition or MHD simplified models). This makes such framework modular and easily updatable. As already mentioned, Fenix is provided with a model of the Discharge Control System (DCS) and AUG actuators. The DCS model elaborates mimed diagnosed signals in output from ASTRA (e.g. kinetic profiles), computes commands for the actuators, which determine new control signals (e.g. heating system or gas puff), that in turn are sent back to ASTRA to close the feedback loop. The DCS has been modeled in Simulink®. It includes controllers for coil currents to control plasma current, position and shape. Other examples of controllers are the gas puff valves and the pellet injector to control the electron density. It simulates also the external heating actuator of NBI, often used to control the feedback on β, and ECRH and ICRH. The next sections are dedicated to the description of the implementation of the control and physics models in Fenix and their interaction.

4.1 Fenix Simulink

The framework in which the model for the DCS has been developed was inspired by PCSSP. Therefore, before to describe the structure of Fenix, PCSSP is shortly introduced in the next section.

4.1.1 PCSSP

PCSSP is an architecture initially built on MATLAB/Simulink®, in order to host models and algorithms to simulate the control system of ITER. Within it there are many intrinsic functionalities, e.g. the user interface, a graphical model editor, model block libraries and other toolboxes, which can ease the process of the control system design. Moreover, PCSSP provides dedicated block libraries for plasma control system, tokamak modeling and event generation. PCSSP is then based on the interaction between a machine and its control system, therefore it must include two main functional blocks related to such elements. These are shown in figure 4.1. In such figure the Tokamak Plant Simulator represents the physical machine, while the Plasma Control System (PCS) simulator is the control system. In figure 4.1 "actuator modules" simulates the actuator responses to commands, "diagnostic modules" simulates the processing of real-time measurements to obtain physical quantities, and the "Tokamak+Plasma module" simulates the combined plasma and device responses after the actuator outputs. The "SDN/CIN" module is implemented to simulate the delays introduced in the transfer of measurement data from the plant to the PCS and the commands from the PCS back to the plant. In particular SDN stays for "Synchronous Databus Network" (i.e. commands & diagnostic data) and CIN means "Central Interlock Network" (i.e. machine protection control data). The "Event Generator" module (EG) has the function of triggering off-normal events in plant during the simulation. Such EGs can be defined by the user, due to the flexibility of PCSSP. PCSSP must include a set of Control Units, which through a specific input/output (I/O) logic actuate specific functions such as feedback control. It also needs an Exception Handling function within

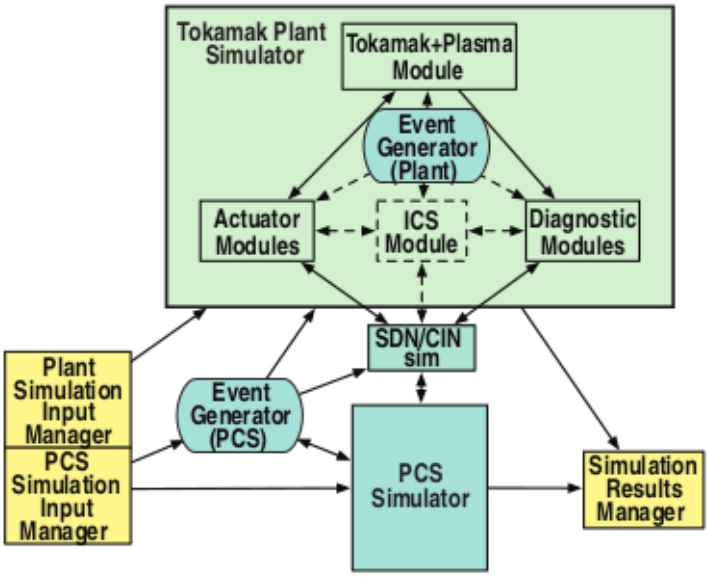

Figure 4.1: Block diagram of the PCSSP architecture, with working principle and connections between different blocks aimed to different purposes. The two main blocks are the green external block (Tokamak Plant Simulator), which represents the physical machine, and the blue block of the PCS simulator, which represents the simulator of the control system. Figure from *M.L. Walker et al., Fusion Engineering and Design 89 (2014) 518–522*

the Event Generator, which reacts to off-normal events with specified responses. Such reactions trigger a change of the control, to switch the Event back to a normal event. In the PCSSP there is also the PCS Supervisor, whose role is to interpret the Pulse Schedule. More information about the mechanism and the details of the Event Generator and the Exception Handler functions are described in [80]. The Interlock Control System (ICS) module incorporates different protection circuits to respond effectively to dangerous events. The "Simulation Input Manager" defines all the necessary data to execute a simulation. Such modules can communicate with the PCS simulator (e.g. to configure data to support iterative algorithm development), or with the plant simulator modules, which configure data to model, when possible, different tokamaks. The Simulation Results Manager is a support to the user during the phase of interpretation of simulation results, and includes data visualization (i.e. scopes), real-time and post-simulation, archiving of simulated data, and data analysis. More details about PCSSP can be found in [10].

4.1.2 Fenix Interface and DCS

Most of the described elements of PCSSP are highly customizable (i.e. can be easily modified) and the open architecture enables users to add their own modules, allowing a strong flexibility and adaptation to different contexts. This has motivated the usage of

such system for the design and development of AUG DCS. In fact, Fenix can directly use PCSSP's Event and Reference Generator blocks with a built-in exception handling, as well as generic feedback controller blocks (e.g. coil currents). However, several custom blocks must be developed for Fenix to model the DCS control system and its interfaces between actuators and diagnostic systems. In other words the general structure of ITER's PCSSP is maintained while implementing such framework in Fenix, but ad-hoc corrections should be included to model the AUG elements which differ with respect to ITER's ones. The custom blocks should represent the real system (AUG), therefore an interface between this framework and the AUG server is provided to obtain the actual parameters of the machine and the values obtained in earlier discharges. To this purpose Fenix can directly parse the DP of a specific discharge. In figure 4.2 the user interface of Fenix is shown. Here

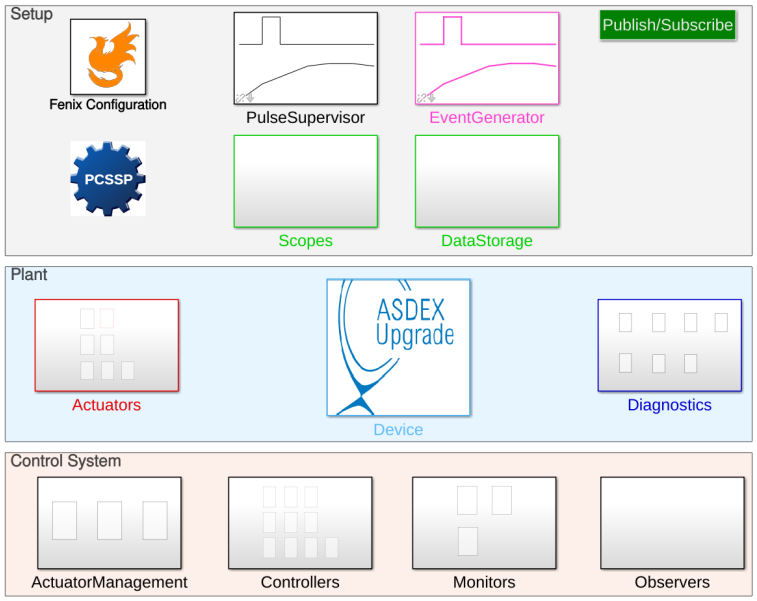

Figure 4.2: User interface of Fenix. From the top, going downwards one finds 3 main macro-blocks, "Setup", "Plant" and "Control System", which deal respectively with the initialization and setting of the simulation, the plant model (in this case AUG) and the DCS model.

one can see different panels and blocks which recall the structure of PCSSP. The 3 main macro-blocks are "setup", "plant" and "control system", which contain respectively all the initial configuration of the simulation, the model of the plant and the control system model. These are furtherly split in different blocks. "Fenix Configuration", "PCSSP" and "Data Storage" contain simply memory-related settings (e.g. sources and storage folders). "Pulse Supervisor" is the "DCS Supervisor" in figure 4.1, "scopes" allows data-visualization functions, while "Event Generator" deals with the exception-handling of unexpected events. In the "Plant" macro-block "Actuators", "Diagnostics" and "Device" represent respectively "Actuator modules", "Diagnostic Modules" and "Tokamak+Plasma module" of figure 4.1. Finally the macro-block "Control System" includes the modeling and connection between

the different parts of the AUG DCS. This block is highly customizable and allows a manipulation by the user in order to simulate different control system configurations.
This is the general picture of the control system model in Fenix. It is necessary to couple such system with a framework in which the physics of the tokamak can be described. This task has been assigned to the ASTRA suite, whose description is explained in the next section.

4.2 ASTRA

As already mentioned, in the flight simulator all the physics models are developed in the framework of ASTRA [77], [78], that is coupled with SPIDER [79], which is a 2D Grad-Shafranov equilibrium solver. ASTRA is a code which solves 1D fluid transport equations, assuming thermodynamical fluxes as composed by a diffusive and convective part. In this code the transport coefficients must be provided by external models. In many applications quasi-linear transport models are coupled with ASTRA for the computation of the diffusivities [22, 23, 20], but in the context of a real time or inter-discharge predictive simulation such models are too slow.
ASTRA is used to calculate the kinetic profiles from the magnetic axis to the separatrix. The strength of this code is its flexibility, which allows to choose which profiles should be kept fixed (e.g. equal to the experimental measurements), and which should be self consistently calculated, where should be assigned the boundary conditions and how they should be calculated, how dense is the grid on which transport is computed, how many species (including impurities) should be included. In a flight simulator all the profiles should be calculated and there should not be any experimental input, so that the prediction of a discharge evolution is not based on experimental assumptions. This implies that in this work we have calculated the heat and particle transport equation for all the ions (H, D, He, B, N, Ne, Ar, Kr, W). Nevertheless, the concentration of most of the species is extremely low in the discharges simulated in this thesis (i.e. only D, B and W have a non-negligible density). For the electrons species, the heat transport equation is solved, whereas the particle density is assigned via quasineutrality, according to

$$n_e = \sum_i Z_i n_i. \tag{4.1}$$

Considering that the last point of the ASTRA grid is the separatrix, the boundary conditions of density and temperature of the various species must be assigned at this coordinate. Such boundary conditions can in general be assigned based on experimental observations. Nevertheless a prediction of these values based on simple models, which can simulate the evolution of the SOL in a simplified way, can be introduced and validated through the implementation of subroutines which do not have spatial definition (i.e. they are 0-D and return time traces). As for the heat and particle transport also the calculation of the current (or magnetic flux) transport must be provided, in order to assure full predictivity. In this work the momentum transport equation is not evolved and the toroidal rotation is

assigned.
The following part of this section describes the main equations adopted by ASTRA to compute the radial plasma profiles. A more detailed derivation of such equations can be found in [77].
The poloidal flux transport equation reads

$$\sigma_{\parallel}\left(\frac{\partial\psi}{\partial t}-\frac{\rho\dot{B}_0}{2B_0}\frac{\partial\psi}{\partial\rho}\right)=\frac{J^2R_0}{\mu_0\rho}\frac{\partial}{\partial\rho}\left(\frac{G_2}{J}\frac{\partial\psi}{\partial\rho}\right)-\frac{V'}{2\pi\rho}(j_{BS}+j_{CD}). \tag{4.2}$$

Here $\sigma_{\parallel}$ is the parallel conductivity, J is defined as $\frac{I}{R_0B_0}$ (where 0 indicates the reference value), G_2 is a metric coefficient, defined as $<|\nabla\rho/r|^2>V'/(4\pi^2)$, V is the volume, j_{BS} is the boostrap current and j_{CD} is the current driven by non-inductive auxiliary sources (e.g. NBI or ECRH). The previous equation can be rewritten as

$$j_{\parallel}=\sigma_{\parallel}E_{\parallel}+j_{BS}+j_{CD}, \tag{4.3}$$

where $\sigma_{\parallel}E_{\parallel}$ is the the induced resistive current and $j_{\parallel}$ is the total parallel current. The equation 4.2 allows the calculation of the time evolution of the total plasma current, which is crucial in time-dependent simulations, to reproduce the temporal evolution of the discharge. In this work the parallel conductivity and the boostrap coefficients are calculated with the formula derived in [17], while j_{CD} must be calculated together with the external heating sources in a consistent way. To this purpose TORBEAM [81] for ECRH and RABBIT [82] for NBI have been coupled. These modules require as input all the engineering parameters of the heating systems (e.g. power, injection angles, frequency of the ECRH gyrotrons, voltage of the NBI beams, etc.) and the plasma kinetic profiles, and they return the radial profiles of the heating power densities and driven currents as output. The radial derivatives of the total pressure profile and of the magnetic field are taken as input in the Grad-Shafranov equation, solved in SPIDER. Then SPIDER calculates the plasma magnetic equilibrium for a free plasma boundary (LCFS) at each time step, allowing the calculation of all the metric functions (e.g. G_2 in equation 4.3) which are used as input in ASTRA for the calculation of the transport equations.
The particle transport is described through the flux-surface-average 1D equation

$$\frac{1}{V'}\left(\frac{\partial}{\partial t}-\frac{\dot{B}_0}{2B_0}\frac{\partial}{\partial\rho}\rho\right)(V'n_j)+\frac{1}{V'}\frac{\partial}{\partial\rho}\Gamma_j=S_j, \tag{4.4}$$

where j refers to a specific species, S_j is the particle source term and Γ_j is the particle flux. The former can be calculated by implementing a module which computes the release due to NBI or gas puff (GP), while the latter can be expressed as

$$\Gamma_j=-n_jV'g_1\left(D_j\frac{\partial n_j}{n_j\partial\rho}-C_j\right), \tag{4.5}$$

where g_1 represents another metric coefficient calculated by SPIDER. Here one can recognize two different terms, which are proportional or independent on the density gradient.

This means that such terms represent respectively a diffusive and a convective coefficient. Finally, the heat transport for a generic species j can be described as

$$\frac{3}{2}(V')^{\frac{5}{3}}\left(\frac{\partial}{\partial t}-\frac{\dot{B}_0}{2B_0}\frac{\partial}{\partial\rho}\rho\right)\left[\left(V'^{\frac{5}{3}}\right)n_jT_j\right]+\frac{1}{V'}\frac{\partial}{\partial\rho}\left(q_j+\frac{5}{2}T_j\Gamma_j\right)=P_j, \tag{4.6}$$

where P_j is the local power density and q_j is the local heat flux, which can be expressed as

$$q_j=-n_jT_jV'g_1\chi_j\frac{\partial T_j}{T_j\partial\rho}. \tag{4.7}$$

In the last equation χ_j is the heat transport coefficient for species j.
Generalizing, the thermodynamical fluxes can be expressed with the equation

$$\phi_j=-C_jV'g_1\sum_i\chi_j^iF_j^i, \tag{4.8}$$

where C_j can be n_j or n_jT_j, depending on whether ϕ_j is a particle or heat flux, χ_j^i is a general transport coefficient for species j related to the thermodynamical drive i, represented by F_j^i, as in

$$F_j^i=\left(\frac{\partial n_j}{n_j\partial\rho};\frac{\partial T_j}{T_j\partial\rho};\frac{E_\parallel}{B_p}\right). \tag{4.9}$$

Such formulation of the fluxes emphasizes the relation between thermodynamic drives and fluxes for different species (i.e. ion gradients can drive electron fluxes and viceversa) and different quantities (i.e. density gradients or electric fields can drive heat fluxes). These terms of the equations are usually addressed as off-diagonal terms or "crosstalks" . As already shown, in our work these have been neglected with respect to the on-diagonal terms (i.e. in equation 4.7 $\chi_j^i\neq 0$ only for $j=i$).
The transport coefficients (i.e. the heat and particle diffusivities, and the particle pinch) are given by the sum of the neoclassical components (calculated with simplified formulae [12, 17, 85, 86]), and the turbulent components, whose model has been the task of this thesis. The external power and particle sources are self-consistently calculated by the corresponding modules previously discussed, which are included in ASTRA.
The turbulent transport models developed in this work have an analytical nature, which allows to be fast. In particular, the time step, which is 0.2 ms, acts effectively as the iteration parameter, and it allows for instantaneous profile relaxation below the physical confinement time. The kinetic profiles, calculated in ASTRA as previously discussed, are then manipulated in order to derive other quantities, which are sent to the AUG DCS modeled in the Simulink®environment, in order to simulate the diagnostic of the plant and provide some values as input for the actuators. Then, the variation of the actuator commands is in turn calculated as response and it is sent back to ASTRA as modification of several inputs (e.g. heating systems or fueling). This interaction between the two frameworks proceeds for the entire discharge duration, predicting the plasma and control system evolution, according to the discharge program, the exception handling and the

controllers, which can also be manipulated by the user for testing purposes. In this context the highly flexible modeling framework enabled by the ASTRA transport code, based on a workflow which allows the description of the coupling between SOL, pedestal and core, with a self–consistent treatment of the boundary conditions, allows the implementation and test of different physics models. The next chapter describes in detail all the physics models developed and tested in this thesis.

Chapter 5

Description of the Integrated Model

In order to reproduce the temporal evolution of a tokamak plasma, an integrated transport model which couples the confined and unconfined regions is developed, assuring then the transport predictivity and the capability to derive information about the confinement. As already mentioned in the introduction, several ways to calculate the confinement and/or kinetic profiles predictions already exist and they differ in level of detail and required computational time. In this thesis, a different approach which requires small computational time and is physics-based has been developed for the tokamak flight simulator Fenix [8, 9], which was described in the previous chapter. In this framework the plasma equilibrium and the control algorithm are already successfully included and tested, while a fully integrated analytical transport model was still missing before this thesis. In fact, as a starting point, Fenix was initially tested with models in which the transport was tuned to match few experimental measurements. However, the models implemented in Fenix should not include any experimental ingredient to provide complete predictive capability. Moreover, the models developed have to be physics based to be realistic, but also fast enough to be used as an inter-discharge prediction tool. This compromise can be reached by employing analytical models which are derived from first principle theories.
The integrated model developed in this thesis, published in [83], includes a set of three physics-based transport models. Two models are applied in the confined region, along the radial grid of ASTRA, while the other two act in the SOL, which is implemented in dedicated subroutines, coupled with ASTRA. These models are linked through the LCFS. In this point the models for the SOL and the confined region give boundary conditions to each other. These fast analytical models have been implemented in the flight simulator, so that it can be used inter-discharges to predict the discharge evolution. In addiction to the transport, a multitude of dynamical processes have to be taken into account, because they can set strict operational limits. For example MHD sets hard limits (e.g. density or β limit), which should not be hit, because they could cause a disruption. Therefore Fenix should be coupled with a predictive model for these limits, in order to allow the avoidance of disruptive cases. Such a model still does not exist, but its development has been planned as future work. A possible simple approach could be to couple Fenix with a space state description which set the conditions for which the plasma hits the hard limits (e.g. high

density limit, like in [84]).
As already mentioned the transport models have been developed in the framework of ASTRA [77], [78], which was described in the previous chapter. ASTRA does not contain any radial grid beyond the LCFS. Therefore, additional subroutines have been coupled, which (virtually) simulate the evolution of the SOL concomitantly with the evolution of the confined plasma. The analytical nature of all the models implies that the transport coefficients do not need iterations to be calculated, that means that all the models proceed concomitantly, interacting with each other through their boundaries. In the following sections a detailed description of the different models developed in this thesis is presented.

5.1 Core Transport

5.1.1 Methodology

The core of a tokamak plasma is usually defined as the confined region, which is the region enclosed by the LCFS. However, in different regimes the plasma can form a pedestal, thus the core can be redefined as the region which goes from the magnetic axis to the top of such pedestal. In this thesis the core has been defined as the region up to $\rho_t = 0.9$. This definition implies the choice of a fixed pedestal width. In fact, this has been chosen equal to 0.1 in ρ_t units. The nature of this choice is related to a numerical aspect: all the simulations run to build up the core transport model were performed along the radius up to $\rho_t = 0.9$, which is the region where the code used to perform such simulations has been already widely validated in earlier works. Other reasons for the choice of the pedestal width will be discussed in the section where the edge model is described.
In the core the plasma reaches the highest values of pressure. In this region, when the kinetic pressure is high enough, the fusion reactions can happen. Nevertheless several dynamics are found to be opposed to the increase of plasma energy, and in some cases they can set a constraint on the maximum reachable pressure and energy. As shown in the theoretical chapter, the main phenomena involved in setting the kinetic profiles are MHD and Larmor-scale instabilities, which drive part of the transport. The transport is split in neoclassical and anomalous part. In order to model the former the formulae from [17], [85] and [86] have been used in Fenix simulations. Nevertheless, this thesis focuses on the anomalous transport. Several fast models already exist and they are based on neural networks (NN), like Qualikiz NN [7]. However, NNs need a training on a wide database which can assure that the model will work properly inside the range of variation of the data collected, but it could be not successful outside it, so its use could be compromised. This is particularly important when one extrapolates to larger devices, that is a crucial problem for machines of next generation. Moreover even if the NNs can provide a correct prediction of transport coefficients, their structure does not offer physics insights. For these reasons in this thesis we have chosen to develop an alternative model, which is based on analytical formulae fitted over a smaller database than the one usually needed for a NN. With respect to NNs, this approach wants to focus on different priorities, like physical

transparency and easier modifiability. With the approximation of local turbulence-driven transport, the coefficients derived in this work are multiplied by a gyroBohm scaling factor, which has been defined as

$$\chi_{gB} = \frac{T_e^{\frac{3}{2}}}{aB_T^2}. \tag{5.1}$$

In order to define the formulae of the transport coefficients the main instabilities affecting the core have to be considered. In this region they are the micro-instabilities driven by temperature and density gradients, which have been introduced in the theoretical chapter. It has been shown first by theory, then by experiments that this transport has a threshold nature [87], [88]. It is also known that there are stabilizing effects on these instabilities (e.g. collisionality, magnetic shear, impurity concentration, β, concentration of fast particles and $E \times B$ shear) [89], [90], [91], [92], [93], [94] and that shape plays a role [95]. Therefore, taking into account all these aspects, different threshold formulae have been adopted for ion temperature gradient (ITG), electron temperature gradient (ETG) and trapped electron mode (TEM) and fitted to a database of TGLF [22], [23], [96] simulations, while Micro-Tearing-Modes (MTMs) [12], [97], [98] have been neglected, because they are usually negligible with respect to the ITG/TEM transport in the core region of AUG. This is not always true, especially in spherical tokamaks [99] or in other configurations with high β, which is the main drive of MTM, or in ITG-suppressed advance scenarios. However, the database used in the fitting does not include such discharges, but the development of a formula to take into account this instability in an extended database of discharges is planned for the future. TGLF simulations were set in this way: saturation rule 2 (which sets a specific rule for the fitting of the quasilinear fluxes of TGLF based on nonlinear gyrokinetic simulations), 3 species (electron, D and B or N, depending on the discharge) and electromagnetic effects. The database consists of the stationary phases of 15 AUG discharges from different scenarios (H-mode, L-mode, I-mode and negative triangularity). Each of these cases has been perturbed in the boundary condition of the kinetic profiles by enhancing/reducing by 10% electron density, electron temperature and ion temperature at $\rho_t = 0.9$. This scan has increased the database and assured that the range of variation of the normalized gradient of the kinetic profiles is covered in a more homogeneous way, with a contiguous spread of the data. This should improve the quality of the fitting. The broad variety of configurations included in the database is largely justified by the general nature of the instabilities treated. In this database 6 coordinates in the range $\rho_t = [0 - 0.9]$ have been considered for the last 20 time steps of the converged TGLF+ASTRA simulations. The simulations included sawteeth, but a strategy to exclude their impact on transport has been used, based on varying the position of the first radial coordinate included in the fitting. Moreover, several coordinates at $\rho_t > 0.9$ for 1 L-mode case where included. Thus, it is possible to use this model in the edge in L-mode configuration, where turbulent transport is still determining the profiles. The database consists overall of 12600 values of χ_e and χ_i, which are respectively electron and ion heat diffusivity.

5.1.2 Analytical Formulae for the Transport Coefficients

The formulae used for the fitting are reported here, in gyroBohm units [100] (i.e. normalized by χ_{gB}, equation 5.1):

$$\hat{\chi}_{i,ITG} = C \cdot H_{ITG} \cdot \left(\frac{R}{L_{Ti}} - \frac{R}{L_{Ti,ITG}} \right)^{\epsilon_{10}} q^{\gamma_q} e^{-\gamma_{\beta_e} \beta_e} k^{-\gamma_k} e^{-\gamma_{imp}(1-c_I)}, \tag{5.2}$$

$$\hat{\chi}_{e,ETG} = D \cdot H_{ETG} \cdot \left(\frac{R}{L_{Te}} - \frac{R}{L_{Te,ETG}} \right)^{\epsilon_{20}} q^{\gamma_{q,e}} k^{-\gamma_{k,e}}, \tag{5.3}$$

$$\hat{\chi}_{e,TEM} = D_2 H_{TEM} \cdot \left(\frac{R}{L_{Te}} - \frac{R}{L_{Te,TEM}} \right)^{\epsilon_{30}} e^{-\gamma_\nu \nu} e^{-\gamma_s s} e^{\gamma_{\delta,e} \delta}, \tag{5.4}$$

$$\hat{\chi}_{e,ITG} = max \left\{ 1, f_t D_3 \frac{L_{Te}}{L_{Ti}} \right\} \hat{\chi}_{i,ITG}, \tag{5.5}$$

$$\hat{\chi}_e = (1 - f_t) \hat{\chi}_{e,ETG} + f_t \hat{\chi}_{e,TEM} + \hat{\chi}_{e,ITG}, \tag{5.6}$$

$$\hat{\chi}_i = \hat{\chi}_{i,ITG}, \tag{5.7}$$

where

$$H_{ITG} = H \left(\frac{R}{L_{Ti}} - \frac{R}{L_{Ti,ITG}} \right), \tag{5.8}$$

$$H_{TEM} = H \left(\frac{R}{L_{Te}} - \frac{R}{L_{Te,TEM}} \right), \tag{5.9}$$

$$H_{ETG} = H \left(\frac{R}{L_{Te}} - \frac{R}{L_{Te,ETG}} \right), \tag{5.10}$$

R is the major radius, $1/L_T = -\frac{\partial_r T}{T}$, q is the safety factor, β_e is the ratio between electronic kinetic and magnetic pressure, k is the local elongation, δ is the local triangularity, c_I is the main ion fraction, ν is the collisionality, defined as $RZ_{eff} n_e T_e^{-2}$ with n_e in $10^{19} m^{-3}$, T_e in keV and Z_{eff} equal to effective charge, s is the magnetic shear and f_t, defined as $\sqrt{\frac{r}{R}}$, is the analogous of the trapped particle fraction, while C, ϵ_{10}, γ_q, γ_{β_e}, γ_k, γ_{imp}, D, ϵ_{20}, $\gamma_{q,e}$, $\gamma_{k,e}$, D_2, ϵ_{30}, γ_ν, γ_s, $\gamma_{\delta,e}$, D_3 are the fitting parameters. H is the heaviside function, whose argument is specified in the parenthesis of equations 5.8, 5.9, 5.10. This structure of the formulae assures the threshold nature of the instabilities.

An important characteristic of the transport in the core is the stiffness, which was already discussed in the theoretical chapter. It is a mechanism by which the transport coefficients depend strongly on the normalized gradients. Such behaviour is assured by the presence of ϵ_{10}, ϵ_{20} and ϵ_{30} in the formulae, as exponent of the differences between the actual normalized gradients and their thresholds. In fact, if these fitting coefficients are positive the transport coefficients increase with the temperature gradients. This means that if the heating power is increased, also the transport increases, and the resulting kinetic profiles are very self-similar, if all the other sources and sinks are kept fixed.

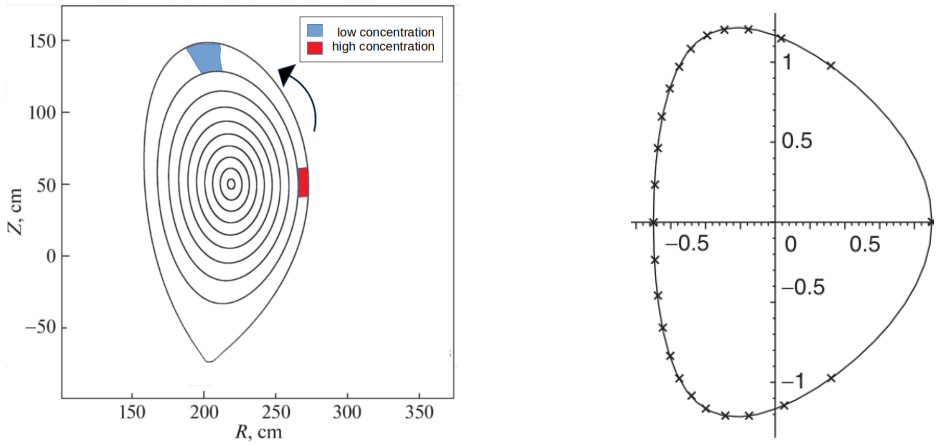

Figure 5.1: On the left an image which shows how the elongation affects the transport. It creates zones with higher concentration, causing a poloidal redistribution which reduces the number of particles in the bad curvature region. On the right the effect of triangularity on the transport is shown. The crosses on the contour of the magnetic surface represent consecutive positions of the particles after the same distance traveled toroidally. The trip of the particles takes place for most of its time in the good curvature region (HFS), reducing thus the transport associated with ballooning instabilities. Figure taken from *"Magnetohydrodynamic Stability of Tokamaks", by Hartmut Zohm (2014).*

As already mentioned, there are many stabilizing or destabilizing effects on these instabilities. A part of these have been introduced in the formulae through the exponentials or the power laws. The electromagnetic effects due to the fluctuations of magnetic fields are included through the β_e term, as stabilization of ITG modes, resulting in an overall reduction of ion heat transport. The shape of the plasma cross section also affects the transport, because it changes the relative length that the particles travel in the high field side (HFS) and in the low field side (LFS), affecting thus the ballooning stability. In particular, the triangularity determines how much time a particle spend in the good and bad curvature region, resulting then in a more or less pronounced associated transport. The shape changes also the local concentration of particles between confining magnetic surfaces, which generates poloidal concentration gradients and subsequent poloidal redistribution. These dynamics are shown in figure 5.1. In order to take into account these effects, respectively δ and k have been included in the formulae. The collisionality is another crucial parameter to distinguish between different instability regimes. In particular it reduces the effect of the trapped particle fraction, through collisions with passing electrons. This in turn results in a reduction of the TEM driven transport. Such effect is modeled in $\hat{\chi}_{e,TEM}$, through $e^{-\gamma_\nu \nu}$. Also the magnetic shear plays a role, because it reduces the transport, through the tilt of the magnetic field lines, which leads to a decorrelation of the neighbouring field lines. This mechanism is visualized in figure 5.2. This means that the radial structures (i.e. eddies) move poloidally with different velocities, until such structures are teared apart. In other words the radial "communication" between particles around a cer-

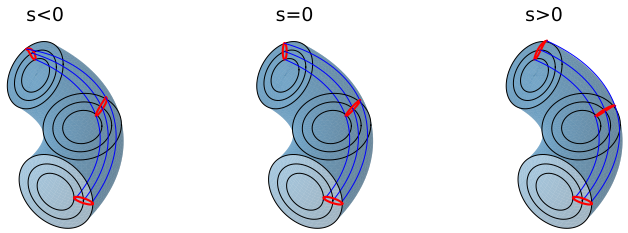

Figure 5.2: The tilt of neighbouring magnetic field lines determines different poloidal velocities of the particles. This generates a deformation of the structures which eventually tear them apart. Figure from "Maximilian Reisner, *Dependence of transport in high-beta low collisional H-modes on ExB-shear and q-profile*, PhD thesis, Ludwig-Maxmilian-Universität (2022)"

tain position is reduced, resulting in a weaker transport. This effect is taken into account through the terms related to s in the formulae. The Landau damping affects the transport through the parallel dynamic, whose importance is determined by the safety factor. This effect is therefore represented by a term related to q in ITG and ETG formulae. Finally, the presence of impurities in the plasma reduces the transport of the main ions, because it represents a sink of energy, depleting passively the active turbulence, without adding other drives. This effect has been taken into account by introducing the term $e^{-\gamma_{imp}(1-c_I)}$ in the formula for $\hat{\chi}_{i,ITG}$.
The time scale of the ITG instability is usually slower than the inertial time of the passing electrons, while trapped electrons move toroidally with a comparable time scale. This implies that the former are adiabatic (i.e. they do not participate to ITG transport), while the latter can be affected by ITG. In order to model the ITG driven electron heat transport $\hat{\chi}_{e,ITG}$ has been introduced. It shows a proportionality with $\hat{\chi}_{i,ITG}$, through the trapped particle fraction and a ratio between electron and ion temperature gradient. This last parameter was introduced to simulate the relative contribution of the electrons to an ionic instability. The linear threshold formulae are available from the literature [101], [102]. For the ETG and ITG thresholds few fitting parameters have been put to multiply the dependencies. The formulae read

$$\frac{R}{L_{Ti,ITG}} = max\Bigg\{A_{10}\left(1+B_{10}Z_{eff}\frac{T_i}{T_e}\right)\left(1+B_{20}\frac{s}{q}\right)\left(1-1.5{f_t}^2\right)\left[1+0.3\left(k-1\right)\right]; A_{20}\frac{R}{L_n}\Bigg\}, \tag{5.11}$$

$$\frac{R}{L_{Te,ETG}} = max\Bigg\{F_{10}\left(1+G_{10}Z_{eff}\frac{T_e}{T_i}\right)\left(1+G_{20}\frac{s}{q}\right)\left(1-1.5{f_t}^2\right)\left[1+0.3\left(k-1\right)\right]; F_{20}\frac{R}{L_n}\Bigg\}, \tag{5.12}$$

$$\frac{R}{L_{Te,TEM}} = 0.357\frac{f_t + 0.271}{f_t}\left[4.9 - 1.31\frac{R}{L_n} + 2.68s + \log\left(1 + 20\nu\right)\right], \tag{5.13}$$

where $1/L_n = -\frac{\partial_r n_e}{n_e}$, while A_{10}, B_{10}, B_{20}, A_{20}, F_{10}, G_{10}, G_{20}, F_{20} are other fitting parameters. The ITG threshold has the same shape of ETG one, with the difference that $\frac{T_e}{T_i}$ is inverted, because in the linear limit the two instabilities have the same physical description [103]. In the threshold formulae the dependence on $\frac{T_e}{T_i}$ takes into account how both the ions and the electrons participate to the dynamic of the instabilities. It is worth to notice that the normalized density gradient is stabilizing for ETG/ITG and destabilizing for TEM, as already discussed in the theoretical chapter. The TEM threshold has been chosen not to contain fitting parameters because there are not many TEM-dominated pulses in the database. The ETG threshold has instead been fitted, because in this way it was found to better match TGLF output. The results of the fitting procedure show stronger dependence on $\frac{T_e}{T_i}$ and lower dependence on s and $\frac{R}{L_n}$ in the linear ETG threshold with respect to the formula from the literature. This effect could be due to a residual presence of $\frac{R}{L_n}$ driven TEM, which is not included in the model. A threshold formula is present in the literature, but the hypothesis under which it is valid are too constraining (no temperature fluctuations). Another cause of the difference between the fitted threshold and the one from the literature could be the shift of the linear ETG threshold due to nonlinear effects. In fact, nonlinearly, the transport can increase due to the formation of ETG streamers [103], [104], [105], [106]. However, TGLF is a quasilinear model, therefore the presence of a nonlinear shift of the ETG threshold could be just the result of the multiscale spectral calibration over the gyrokinetic database fitted to obtain the saturation rule.

5.1.3 Specifics on the ETG database

The simulations used to build up the database for the fitting were performed using ASTRA+TGLF. After running the simulations, the spectra of γ, ω and heat flux vs $k_y\rho$ for each radial coordinate have been analysed to characterize the instabilities. The contribution to the transport from scales in the range of $k_y\rho > 1$ has been found to be at maximum equal to 5%, varying slightly for different conditions and radial positions. Considering that the ETG instability is found only for small scales (i.e. $k_y\rho > 1$) one can conclude that the ETG contribution to the transport is rather low for the discharges included in the database.

This has motivated the creation of a dedicated ETG database, without which it would have been impossible to distinguish the ETG driven transport from the total transport. This has been obtained by multiplying the original database of χ_e in output from ASTRA by $\frac{Q_{high}}{Q_{tot}}$, where Q_{high} is the anomalous electron heat flux coming from $k_y\rho > 1$ transport, and Q_{tot} is the total anomalous electron heat flux over all the spectra. This ratio represents the percentage of electron heat transport due to small scale turbulence. Considering that the temperature gradient is constant over the spectra $\chi_e\frac{Q_{e,high}}{Q_{e,tot}} = \chi_e\frac{\chi_{e,high}}{\chi_e} = \chi_{e,ETG}$, because $\chi_{e,high}$ is assumed to be due to ETG. This should provide a rough distinction between ion

scales and mixed-electron scales, making easier the distinction between ETG driven and total transport. This procedure has therefore led to a disentanglement of the microinstabilities, which are fitted separately, leading to a reduction of degrees of freedom, which goes more into the direction of a physics-based fitting. However, the rough separation between ETG and TEM+ITG contributions made by splitting the spectra in two clear regions is not completely consistent. In particular, a certain amount of TEM and ITG driven transport exist also for $k_y\rho > 1$ scales. To overcome this problem a first fitting on this derived ETG database has been performed by including also $\chi_{e,ITG}$ formula, and it has been seen to match a branch of high $\chi_{e,TGLF}$ values. In fact, a clear difference between the $\chi_{e,TGLF}$ matched by ITG formula and by ETG formula has been found in terms of parameters dependencies and order of magnitude. After this initial test, a filter to separate these 2 branches of coefficients has been put by excluding data with both $\frac{R}{L_{T,e}} < 20$ and $\chi_e > 10$ (in gB units) conditions met, because such conditions are suspected to not belong to ETG unstable cases. Those conditions have been associated with ITG-driven transport. Nevertheless, even after this filter, an unavoidable small residual contribution from TEMs is present in the clean database, due to the fact that this instability appears also on electron scales. The consequences related to this will be discussed in the following.

5.1.4 Results of the fitting procedure

In figure 5.3 and 5.4 the scattering of the fitted coefficients compared to the respective values calculated by TGLF is shown. The red points are the values calculated using the fitting formulae, while the respective TGLF values lay on the black solid line. The coefficients are shown in gyroBohm units. One can see that the general trend is reproduced, and a certain level of scattering should be tolerated considering that the coefficients are taken along the entire radius (up to separatrix in few cases) and the simple structure of the analytical formulae. Nevertheless, few analytical coefficients are severely off the values from TGLF, which is the case of the spot of red points around $\chi_{e,TEM+ITG,fitted} = 10^{-2}$. These cases were investigated to understand the nature of the mismatch. It has been found that the corresponding values calculated in the simulations (2 in gB units, as can be seen in figure 5.3) were at $\rho_t < 0.1$, outside the range in which TGLF is applied (i.e. $0.1 < \rho_t < 1$), and where the transport coefficients were fixed. The means and the standard deviations of the ratios between the fitted and the TGLF transport coefficients for $\chi_{i,ITG}$, $\chi_{e,ITG+TEM}$ and $\chi_{e,ETG}$ are respectively $\mu_{i,ITG} = 1.83$, $\sigma_{i,ITG} = 2.5$, $\mu_{e,ITG+TEM} = 1.4$, $\sigma_{e,ITG+TEM} = 1.226$, $\mu_{ETG} = 1.15$, $\sigma_{ETG} = 1.27$.

Figure 5.6, 5.7 and 5.8 display the wide range of variations of most of the parameters and show that most of the parameter dependencies are well caught, proving the successful performance of the fitting routine. However in figure 5.6.c a branch of analytical χ_i could not match the TGLF values. In fact, in this plot one can clearly see a bifurcation of the dependence of χ_i on $\frac{R}{L_{T_i}}$, where one branch is increasing weaker and the other is very steep. In order to investigate this apparent bifurcation in χ_i with strong $\frac{R}{L_{T_i}}$ dependence, the input parameters of 2 simulations with $9 < \frac{R}{L_{T_i}} < 10$ giving respectively $\chi_i > 50$

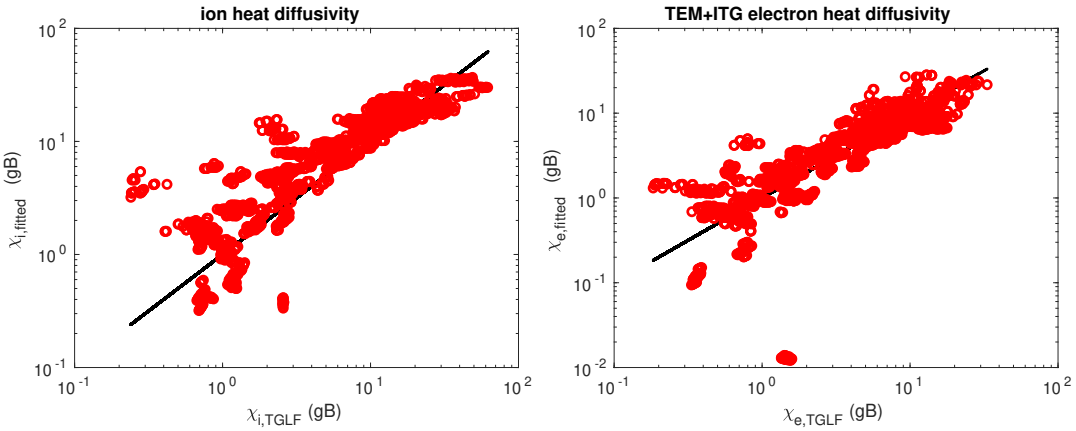

Figure 5.3: Transport coefficients derived by the fitting formulae vs those calculated by TGLF. The red points are the values calculated by the analytical formulae, while the solid line represents the respective values computed from TGLF. On the left is shown the ion heat diffusivity, while on the right the TEM+ITG electron heat diffusivity. The coefficients are shown in logarithmic scale.

and $\chi_i < 40$ were selected and several scans around the nominal input parameters were performed with TGLF stand alone. After a detailed analysis the main reasons of the difference between the transport coefficients in the 2 cases were identified in the different values of collisionality and radial position (and associated trapped particle fraction). In particular, the collisionality of the high χ_i case was 3 times the one of the low χ_i, while the normalized minor radius of the former was 1.5 times the one of the latter. This is not surprising because high collisionality usually drives transport through shifting upwards the saturation level given by zonal flows [107]. However, the similar values of the other parameters (in particular the high value of magnetic shear) should prevent the triggering of an ITG for both the cases, while the TEM should be reduced by high collisionality. The differences between the two χ_i have been compared with two corresponding linear calculations with the gyrokinetic code GENE, using the same input parameters as the TGLF cases. While for the low collisionality case GENE confirms the results of TGLF, in the high collisionality simulations, whose output turbulence spectra are shown in figure 5.5, sensitive differences are found. In particular, the growth rates of GENE has been found similar to the one of TGLF, but a quasi-linear estimate of the ion heat flux using the GENE results and applying a quasi-linear rule which is analogous to that of TGLF yields values which are one order of magnitude lower than TGLF. This result could be due to an overestimation of the quasilinear weight from TGLF or an underestimation of the quasi-linear flux of the linear GENE simulation. An additional TGLF simulation with an increased number of expansion polynomials of the distribution function have confirmed the heat flux overestimation with respect to GENE. A further investigation with nonlinear gyrokinetic simulations would be necessary to understand the reason of the mismatch, but it is well beyond the scope of this thesis. However, the TGLF predicted ion temperature

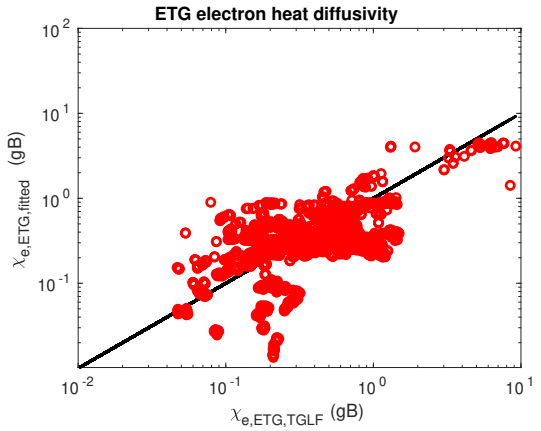

Figure 5.4: Transport coefficients calculated with the ETG fitting model vs those computed by TGLF for $k_y\rho > 1$. The red points are the values calculated by the analytical formulae, while the solid line represents the respective values computed from TGLF. The coefficients are shown in logarithmic scale.

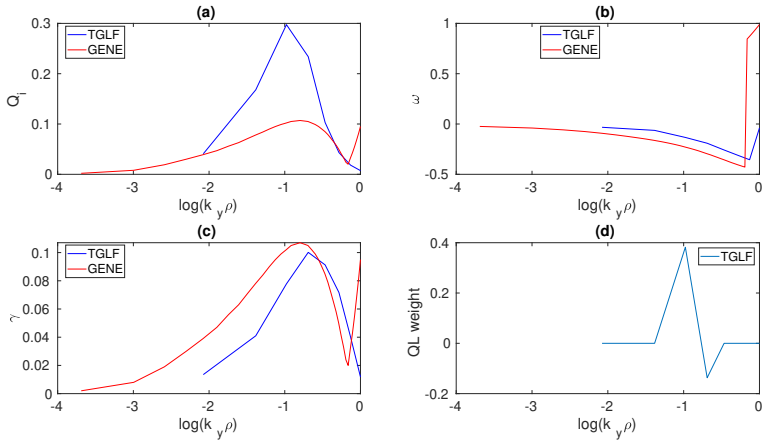

Figure 5.5: Comparison between the turbulence spectra from TGLF and linear GENE simulations for a specific plasma coordinate at high ν and magnetic shear. In (a) is the ion heat flux, in (b) is ω, in (c) is γ and in (d) is the quasilinear weight. In blue is TGLF, while in red is GENE.

profiles in these conditions are significantly below the experimental ones, that means that TGLF does not predict the correct transport coefficients for this case, therefore the branch of TGLF results with $\chi_i > 50$ and $-R\frac{\nabla_r T_i}{T_i} < 10$ has been ignored in the derivation of the analytical model. It is worth to notice that the branch of mismatching χ_i in figure 5.6.c is reflected also on χ_e in figure 5.7.c, through the term $\hat{\chi}_{e,ITG}$ in equation 5.5.
In figure 5.8 each of the 12 plots shows a subset of TGLF χ_e which are not matched by the ETG analytical formula. This is probably caused by a minimum residual of ITG driven transport in the TGLF database used for the ETG fitting. This is supported by the fact

that the trend in $\frac{R}{L_{T_i}}$ is caught except for high values of the normalized gradient, which is consistent with the presence of the ITG. Moreover, the mismatching transport coefficients are underestimated for low values of β, which reduces ITG. Other mismatching χ_e could be due to the presence of TEM driven TGLF transport coefficients, because most of these χ_e mismatch for high value of trapped particle fraction and high value of density gradient which can drive TEM. The presence of residual TEM transport is supported also by the bigger heat conductivities for high $\frac{R}{L_{T_e}}$. As already mentioned, the ETG contribution to the transport was found smaller than 5% for most of the cases, so its relevance is low in this work. A better formulation of the ETG transport, widening the database with ETG dominated discharges, is planned for the future.
The means and standard deviations of $\frac{\chi_{fitted}}{\chi_{TGLF}}$ for different values of the parameters included in the fitting are shown in figure 5.9, 5.10 and 5.11 respectively for $\chi_{i,ITG}$, $\chi_{e,TEM+ITG}$ and $\chi_{e,ETG}$. Here one can see the most critical values of the parameters in which the standard deviation is high, then where the fitting procedure loses quality and does not match the TGLF values.

The output fitting parameters are:

$$\begin{aligned}
&C = 26.15,\ \epsilon_{10} = 0.207,\ \gamma_q = 0.0546,\ \gamma_{\beta_e} = 1,\ \gamma_k = 0.01,\ \gamma_{imp} = 1,\\
&D = 0.116,\ \epsilon_{20} = 1.18,\ \gamma_{q,e} = 0.11,\ \gamma_{k,e} = 0.097,\\
&D_2 = 1,\ \epsilon_{30} = 1.74,\ \gamma_\nu = 0.0035,\ \gamma_s = 0.001,\ \gamma_{\delta,e} = 0.031,\ D_3 = 0.92\\
&A_{10} = 0.227,\ B_{10} = 0.0119,\ B_{20} = 2.645,\ A_{20} = 0.635\\
&F_{10} = 1.8,\ G_{10} = 1.27,\ G_{20} = 0,\ F_{20} = 0.1.
\end{aligned} \tag{5.14}$$

The fitting database used has been built using TGLF with saturation rule 2, but earlier saturation rule 1 has been also adopted, in order to strengthen the fidelity of the procedure used in the model. Also in this case a small scattering of the fitted coefficients around the TGLF values has been found, but the main dependencies are well reproduced by the formulae.

5.1.5 Particle transport

The particle transport prediction is a non-trivial task. In fact, while for the heat transport the diffusion is always the dominant mechanism, for particles both diffusion and convection contribute at a comparable level to the observed density profile. In this thesis an attempt to fit the particle flux in output from the ASTRA+TGLF simulations has been made, by implementing an analytical formula which includes the contribution of diffusivity and pinch normalized to be consistent with TGLF. This formula contains all the main dependencies of the pinch on different parameters. However, the analytical fitted formula has been tested in Fenix without success. In particular, the density profile evolution showed a slowly increasing artificial step at the connecting region between core and edge. This determined a mismatch with the experimental density profile, and the reason for this was identified in an unphysical competition between particle pinch and diffusivity (i.e. too low

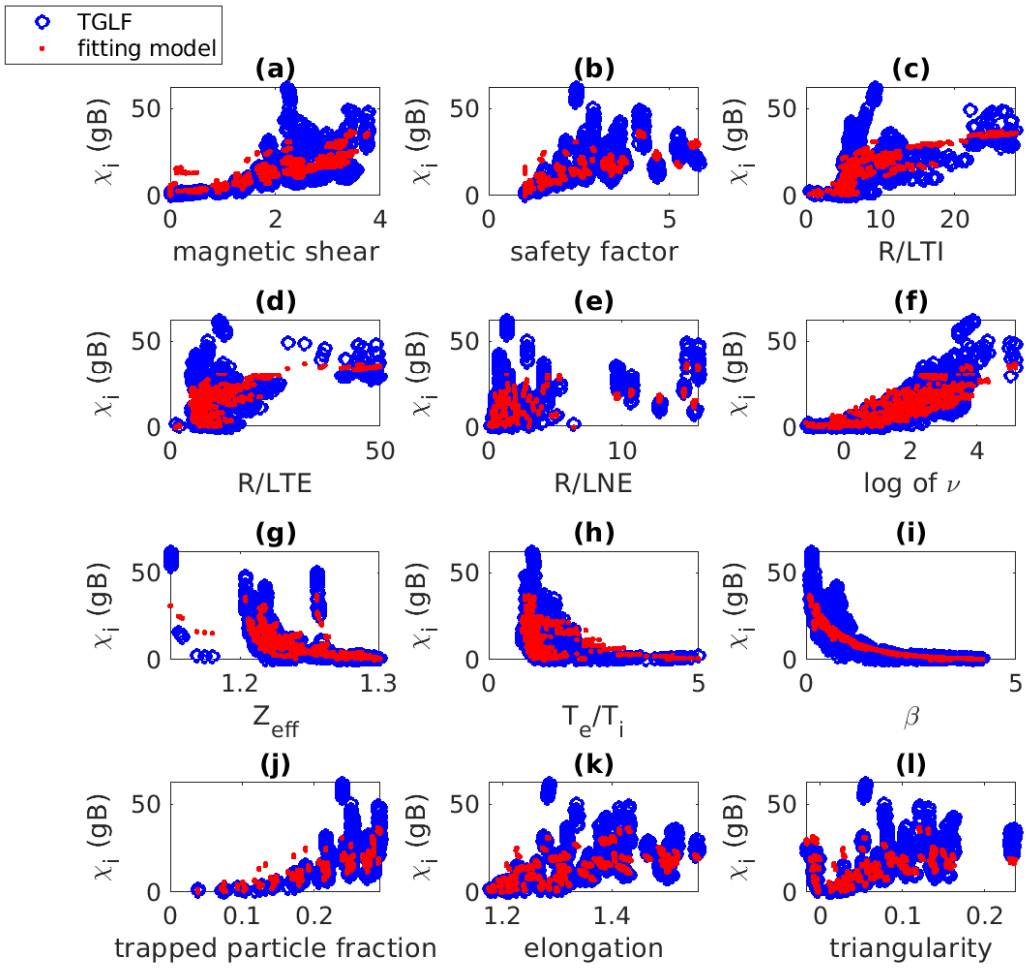

Figure 5.6: Dependency of χ_i on the physical parameters included in the fitting. In blue the values from TGLF database, in red the ones respectively calculated by the fitting model.

diffusivity or too negative convection), which does not let the density relax.
Due to the encountered difficulties, it was decided to adopt a simpler model of particle transport. The particle diffusivity has then been assumed to be equal to $C \cdot \chi_e$, where C is a calibration factor which has been fixed equal to 0.96 to match the kinetic profiles of a discharge, while the particle pinch has been modeled with a heuristic formula which is proportional to diffusivity to assure stationarity and takes into account the effect of L_{T_e}, s and ν [108], [109], [110], [111], [112]. These effects were similar to the ones included in the tested analytical formula, to assure a physics-based nature, even if the self-consistence is compromised.

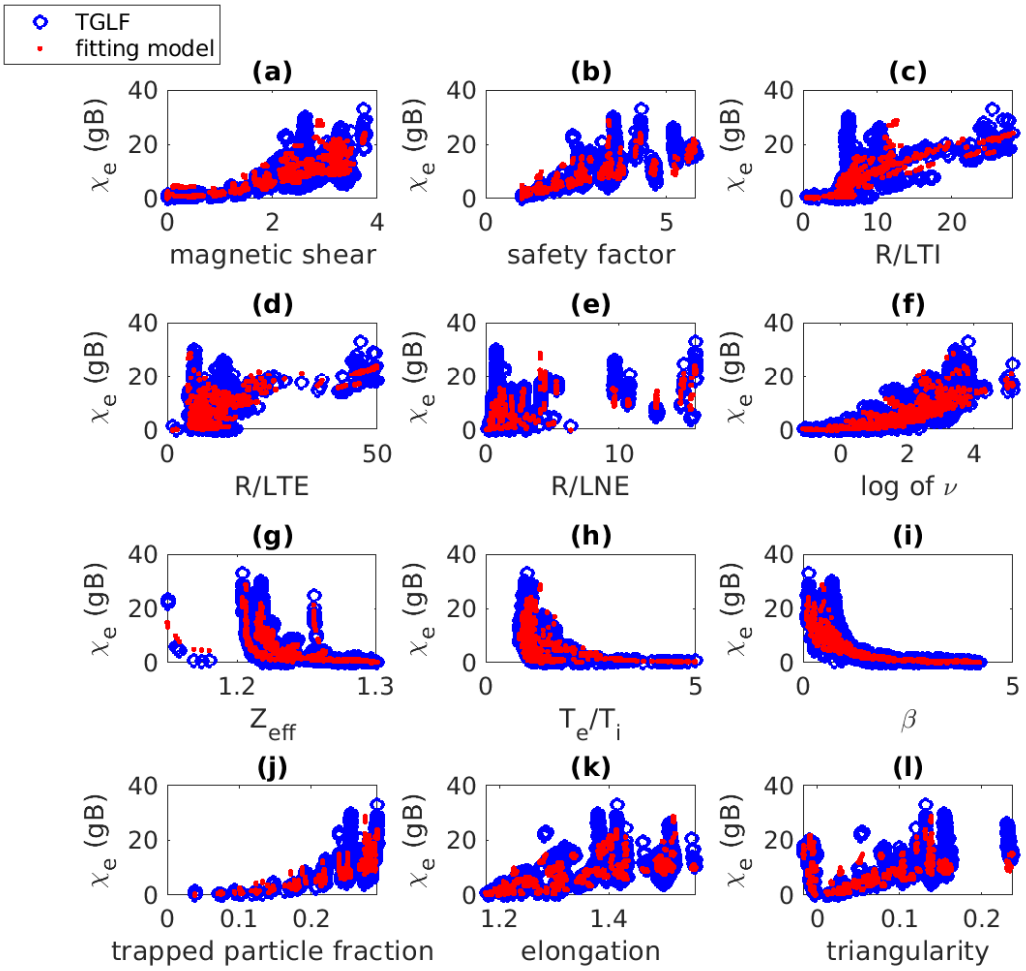

Figure 5.7: Dependency of $\chi_{e,TEM+ITG}$ on the physical parameters included in the fitting. In blue the values from TGLF database, in red the ones respectively calculated by the fitting model.

$$v_p = -\frac{D_n}{R} max\left\{0; 0.2R\frac{|\partial_r T_e|}{T_e} + 0.15s - \nu_{ei}/15\right\} \tag{5.15}$$

The maximum function has been used here to assume a negative convection, that is a pinch, in order to have stationarity through the balance between particle diffusivity and particle pinch. This assumption comes from the observation that hollow density profiles are rarely observed in AUG. As already mentioned, a physics based model for particle transport is a task which has not yet been completed, due to the difficulty of modeling of the particle convection, whose value can change sign locally.

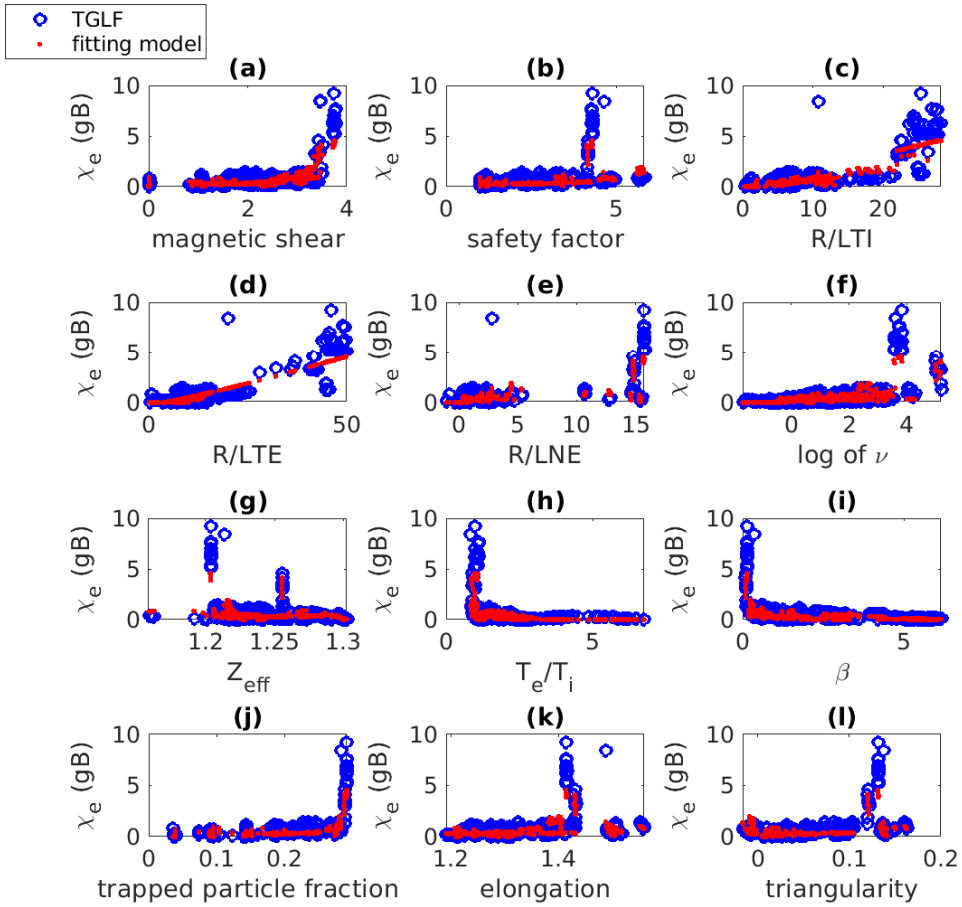

Figure 5.8: Dependency of $\chi_{e,ETG}$ on the physical parameters included in the fitting. In blue the values from TGLF database, in red the ones respectively calculated by the fitting model.

5.2 Edge transport

The transport model described in the previous section is in principle valid for $0 < \rho_t < 1$. However, there are cases in which ad hoc modifications have to be included when dealing with localized regions of reduced transport, such as the Edge Transport Barrier (ETB). In fact, as previously mentioned, when a threshold in the power crossing the separatrix is overcome, the plasma can enter a different state, called H-mode. In this condition, in the region $0.9 < \rho_t < 1$, a pedestal in the temperature and density profiles arises. This pedestal is formed in a small region of the plasma near the LCFS, or separatrix, but it plays an important role, because it sustains up to 50% of the total plasma energy. Within the pedestal the determination of the transport coefficients is complicated, and the description given in the theoretical chapter is not exhaustive. In fact, a combination of

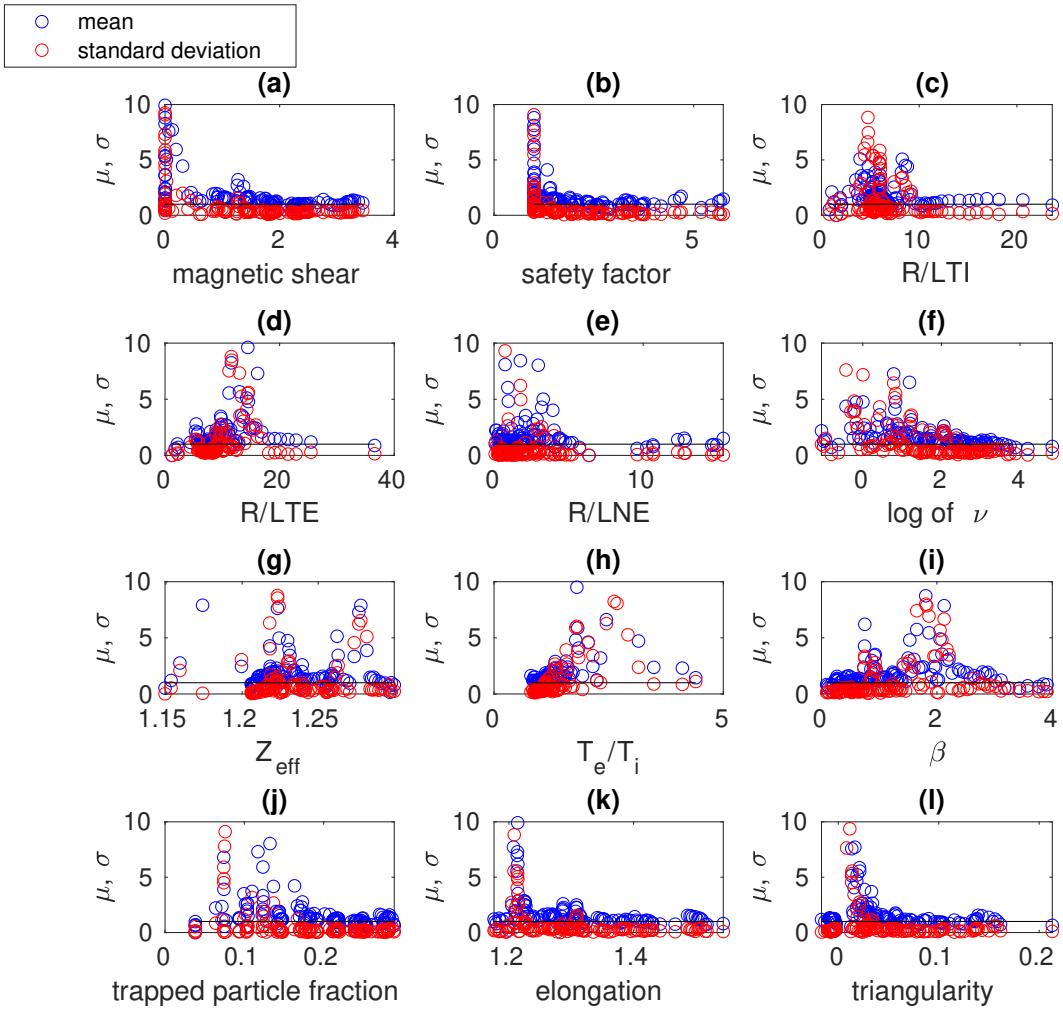

Figure 5.9: Mean and standard deviation of $\frac{\chi_{i,fitted}}{\chi_{i,TGLF}}$ depending on the different physical parameters included in the fitting

.

destabilizing and stabilizing effects, connected with the steep gradients (up to 1 order of magnitude steeper than in the core), the high safety factor, the collisionality, the plasma beta, the magnetic shear and the rotational shear, imply that the pedestal can host a variety of instabilities with consequent turbulence and transport properties. Therefore, a quantitative prediction of the transport in these conditions is not a trivial task, and it would need the usage of global gyrokinetic simulations. This is of course not feasible in a flight simulator, which must run an entire discharge in few minutes. Therefore, a simplified approach is chosen in Fenix, where the pedestal top is basically a boundary condition for the core model, even if the pedestal structure is not captured in detail. To distinguish the edge from the core another model has been used starting from $\rho_t = 0.9$, which is fixed as position of the top of pedestal, outwards. The pedestal width is then assumed. This assumption

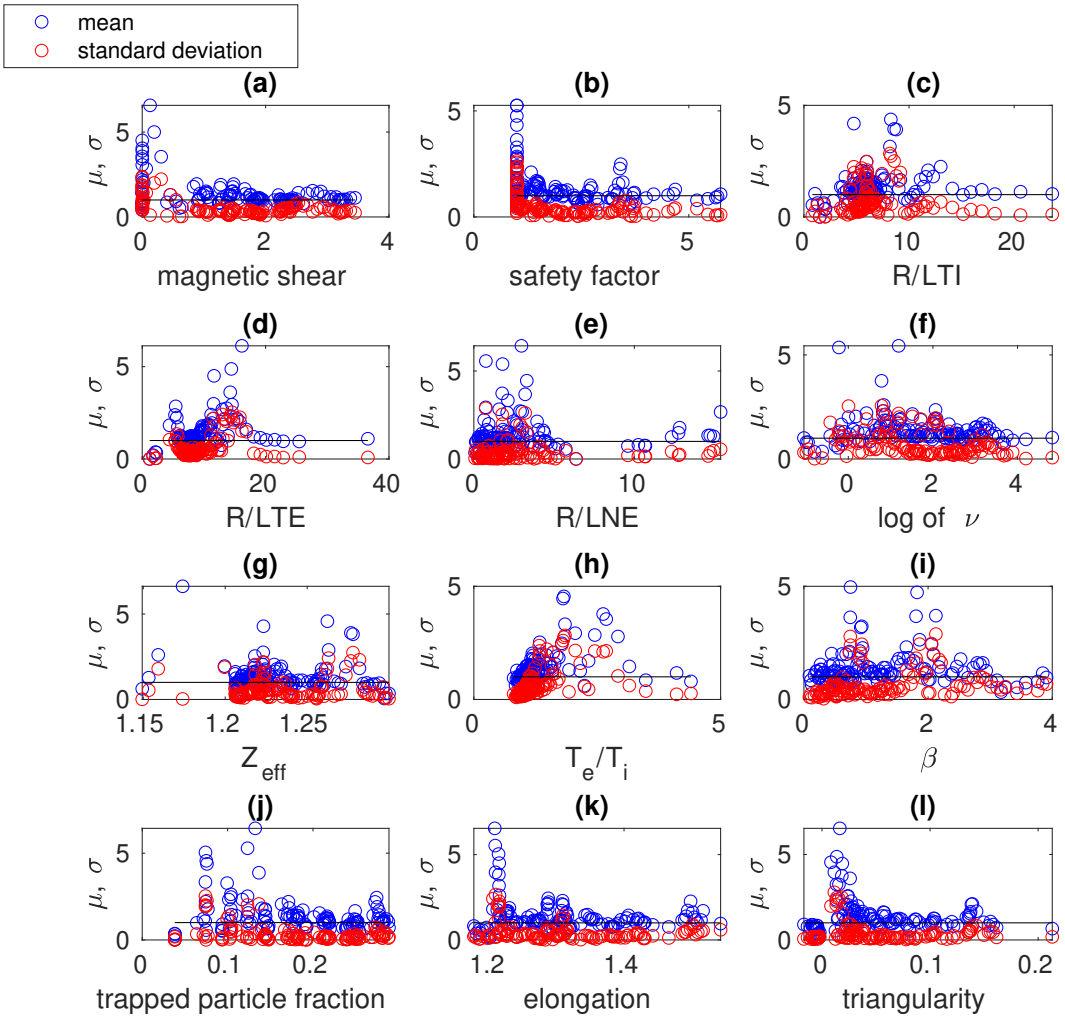

Figure 5.10: Mean and standard deviation of $\frac{\chi_{e,TEM+ITG,fitted}}{\chi_{e,TEM+ITG,TGLF}}$ depending on the different physical parameters included in the fitting

.

comes from the absence of a pedestal transport model, that coupled with an MHD stability model could calculate consistently the pedestal width. However, few pedestal transport models to estimate the pedestal width exist (e.g. EPED [48] and IMEP [47]), but they are computationally expensive, because they need to compute MHD stability. The choice of $\rho_t = 0.9$ as top of pedestal position has been made to connect smoothly core and edge models. Few tests have been done changing this position up to $\rho_t = 0.96$ and no big impact has been found on the results. This has proved that a specific assumption of the pedestal width inside this realistic range does not affect much the results when the pedestal top value is kept constant, justifying therefore the choice of a fixed pedestal width.

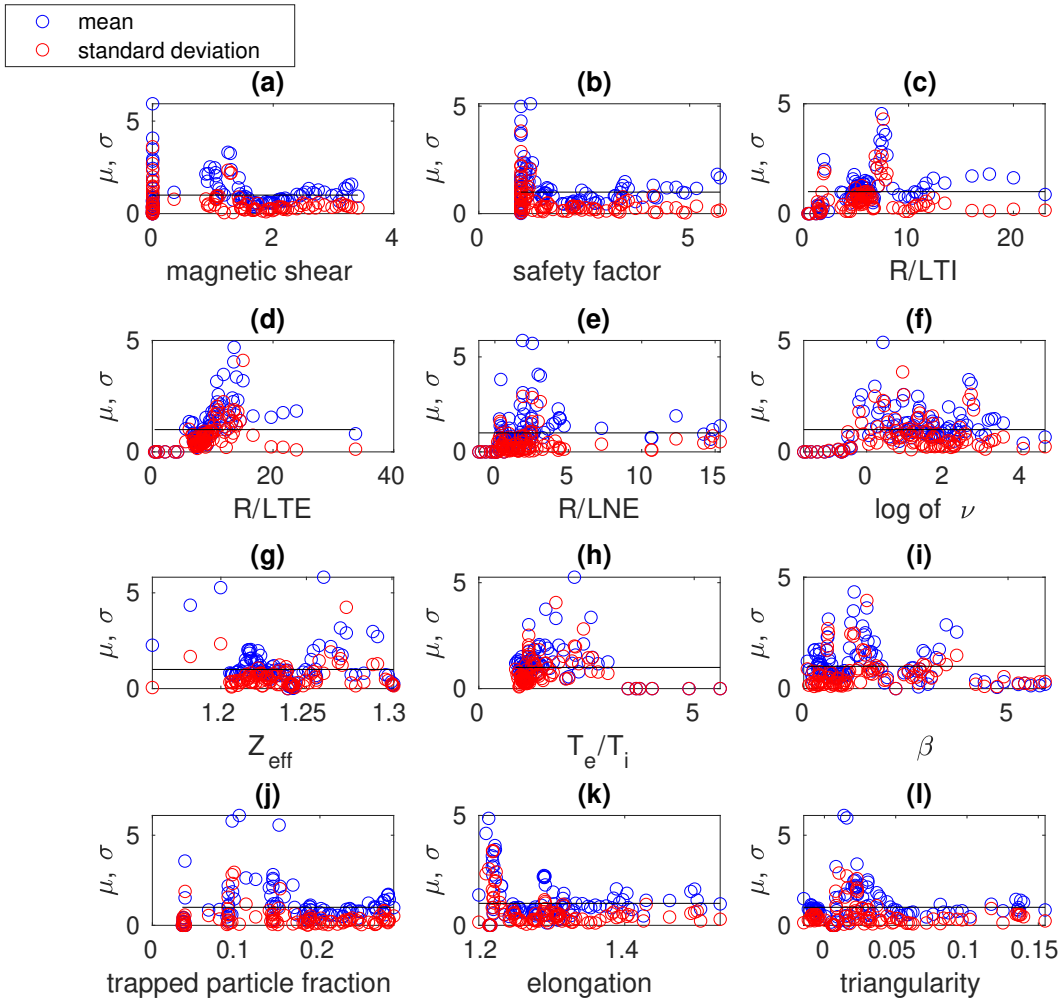

Figure 5.11: Mean and standard deviation of $\frac{\chi_{e,ETG,fitted}}{\chi_{e,ETG,TGLF}}$ depending on the different physical parameters included in the fitting.

5.2.1 Pedestal saturation model

It is known that in high confinement mode (H-mode) the dynamic is usually mainly dominated by Edge Localized Modes (ELMs) [113], [114], which are MHD instabilities, while micro-instabilities are often reduced by sheared flows (as ExB shear) [24]. The prediction of the ELMs frequency and intensity is a complicated task which needs nonlinear MHD calculations. Moreover the time-scales of such instabilities are much shorter than the macroscopic time-scales of interest ($> 1 - 10ms$), like the actuator response delay. This has justified the choice of an ELMs average model instead of a discrete ELMs model. While the latter describes the real physical temporal evolution of these instabilities with the succession of drops and growths of the pressure pedestal, the former considers a temporal average of such evolution to match the amount of total transport. This means that such model describes the plasma as constrained at the marginal stability, instead of os-

cillating around it through drops and growths. This allows us to neglect the transport inter-ELMs, which is the transport between consecutive ELMs, simplifying thus the description. Therefore, to simulate the ELMy H-mode configuration, an ELM average model has been adopted and the diffusivities have been assumed such that the profiles lay on the marginal stability limit of MHD Peeling-Ballooning model [115], [116]. This approach is justified by the fact that we are not interested in reproducing accurately the temporal evolution of the instability. However, a discrete ELMs model could be added in future.
To assume that the plasma lays on the marginal stability we have first to implement a critical value of a pressure-related parameter, which represents the threshold between stability and instability. In this thesis a $\beta_{p,MHD}$ threshold from literature [117] has been chosen. Then a heuristic formula for χ_e has been derived to keep the $\beta_{p,top}$, which is the value at the top of pedestal, close to $\beta_{p,MHD}$, which is the critical value for the onset of the instability:

$$\chi_e = \left(\frac{\beta_{p,top}}{\beta_{p,MHD}} \right)^4. \tag{5.16}$$

The critical value of $\beta_{p,MHD}$ is given by

$$\beta_{p,MHD} = 0.686\sqrt{k}(1+\delta)^{1.68} q^{1.61} \overline{\beta_p}^{0.33} \hat{n}_e^{0.06} w_p^{1.29}. \tag{5.17}$$

This is a scaling that has been obtained from an IPED [118] database in a previous work [117]. Here $\hat{n}_e$ is the electron density normalized to the Greenwald limit, while w_p is the pedestal width in the normalized poloidal flux label, which has been fixed to 0.1. This is a good assumption for AUG, but it needs to be generalized in order to extrapolate to other devices. In this scaling also the effect of the shape is included, which allows us to take into account and predict also the purely peeling or peeling-ballooning limited cases. In fact, through the shaping the stability diagram of the plasma (i.e. ∇p vs $j_\parallel$) can be modified, widening the ballooning stable operational space.
For the pedestal $\chi_i = \chi_e + \chi_{i,nc}$ has been assumed, supported by [47]. The particle diffusivity has been fixed to be equal to $C \cdot \chi_e$, where C has been fixed to 0.03 to match experimental stationary profiles in a selected discharge. This is still in agreement with [47].
In the low confinement regime (or L-mode, i.e. when the power threshold is not overcome), the fitting model used for the core has simply been extended to this region, while particle diffusivity was kept equal to $F \cdot \chi_e$, where F is calibrated to match experiments of the database ($F = 0.1$).
In order to predict the transition between L- and H-mode a criterion based on the ion power crossing the separatrix has been chosen, according to [56]:

$$Q_{i,LH} = 0.0029 \overline{n}_e^{1.05} B_T^{0.68} S^{0.93}. \tag{5.18}$$

Here S is the plasma lateral surface area in m^2. Differences in pedestal widths between density and temperature [119], [120] have been neglected, because they have been considered to have a small impact on the confinement and global parameter evolution.
The simulation of ELM-free scenarios (e.g. I-mode, EDA H-mode or negative triangularity) can be more challenging, due to the complicated and wide physics involved in the

edge. These scenarios are really attractive for future reactors, therefore at least a reduced prediction capability should be included. Hence for these configurations few ad-hoc models are present, which have less physics-based nature, due to the fact that the dynamic involved is still not fully understood. For the negative triangularity discharges a correction on the L-H transition has been numerically introduced to modify the power threshold. For the transition from L- to I-mode a scaling derived in [121] has been used, during which a pedestal arises only for the temperatures. For the stability of the I-mode pedestal the same model of H-mode is employed, but taking $\frac{\beta_{p,crit}}{2}$ as MHD threshold and no density pedestal.

5.3 SOL Particle Balance model

The models described for the confined region require boundary conditions at the LCFS to close the system. Therefore, we need to calculate the temperature and density at the separatrix. The former can be computed with the 2-point model from the literature [63], while to calculate the latter a SOL particle transport model has been derived in this thesis. As opposed to the core transport, which was based fully on a first-principles-derived model like TGLF, for the SOL we have to employ empirical arguments and fit the model free parameters against experimental measurements (e.g. particle density evolution). Moreover, as the dynamics of the SOL is strongly influenced by the plasma facing components material and geometry, this renders the problem and the fitting of the free parameters machine-dependent.
The proper treatment of the particle transport can be pursued by usage of time consuming codes which include the treatment of neutral particles, as SOLPS-ITER [59], [60]. However, this is widely beyond the scope of this thesis, and the implementation of such time-consuming code in Fenix is not feasible. Nevertheless, a simplified approach can be used to translate engineering parameters in boundary conditions for the separatrix. Few formulae have been already used in past for AUG, for example in [65], where the density at the separatrix is related to the neutral pressure at the divertor. This, coupled with a scaling that connects the neutral pressure with the gas puff intensity, like in [47], allows one to predict the density at the separatrix knowing the engineering parameters (e.g. gas puff, NBI power and vacuum pump velocity). However these are often related to technological aspects of a specific experiment, so they miss a general validity. Moreover these formulae are not time dependent, therefore they can not be used in a flight simulator.
In this thesis an alternative model has been developed, based on a multispecies 0D time dependent particle balance, which takes into account only the main features related to different regions included in the SOL, but ignores any detailed local dynamic. This model simulates the SOL by splitting it in 6 different zones which communicate with each other. These zones are the two divertor legs, the private flux region (PFR), the two upper sides of the Tokamak cross section, and an additional zone close to the wall on the low field side (LFS). The topology of the SOL with its regions is shown in figure 5.12. This configuration describes the lower single null (LSN) case, which is when the magnetic X-point is

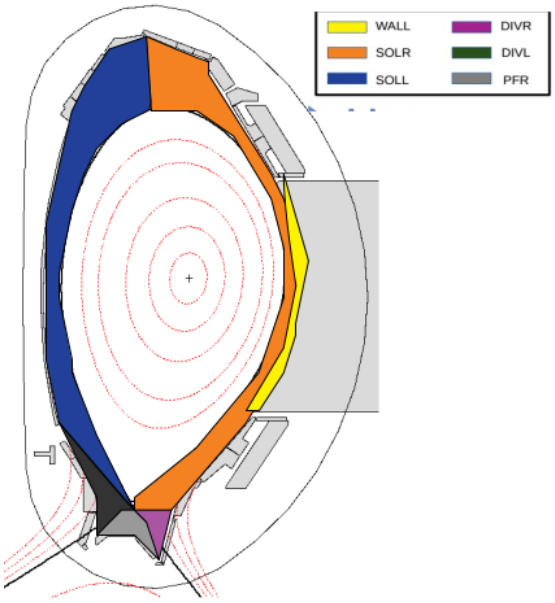

Figure 5.12: Splitting of the SOL region in 6 different zones.

positioned at the bottom of the plasma cross section. However, to simulate other divertor configurations the SOL can be splitted in more or different regions with different poloidal locations. For example, to simulate an upper single null (USN), which is a configuration where the divertor is at the top of the plasma cross section, the divertor and the private flux regions can be shifted upwards. Otherwise, to simulate a double null divertor (DN), which has 2 X-points, one can include another upper private flux region.
Every region is characterized by its topology and connection to the PFCs. This is taken into account empirically by setting free parameters as to replicate the main physics and phenomenology of each region. The model consists of a particle balance between all the confining regions, which includes diffusive terms, ionization sources, recombination sinks and sources of plasma coming from the LCFS. The recombination sinks have been assumed equal to zero, that is consistent with the assumption of attached divertor. Gas puff and vacuum pump are also included as source and sink in the regions where they act. These are examples of the possibility to treat local effects in the respective zones. One other example is the recycling factor, which is only modeled in the wall zone (i.e. low recycling regime). This is not always realistic, because in certain conditions (e.g. high recycling regime) the recycling from the divertor is the dominant one. Nevertheless, a more precise description of it including the recycling in both the divertor legs is planned for the future. The wall recycling factor is assumed equal to 0.99 for D and H. To simulate the wall leakage a diffusivity within the wall has been assumed, while for all the other zones perfect reflectivity of the PFCs has been considered. A special set of coefficients have been added in the equations to keep the concentration gradients between confining regions unbalanced, in order to mimic convection. In fact, different compression factors between different regions of the SOL are observed, showing that some zones have higher species concentrations

than others. The coefficients which keep the concentration gradients unbalanced are called enrichment factors and they multiply the density of the species:

$$\frac{dN_k^i}{dt} = S_k^i + P_k^i + \sum_{j=1, j\neq k}^{6} D_{jk}^i \left(\epsilon_{jk}^i \frac{N_j^i}{V_j} - \frac{N_k^i}{V_k} \right) \tag{5.19}$$

In this equation the index i refers to a specific species, S_k^i represents the source term in $\frac{particles}{s}$, which contains also the plasma coming from the confined region through the separatrix, P_k^i is the sink in $\frac{particles}{s}$, D_{jk}^i is a 0-D diffusion coefficient defined as an exchange rate between the regions j and k in m^3/s, N_k^i is the number of particles, V_k^i is the volume in m^3 and ϵ_{jk}^i is the enrichment factor (adimensional). From these balance equations the temporal evolution of the particle density in every region can be calculated as $\frac{N_k^i}{V_k^i}$. Since ASTRA adopts flux-surface-averaged equations, it means that we must take an average of the density of the different zones of the model facing the confined region as boundary condition at the separatrix. Such average is calculated between the densities of the 2 upper parts of the SOL (SOLL and SOLR in figure 5.12), because they are the only one above the X-point, which therefore face the confined plasma. In order to calculate the temporal evolution of the impurities in the SOL the model includes a multispecies treatment up to 8 species, all obeying equations as in 5.19. The treatment of neutral particles is crucial if one wants to include other possible configurations (e.g. detachment). This model allows in principle the inclusion of such treatment by adopting similar equations as in 5.19, but considering the recombinations as sources and the ionizations as sinks. However, this has not been tested in this thesis, thus it remains a possible future work. Considering 6 equations like (5.19) for 6 regions, the following system can be derived for each species:

$$\overline{N}^i = \overline{N}_0^i + \overline{\overline{D}}^i \cdot \overline{N}^i, \tag{5.20}$$

where $\overline{N}^i$ is the vector of the particles number for every region, $\overline{N}_0^i$ is the vector which includes all the local effects (ionization, recombination, recycling, vacuum pump or gas puff) and $\overline{\overline{D}}^i$ is the matrix of the diffusivities normalized by terms which include also the enrichment factors. The system is calculated implicitly. In particular $\overline{N}_0^i$ is

$$\overline{N}_0^i = \begin{pmatrix} \frac{N_{10}+\alpha_1\Gamma_1\delta t}{D_{N1}} \\ \frac{N_{20}+\left[(1-\alpha_1)\alpha_2\Gamma_1+(1-\alpha_6)\alpha_2\Gamma_6+\frac{\phi}{2}\right]\delta t}{D_{N2}} \\ \frac{N_{30}+\frac{\phi}{2}\delta t}{D_{N3}} \\ \frac{N_{40}}{D_{N4}} \\ \frac{N_{50}}{D_{N5}} \\ \frac{N_{60}+\alpha_6\Gamma_6\delta t}{D_{N6}} \end{pmatrix}, \tag{5.21}$$

and $\overline{\overline{D}}^i$ is

$$\overline{\overline{D}}^i = \begin{pmatrix} 0 & \frac{\epsilon_{12}\frac{D_{12}}{V_2}}{D_{N1}} & 0 & 0 & 0 & \frac{\epsilon_{16}\frac{D_{16}}{V_6}}{D_{N1}} \\ \frac{\frac{D_{12}+r_1(1-\alpha_1)\alpha_2 D_{10}}{V_1}}{D_{N2}} & 0 & \frac{\epsilon_{23}\frac{D_{23}}{V_3}}{D_{N2}} & 0 & 0 & \frac{\epsilon_{26}\frac{D_{26}}{V_6}}{D_{N2}} \\ 0 & \frac{\frac{D_{23}}{V_2}}{D_{N3}} & 0 & \frac{\epsilon_{34}\frac{D_{34}}{V_4}}{D_{N3}} & 0 & 0 \\ 0 & 0 & \frac{\frac{D_{34}}{V_3}}{D_{N4}} & 0 & \frac{\epsilon_{45}\frac{D_{45}}{V_5}}{D_{N4}} & 0 \\ 0 & 0 & 0 & \frac{\frac{D_{45}}{V_4}}{D_{N5}} & 0 & \frac{\epsilon_{56}\frac{D_{56}}{V_6}}{D_{N5}} \\ \frac{\frac{D_{16}}{V_1}}{D_{N6}} & \frac{\frac{D_{26}}{V_2}}{D_{N6}} & 0 & 0 & \frac{\frac{D_{56}}{V_5}}{D_{N6}} & 0 \end{pmatrix} \delta t, \tag{5.22}$$

where

$$D_{N1} = 1 + \frac{D_{10} + D_{12} + D_{16} - r_1\alpha_1 D_{10}}{V_1}\delta t, \tag{5.23}$$

$$D_{N2} = 1 + \frac{\epsilon_{12}D_{12} + D_{23} + D_{26}}{V_2}\delta t, \tag{5.24}$$

$$D_{N3} = 1 + \frac{\epsilon_{23}D_{23} + D_{34}}{V_3}\delta t, \tag{5.25}$$

$$D_{N4} = 1 + \frac{\epsilon_{34}D_{34} + D_{45}}{V_4}\delta t, \tag{5.26}$$

$$D_{N5} = 1 + \frac{\epsilon_{45}D_{45} + D_{56}}{V_5}\delta t, \tag{5.27}$$

$$D_{N6} = 1 + \frac{Q_{vac} + \epsilon_{16}D_{16} + \epsilon_{26}D_{26} + \epsilon_{56}D_{56}}{V_6}\delta t. \tag{5.28}$$

In the previous equations α is the ionization factor (adimensional), δt is the time step in s (necessary because D_{jk} is in $m^3 s^{-1}$ and D_{Nj} is adimensional), Γ is the gas puff in $\frac{particles}{s}$, ϕ is the plasma flux from the confined region in $\frac{particles}{s}$, r is the recycling factor (adimensional) and Q_{vac} is the pump volumetric flow in $m^3 s^{-1}$. It is easy to visualize the local effects in the SOL, which are for example the vacuum pump in the outer divertor (i.e. Q_{vac} in D_{N6}), the recycling factor for the wall (i.e. r_1 in D_{N1}), the gas puff in the outer upper SOL and the outer divertor (i.e. Γ_1 and Γ_6 in $(\overline{N}_0^i)_1$ and $(\overline{N}_0^i)_6$) and the flux from the confined plasma upon the X-point (i.e. ϕ in $(\overline{N}_0^i)_2$ and $(\overline{N}_0^i)_3$).
A crucial problem is the determination of the diffusivities between confining zones (i.e. D_{ij}). These have been derived heuristically, considering the main contributions to the

parallel and perpendicular particle transport:

$$\begin{aligned} D_{\parallel} = 0.1\frac{M}{L_{par,sep}} \quad \left(\frac{m^4}{s}\right), \qquad D_{\perp} = \frac{0.05\nu_{sep}}{(R_w - R_{omp})^2} \quad \left(\frac{m^5}{s}\right), \\ D_{23} = D_{34} = D_{26} = 1000 D_{\parallel}, \\ D_{10} = 0.03 D_{\perp}, \qquad D_{12} = 0.5 D_{\perp} \\ D_{45} = D_{56} = 0.1 \quad \left(\frac{m^3}{s}\right), \quad D_{16} = 0 \quad \left(\frac{m^3}{s}\right). \end{aligned} \tag{5.29}$$

Here *sep* subscript stands for separatrix, M is the sound velocity, calculated as $\sqrt{\frac{T_{i,sep}}{m_D}}$, m_D is the deuterium density, $L_{par,sep}$ is an estimate of the distance traveled by the particles along the field lines and it is calculated as $\pi q_{sep} R$, R_w and R_{omp} are the major radius at wall and outer midplane positions. D_{23}, D_{34} and D_{26} were calculated assuming convection as the dominating parallel transport. D_{45} and D_{56} were fixed to 0.1 to mimic a lower transport between the divertor legs across the private flux region with respect to the parallel transport along the field lines, which is a reasonable assumption for ions [122] in L-mode. The high gradients between divertor legs and private flux region assure anyway a higher value of diffusion across the private flux region in H-mode [122]. D_{16} has been fixed to 0 to neglect the transport from the wall directly to the divertor (i.e. perpendicular transport is the only dynamic assumed in the thin layer of plasma near the wall). D_{10} and D_{12}, which represent the perpendicular transport in the LFS, have been assumed proportional to the collisionality, according to [49], neglecting poloidal asymmetries. In particular D_{12} has been multiplied by 0.5 which is the standard value used in SOLPS calculations [52],[53], while D_{10} has been multiplied by 0.03 to take into account a certain level of D wall retention, which counteracts the outwards diffusion. The previous equations contain few numerical factors which represent the calibration of the model to match an experimental case.
To account for more complex local transport physics, such as the drifts, we introduced the enrichment factors ϵ, which keep the densities of the confining regions unbalanced and assure a certain background level of diffusion. These are

$$\begin{aligned} \epsilon_{12} = \epsilon_{23} = \epsilon_{45} = \epsilon_{16} = \epsilon_{56} = 1, \qquad \epsilon_{34} = 10, \\ \epsilon_{26} = 5 \cdot max\left\{1, min\left\{20, 0.2 {n_{D,H}}^{0.67}\right\}\right\}, \end{aligned} \tag{5.30}$$

in favourable configuration (i.e. $B_t I_p > 0$), while in unfavourable configuration $\epsilon_{23} = \frac{10}{R^2(1+2rR^{-1}))}$. This last coefficient has been used to model a $\nabla B \times B$ drift correction, which has been assumed inversely proportional to the size of the machine and includes an aspect ratio dependence. ϵ_{34} has been fixed to 10 to modulate a certain background level of high field side high density front (HFSHD) [52],[54],[123]. ϵ_{26} is a derivation of the steady-state formula of [65], which has also been successfully implemented in IMEP [47], for a time-dependent situation. $n_{D,H}$ is the density of D or H at the divertor. The numerical factors have been calibrated to match the separatrix electron density of an H-mode AUG discharge in the flight simulator. A better formulation of the enrichment factors including

detachment, X-point radiator [4], $\nabla B \times B$ and $E \times B$ drifts is planned for the future, so that a broader range of configurations and operational states can be simulated. All the particle diffusivities and enrichment factors shown here are used for D or H, but similar formulae are applied also for impurities, taking into account other additional aspects, like W sputtering, B coming from the boronization of the machine and N seeding. In particular the W sputtering is roughly modeled by adding a simple constant input of this species in the SOL. A similar approach is used for the residual B coming from the boronization.
The temporal evolution of D ions in a Fenix simulation of the H-mode discharge #40446 is shown in figure 5.13 together with the D gas puff. In this figure one can notice that the

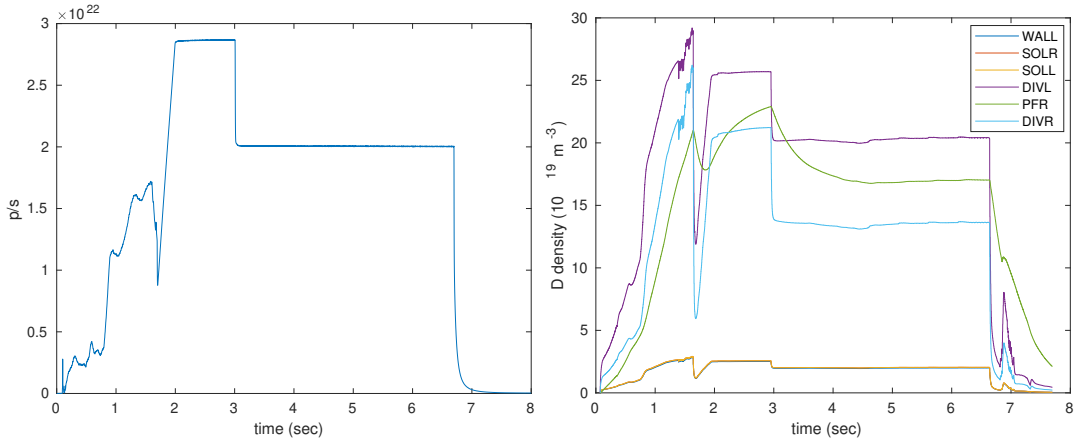

Figure 5.13: Left: D divertor gas puff evolution for discharge #40446. Right: temporal evolution of number of D ions in the SOL for the discharge #40446. For different colors are the densities in the different regions shown in figure 5.12.

densities above the X-point are one order of magnitude lower than the regions below. This is consistent with many experimental observations and theoretical predictions, especially if the particle source is coming from the divertor region (e.g. by gas puff and ionization). One can also notice that in the private flux region the density is lower than those of the divertors for $t < 2s$, while it lays between inner and outer divertor values for $t > 2s$. These 2 temporal ranges are before and after the onset of H-mode, and it is consistent with observations from [122]. It is worth to mention that the only parameters which depend on the temperature are the ionization coefficients of H, D and He.
The main limit of the model is the presence of a specific divertor configuration, which is the LSN. As already mentioned, other configurations (e.g. USN and DN) can still be included by splitting the SOL in more zones, while maintaining a similar approach in describing the particle content in each zone. The modeling of the X-point radiator and detachment are still not included, but they could be implemented by adding the treatment of neutrals in the particle balance and modifying the enrichment factors, without changing the background structure. The description of transport and heat or particle loads with consequent erosion deriving from ELMs is still not provided. However, the W influx should be independent on the conditions of the divertor, even in presence of ELMs, because the region which

dominates such quantity in AUG is the main chamber [124]. Therefore, the same model with the same tuning coefficients is used for both L- and H-mode.

Chapter 6

Results of Fenix with the new Integrated Model

Employing the integrated transport model described in the previous chapter, a series of discharges have been modeled with Fenix to both test and validate the proposed reduced models against pre-existing plasmas. These pulses are listed in the table 6.1, together with their main quantities. One can see that the heating power and average density are different for the 6 discharges covering respectively ranges of $2.5 - 10MW$ and $4.6 - 9.35 \cdot 10^{19} m^{-3}$.

Discharge	Scenario	I_P $[MA]$	B_T $[T]$	P_{aux} $[MW]$	$\overline{n}_e$ $10^{19}[m^{-3}]$	q_{95}
#40446	H-mode	1.019	2.53	10.162	7.9	4.397
#38898	L-mode	0.799	2.99	2.549	4.57	5.86
#40009	H-mode	1.024	2.503	8.523	6.4	4.420
#40254	H-mode	1.017	2.501	7.507	9.35	4.408
#39977	H-mode	0.993	2.502	6.141	6.23	4.463
#39967	H-mode	1.017	2.504	7.667	8.5	4.412

Table 6.1: Discharges analyzed with Fenix, together with their main global quantities.

6.1 Standard H-mode validation

The first discharge analyzed (#40446) is a standard H-mode, which is a reference discharge already described in the chapter of AUG.
Figures 6.1 to 6.6 show the trajectories of several engineering parameters and actuators of the discharge #40446. For this pulse a feedback on the average density, the position and the shape is used, while the heating systems are steered in feed-forward mode. In figure 6.1 gyr1, gyr2, gyr3 and gyr4 panels show the ECRH gyrotrons time traces, while ICRH pair 1 and 2 show the 2 couples of 4 ICRH sources. In figure 6.2 one can see instead the time trace of the NBI sources. The shape of the plasma and its position are controlled by the magnetic coils. In figure 6.4 the time traces of such coil currents are shown, while the

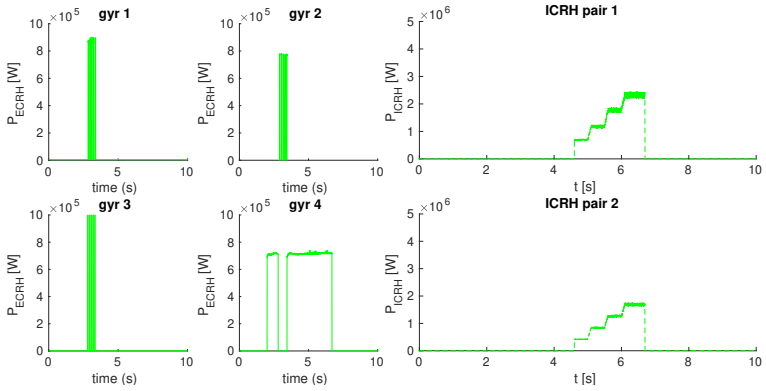

Figure 6.1: Time traces of ECRH and ICRH for the discharge #40446. On the left gyr1, gyr2, gyr3 and gyr4 represent the 4 not null time traces of ECRH gyrotrons, while on the right ICRH pair 1 and ICRH pair 2 represent ICRH time traces.

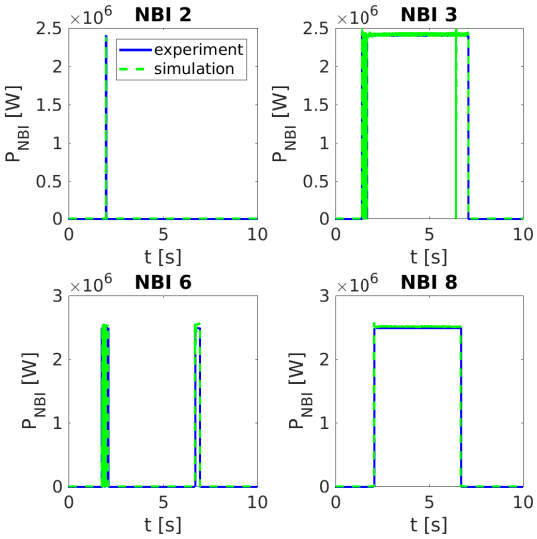

Figure 6.2: Time traces of the NBI power sources. The 4 different plots are for 4 different boxes. In blue is the experimental time trace, while in green is the simulated one.

geometrical parameters which define the position of the plasma are shown in figure 6.5. In figure 6.3 the geometry of the magnetic coils with the associated nomenclature is shown, to help the reader to identify the coil currents in figure 6.4. Few vertical lines are shown in the plots of figure 6.4, to indicate the beginning or the end of a feedback phase. For the same time points, in figure 6.5, the feedback on the position of the plasma (and consequently of the shape) is respectively switched on and off. More details about the connection between the current coils, the position and the shape are given in the caption of the figures.

The feedback on the average density is shown in figure 6.6, where in the upper plot is the average density and in the lower plot is the divertor gas puff. One can see in the

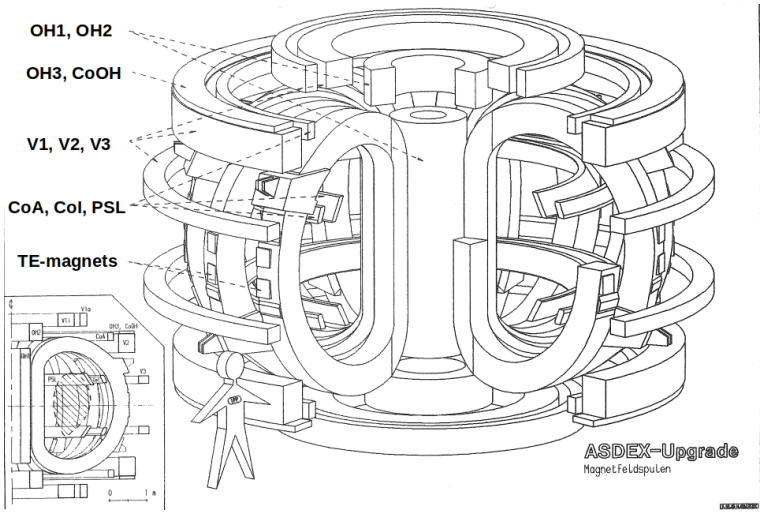

Figure 6.3: Geometry of the control magnetic coils of AUG

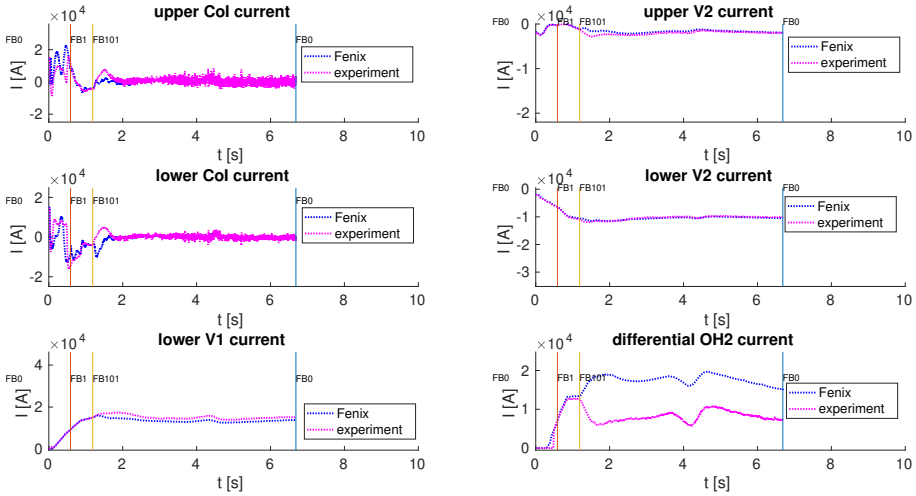

Figure 6.4: Time traces of the coil currents. The geometry of the coil currents is shown in figure 6.3. In particular OH2 is the one at the bottom of the tokamak, which is used to control the X-point formation. In all the plots in purple is the experimental time trace, while in blue is the one from the simulation. The vertical lines shown in the plots identify the beginning or the end of a feedback phase. One can see that different actuators act on different phases of the discharge: after the orange vertical line (i.e. during the ramp-up) all the coils are involved, while after the yellow vertical line (i.e. in the flattop and ramp-down phases) only CoI, V2 and OH2 control the shape and the position of the plasma. However, OH2 does not match the experimental time trace in the last phase because the edge current density is not well developed in the models.

upper plot a sensitive difference between the actual value of the density and its target value, which matches the experimental time trace, during the feedback phase. Here, one

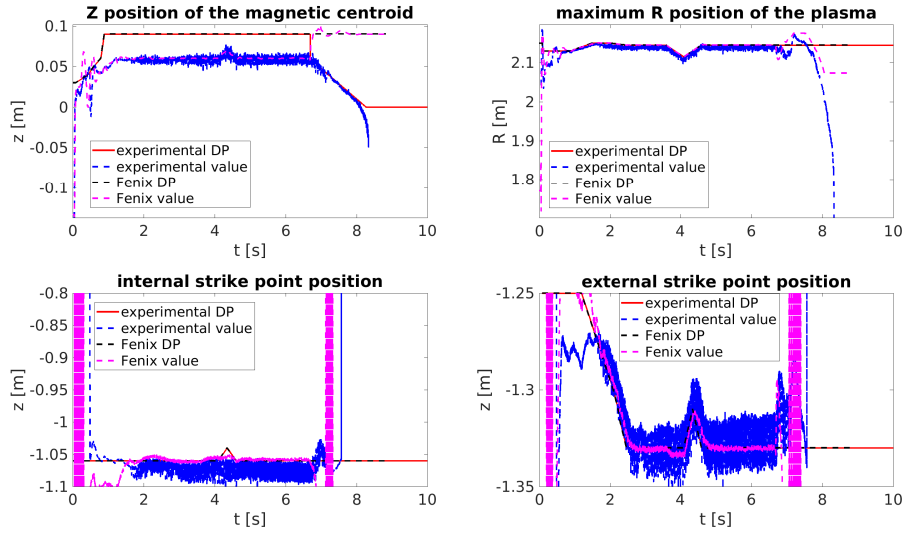

Figure 6.5: Time trace of the geometrical parameters of the plasma. These parameters are controlled by the coils currents shown in figure 6.4. In red is the time trace of the DP used during the experiment, in blue the measured time trace, in black the DP used in Fenix and in purple the simulated time trace. One can notice that for the maximum R position, the centroid Z position and the external strike point the time traces overlap from 2 to around 7 seconds, which is during the flattop, because a feedback is switched on.

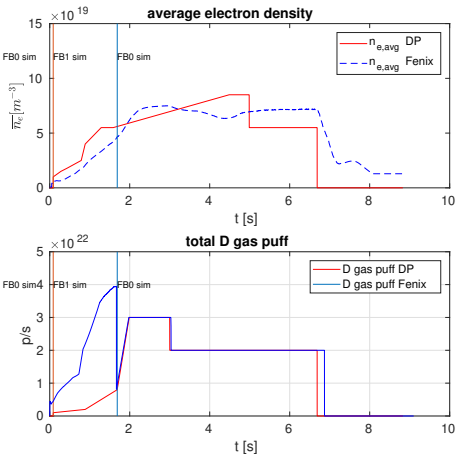

Figure 6.6: In the upper plot is the time trace of the electron density averaged along the entire radius, while in the lower plot is the time trace of the divertor gas puff, which is used to control the average density. In blue is the time trace from the simulation and in red the one from the DP. The orange vertical line represents the beginning of a feedback phase, while the blue one shows the end of it.

can notice that the inner core density does not grow on the right time scale, despite the

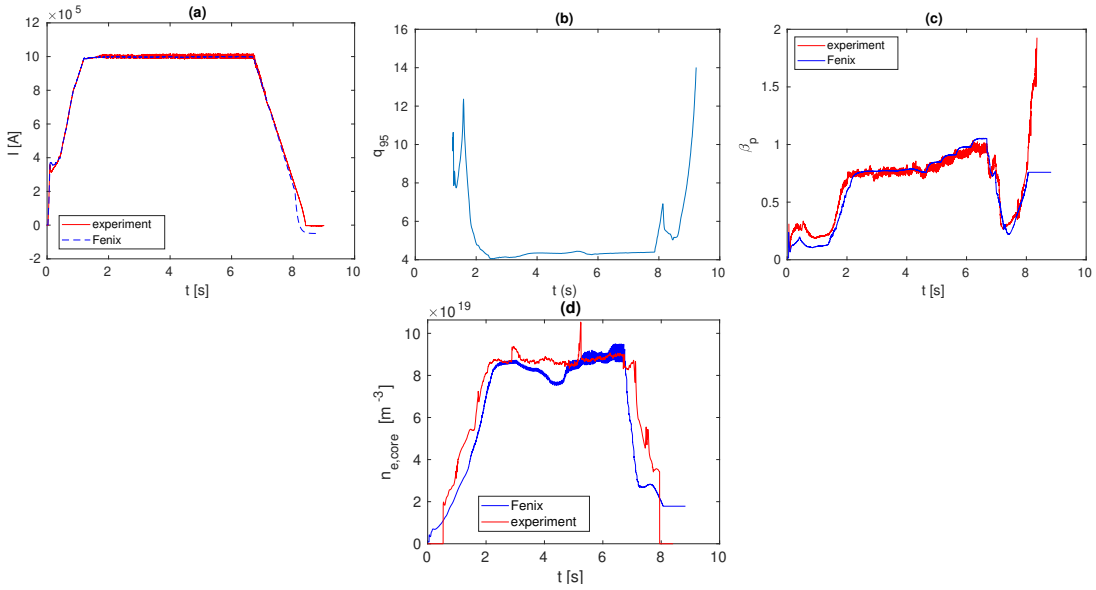

Figure 6.7: Time traces of the global parameters of a Fenix simulation of the discharge #40446. (a) shows the plasma current, (b) illustrates the simulated q_{95}, (c) is β_p and (d) is $n_{e,core}$ (calculated as average between $\rho_t = 0$ and $\rho_t = 0.3$).

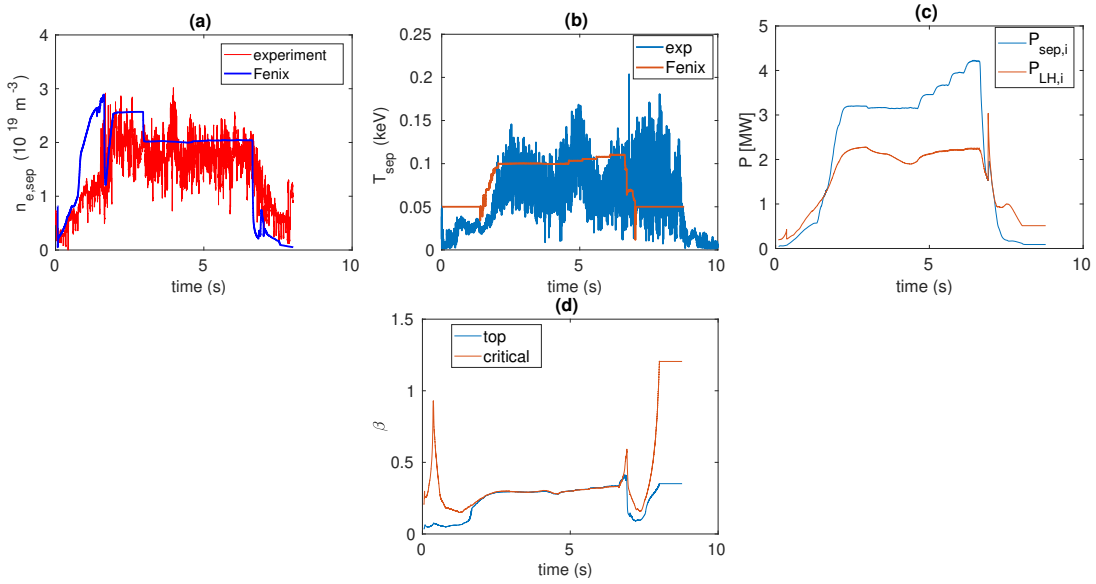

Figure 6.8: Time traces of the control parameters of the integrated model. In (a) the electron density at the separatrix is shown, in (b) the electron temperature at the separatrix is plotted, in (c) the simulated ion power at the separatrix with its L-H threshold are plotted, in (d) the simulated β_p at the top of pedestal with its critical value are shown.

strong gas puff shown in the lower plot. This is due to the inaccuracy of the particle

transport model, whose limitations are more evident during the ramp-up (i.e. in the feedback phase for this discharge). This will be discussed more in the following. Figure 6.7 shows the time trace of few global parameters, while in figure 6.8 the time traces related to the integrated model are shown. These are the electron density and temperature at

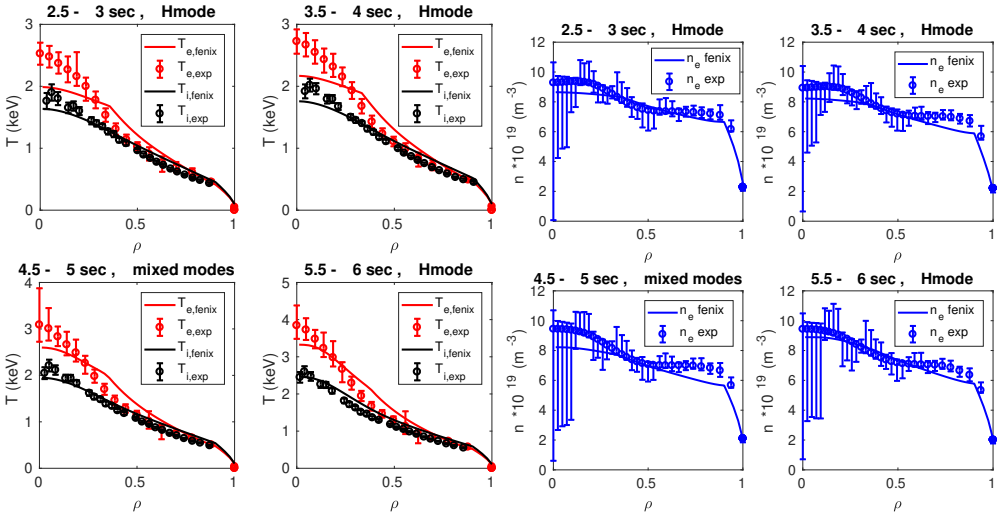

Figure 6.9: Kinetic profiles of a Fenix simulation of discharge #40446 for 4 time slots of the flattop. The 4 plots on the left show in red (black) the electron (ion) temperature, where the solid line is for the simulation and the markers with the error bars are for the experimental profile. The 4 plots on the right show the electron density in blue, where the solid line is for the simulation and the dots with the error bars are for the experimental profile.

the separatrix (respectively figure 6.8.a and 6.8.b), the ion power crossing the separatrix (figure 6.8.c) and the comparison between β_p at the top of pedestal and its critical value calculated with the scaling (figure 6.8.d), as in section 3. One can see that when the power at the separatrix exceeds the critical value (around 2s) $\beta_{p,top}$ approaches the critical value, showing that the H-mode model is triggered. In figure 6.7.c one can see that β_p follows the experimental trajectory for most of the duration of the discharge, so a first validation of the model is given. However, by looking at β_p, one can notice a mismatch with the experimental time trace in the early phase. This is due to the fact that during the ramp-up a TEM dominated regime at high collisionality is found [125], and our model is not able to reproduce it. Moreover, the core particle transport model underestimates the density in the ramp-up phase, because the inward diffusion and its time-scale are underpredicted. However, after the ramp-up the average and maximum error on β_p are respectively equal to 7% and 29%. More comments about these numbers will be made in the following.
Figure 6.9 shows the kinetic profiles during different phases of the discharge. The profiles from the simulation are not always within the experimental error bars, but for $\rho < 0.9$ the maximum error is 20% and for for $\rho > 0.9$ it is 7%. These errors show a limit of the transport model, which can therefore be improved, but we consider it a good starting

point, considering that the task of the flight simulator is not a detailed analysis of the physics, but the prediction of the evolution of the global parameters. In figure 6.10 the different contributions to χ_e via ETG, ITG and TEM channels are shown along the entire #40446 discharge. One can see that for this case ITG is the dominant mode, also during the ramp-up. This is due to the underprediction of the high collisionality TEM-dominated regime during the ramp-up of AUG pulses [125].

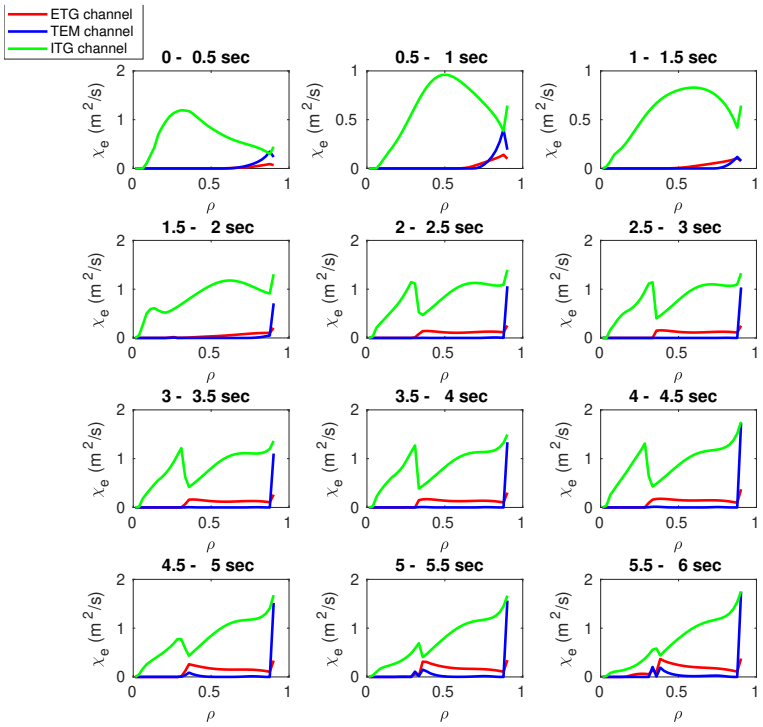

Figure 6.10: Contributions to the electron heat diffusivity from microturbulence during the entire discharge #40446. In red is the ETG contribution, in blue is the TEM part and in green is the contribution due to ITG channel. One can see that the dominant contribution to the transport is due to the ITG mode.

6.2 L-mode validation

The discharge #40446 is an H-mode where the transition takes place at the beginning of the flat-top, therefore one could argue that the mismatch in β_p found in the first 1.5 seconds is due to the fact that here the plasma is still in L-mode. In order to disprove this and disentangle the ramp-up from the L-mode, an Ohmic heated L-mode discharge (#38998) has also been run in Fenix. The time traces of this discharge are shown in figure 6.11, as for the previous pulse. Also here β_p follows the experimental trajectory, but the average and maximum errors are bigger than the ones of the previous discharge (respectively 15% and 55%). Figure 6.12 shows the kinetic profiles between 2.4 and 2.7 seconds. Here on the

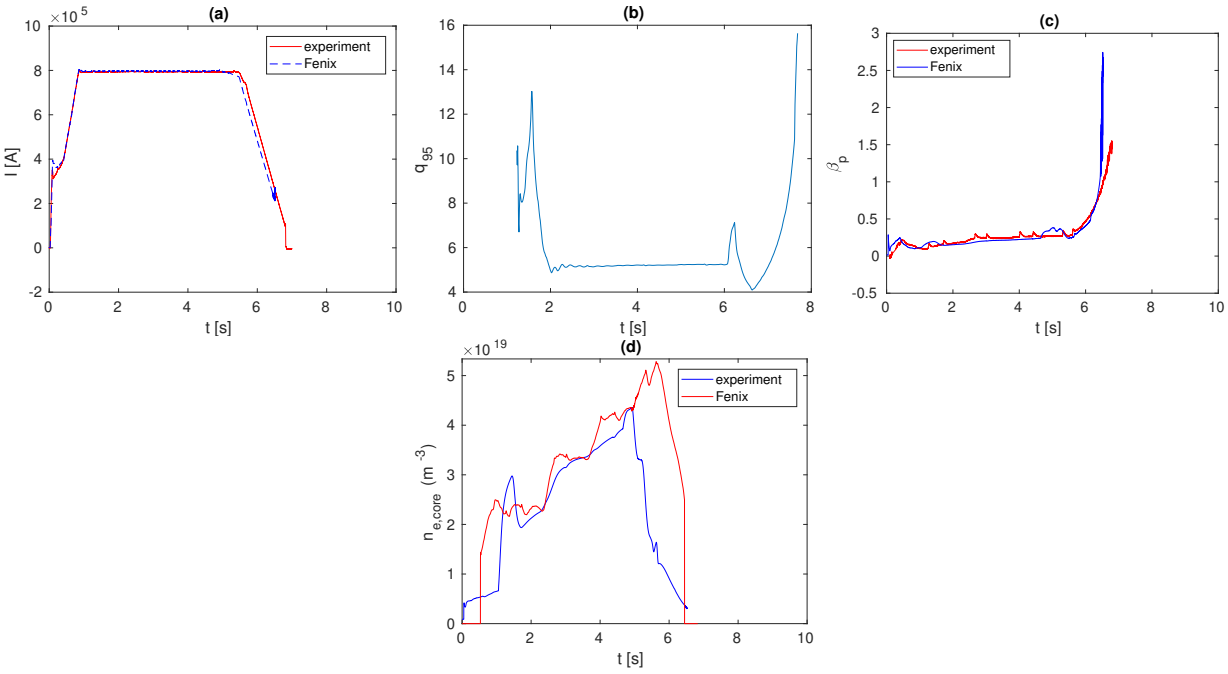

Figure 6.11: Time traces of the global parameters of a Fenix simulation of the discharge #38898. (a) shows the plasma current, (b) illustrates the simulated q_{95}, (c) is β_p and (d) is $n_{e,core}$ (calculated as average between $\rho_t = 0$ and $\rho_t = 0.3$).

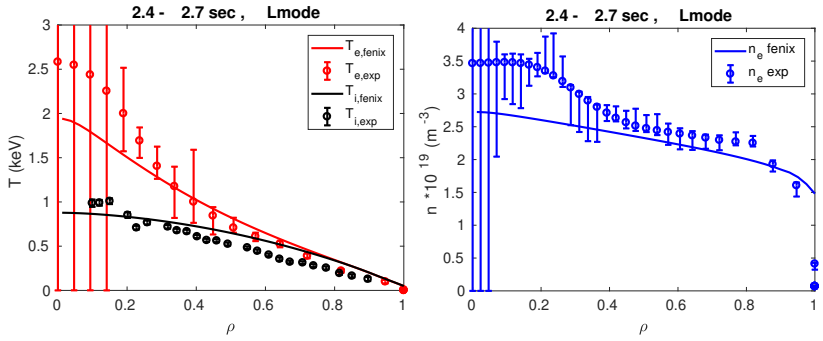

Figure 6.12: Kinetic profiles of the discharge #38898 between t=2.4 and t=2.7 seconds. On the left in red (black) is the electron (ion) temperature, while on the right in blue is the electron density. The solid line is the simulation while the dots are the experimental profiles with the error bars.

right the density profile from Fenix (solid line) shows a non-negligible mismatch with the experimental one (dots). The reasons for the bigger errors on the global parameters and profiles will be discussed at the end of the chapter.

6.3 Further validation

In order to strengthen the validation of the integrated transport model other 4 H-mode discharges characterised by different particle source, heating power and average density have been simulated. The trajectories of I_p and β_p for the various discharges are shown in figure 6.13. The average and maximum error on β_p are shown in table 6.2. While the

Discharge	average erf (%)	maximum erf (%)
#40009	2.3	39
#40254	17	66
#39977	9	44
#39967	7.8	37

Table 6.2: Average and maximum errors of the simulated β_p with respect to the experimental time trace, including flat-top and ramp-down for 4 H-mode discharges.

average errors are low, the maximum errors are high for these 4 discharges. The reason of it will be investigated in the next section. The time traces of the heating power and the D particle source for these discharges are compared respectively in figure 6.14.a and 6.14.b, while the time trace of the average density of the core (for $\rho < 0.3$) is shown in figure 6.15. In figure 6.14.b there is no gas puff signal for the discharge #39977, because there was no diagnostic data available. One can notice an underestimation of the average density in the inner core (for $\rho < 0.3$) in figure 6.15.a, 6.15.c and 6.15.d. However, the simulated time trace of the line averaged density (for $0 < \rho < 1$) reproduces the experimental measurement with higher accuracy, as can be seen in figure 6.16 for the discharges #39967 and #39977. The feedback on the line averaged density for the four discharges is switched off around 1.5s. This is the cause of the drop in the simulated time traces of figure 6.16.

All the results collected in this chapter suggest that the model can predict the temperature profiles and the global parameter evolution during the flat-top and the ramp-down of the discharge, despite the differences between the various transients [125], [126]. However, the mismatch of the density profile is often non-negligible, therefore an improvement is necessary to model the particle transport. The reasons related to the main mismatching profiles or time traces are discussed in detail in the next section.

6.4 Discussion on the observed discrepancies

Most of the time traces and profiles shown in the previous sections match the experimental measurements with a precision that reaches errors of $< 10\%$. However, a detailed analysis has revealed systematic mismatch in few parameters, which deserves a justification.
In the previous sections, the time traces of β_p have been shown for all the pulses with their maximum error with respect to the experimental measurements, whose value was found up to 66% for one discharge. However, the average error, which reaches at maximum 17% for one pulse, is on average 7.28%. Such difference between average and maximum error is due

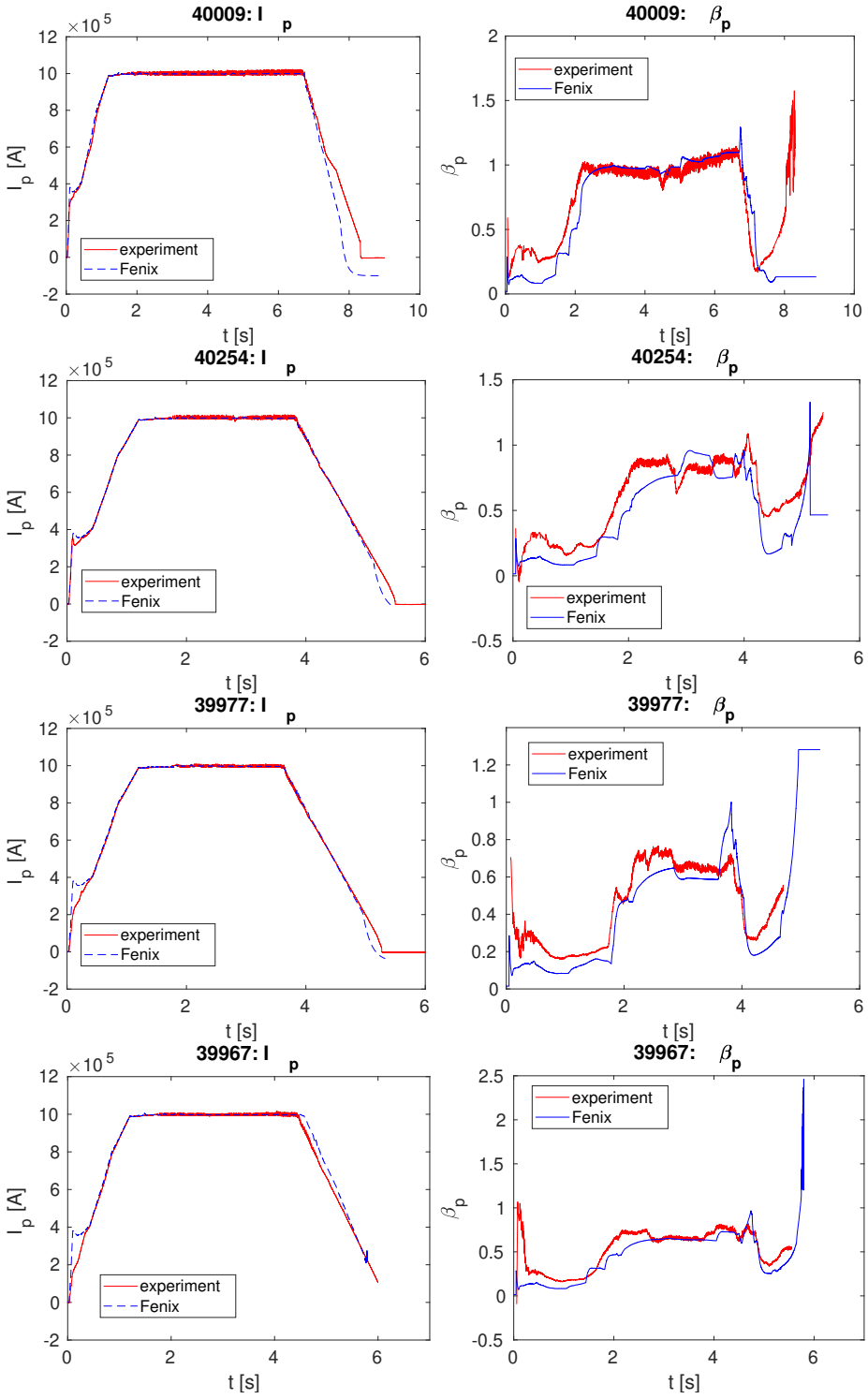

Figure 6.13: Time traces of I_p and β_p for 4 H-mode discharges (#40009, #40254, #39977 and #39967). In blue is Fenix and in red is the experimental measurement.

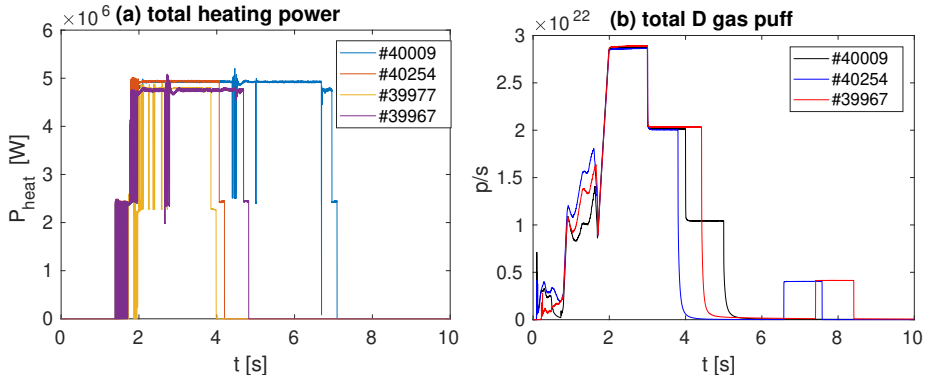

Figure 6.14: Time traces of the total heating power for 4 H-mode discharges are shown in (a), while the D gas puff is shown in (b). In (b) the experimental gas puff of the discharge #39977 is not shown because there was no diagnostic measurement available.

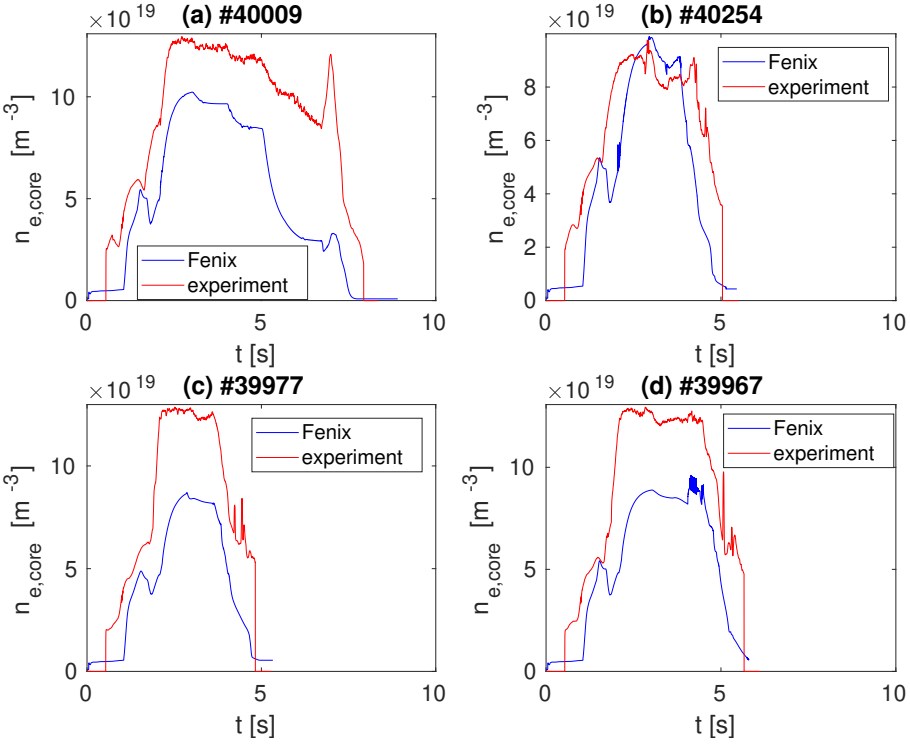

Figure 6.15: Time trace of the simulated (blue) and experimental (red) average density in the inner core (for $\rho < 0.3$) for the discharge #40009 in (a), #40254 in (b), #39977 in (c) and #39967 in (d). While for the pulse #40254 a good match is found, for the other 3 cases there is an underestimation of the density.

to fact that some phases of the discharges are reproduced with less precision. Such phases are the early phase of the flat-top, especially with strong gas puff, and the late phase of the ramp-down. In both the cases the mismatch is related to the delay between the gas

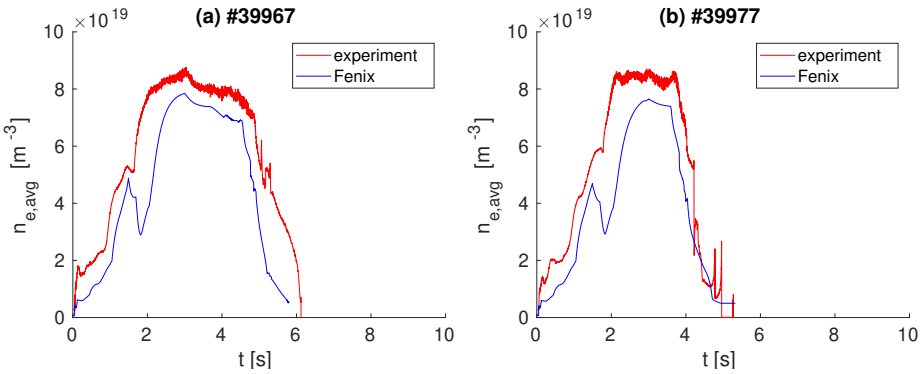

Figure 6.16: Comparison between the simulated (blue) and experimental (red) time trace of the line average density (for $0 < \rho < 1$) for the discharges #39967 (left) and #39977 (right).

puff insertion and the reaction of the density profile. The cause of this could be that the simulated inward convection or outwards diffusion is slower than in the experiment. This implies that the time trace of β_p is delayed with respect to the experiment, as can be seen on the right plots of figure 6.13. This mismatch is more pronounced for short pulses with strong gas puff, where the increase in density and its peaking factor, which is defined as the ratio between the density at the magnetic axis and the volume-averaged density, is stronger and more concentrated in time. The reason for the disagreement between the simulated and experimental time trace is the particle transport in the core, which is modeled with a heuristic formula of the pinch and a proportionality between D and χ_e. Such simplified model is not able to reproduce the different time-scales that the particle transport can have. In addiction to this, in the late phase of the ramp-down the low values of β_p allow for bigger relative errors.

In the results of the previous sections the kinetic profiles from 2 discharges have been shown. While for the temperature profiles an acceptable error is found, the density profile of the L-mode (#38998) shows a non-negligible mismatch with the experimental measurements. In fact, the right plot of figure 6.12 shows a clear underestimation of the the peaking factor and a mismatch in the edge. This is attributable again to the simplicity of the particle transport model. In particular, for a L-mode is even more difficult to predict the particle transport in the edge, because there is no pedestal model and simple proportionality between D and χ_e is assumed, with neoclassical pinch. Nevertheless, the experimental profile always shows a minimum pedestal, which is hard to reproduce.

Finally, an underestimation has been found in the time traces of the core averaged density, as can bee seen in figure 6.15. This is again related with the particle convection, which is not able to reproduce the density peaking factor dynamics. This underestimation is stronger for short discharges with strong gas puff, like the ones in figure 6.15.c and 6.15.d.

To conclude, most of the limits encountered in the validation process of the models developed in this thesis can be related to the inaccuracy of the particle transport model. In particular, the underestimation of the peaking factor and the particle transport time-scale

limits the predictive power. A correct prediction is observed only in the cases of long discharges, where the flat-top duration is maximized, or short discharges with reduced gas puff, where the increase in density is limited. During the flat-top the variations of the actuators and global parameters are usually slower or less extended in time than during the transient phases, leading to an easier capability of matching between simulation and experiment.

Chapter 7

Conclusions and Outlook

In this thesis, we have proposed and implemented improvements in several of the reduced physics models that populate the tokamak plasma flight simulator Fenix. We remember that Fenix has the goal of predicting an entire plasma discharge, from the coils premagnetization to the plasma termination after the current ramp-down. This will allow the experimental/operation leader to check the quality of the discharge program, eventual faults, if physics goals can be achieved, limits eventually touched and disruptive situations. For future devices, this pre-check will be vital for the machine safety. Concretely, Fenix couples a model for the control system with models which describe the physics of the plasma as well as sensors and actuators of the tokamak. The needs for simplified physics models, which must be run on an almost real-time scale, is due to the fact that Fenix should be used several times during the experimental day, inter-discharge, to rapidly predict the next pulse before its actual execution.

In this thesis, we have specifically worked on three transport models, which represent the main part of the plasma dynamics as simulated in Fenix. Such models have been developed in ASTRA. The core model has been developed to simulate the transport for $0 < \rho_t < 0.9$, the edge model is applied in the region $0.9 < \rho_t < 1$, while the SOL particle model is developed for the unconfined region. Having ASTRA a radial grid up to the LCFS, the SOL has been simulated virtually in a dedicated routine. These models give boundary conditions to each other.

The core model consists of a set of analytical transport coefficients, based on the main micro-instabilities which dominate the turbulent transport in the core (i.e. ITG, TEM, ETG). The formulae for the ion and electron heat diffusivities are fitted over a TGLF database made of 15 stationary phases of AUG discharges + 90 virtual discharges generated by changing by 10% the kinetic profiles (i.e. n_e, T_e, T_i) at the boundary conditions of the 15 AUG pulses. The boundary conditions of the simulations have been fixed experimentally at $\rho_t = 0.9$, as TGLF is not yet validated for the H-mode pedestal region. The discharges included in the database cover different scenarios (i.e. H-mode, L-mode, I-mode and other ELM-free scenarios) to strengthen the general validity of the model. The par-

ticle transport coefficient is represented by a diffusivity proportional to the electron heat diffusivity, and a convection coefficient calculated with a heuristic formula, which takes inspiration by the literature including the main parameters which affect the convection. The results of the fitting procedure show a non-negligible scattering of the analytical coefficients with respect to the values calculated by TGLF, especially for the ETG case, which was found to contribute to less than 5% of the transport.

For the edge, different models are employed depending on the configuration of the plasma. In case of an L-mode the core heat transport model is extended to this region and a proportionality between χ_e and D is assumed. The L-H transition has been modeled with a criterion based on the exceed of a threshold of the ion heat flux at the separatrix, according to the literature. To simulate the pedestal in the H-mode an ELM average model is used. In particular a heuristic coefficient is implemented in order to regulate the transport in such a way that β_p at the top of pedestal, whose position is fixed to $\rho_t = 0.9$, equals a critical value. This critical value has been taken from the literature, where it was obtained through a scaling on EPED simulations. The anomalous part of χ_i has been assumed equal to χ_e.

The SOL has been simulated with two different models to give the boundary conditions of the temperature and the density at the separatrix. These are respectively the 2-point model for the electron temperature, taken from the literature, and a particle transport model developed in this thesis. The latter is composed by a 0D particle balance between 6 confining regions in which the SOL has been virtually splitted to treat the local effects only in the zones where they take place. The diffusion between confining zones has been simulated with diffusion coefficients. The compression factors are accounted by including enrichment factors in the equations. Diffusivities and enrichment factors are derived heuristically. The SOL model includes also the treatment of impurity transport, using the same equations but different local effects and sources with respect to the main ions. The neutral particles are not included, therefore only attached conditions can be represented.

Employing all these models, a complete description of the plasma transport in the tokamak is provided. Therefore, the simulation of 1 L-mode (#38898) and 5 H-mode (#40446, #40009, #40254, #39977, #39967) discharges has been executed with the integrated model. The results have shown that β_p, $\overline{n}_e$ and other global parameters are matched with sufficient precision during the flat-top and ramp-down phase of the pulse. In particular, including all the analyzed pulses, an average error of 7.28% has been found for β_p after the ramp-up. This value is affected by the inclusion of the ramp-down where the β_p reaches low values, leading to higher values of relative error. The kinetic profiles have been shown for different phases of the discharges. The temperature profiles are predicted with less precision with respect to the global parameters, but a maximum error of 20% in the core and 7% in the edge have been found for the discharge #40446. The observed discrepancies between the simulated and the real discharge profiles are sufficiently low as to not impact substantially the global parameters of interest, thus allowing to consider the

simulated case a good virtual realization of the discharge. However, the prediction of the density profile has shown evident limits, related to the weak predictivity of the particle transport model developed in the thesis. In particular, the density profile often shows an underestimation of the peaking factor.

The results presented in this work have demonstrated the viability and potential capabilities of a physics-based flight simulator and the correct prediction of the global parameters and the temperature profiles. The models developed to reach such results are particularly attractive for two main aspects: they are analytical, so the computational time is extremely low, and they are written in a form as to minimize the need for experimental input, thus giving them the character of generalized models which can be applied to other machines and scenarios (via appropriate refit of the empirical parameters that are compromised in some of the models). However, the models do not need experimental input from a specific discharge in order to simulate it in Fenix.
Few clear limitations have arisen during the development and the validation of the models:

- the prediction of the density profile and its peaking factor is weak. This is important for reactor-relevant pulses, because in the inner core the highest value of density is reached, leading to the highest rate of nuclear fusion reactions;

- the prediction of the ETG transport needs improvements. In fact, the small contribution to the transport played by ETG in the TGLF simulations reduces the reliability of the database used to fit the ETG transport coefficient;

- cross-dependencies and non-monotonic dependencies on the parameters should be included in the core transport formulae to describe the physics more in detail, especially when the normalized gradients are close to their thresholds (e.g. the exponent of the power law which represents the stiffness could depend on other parameters);

- the assumption of local transport implies that the extrapolation to other devices can not always be guaranteed. However, this approximation should still be valid for future bigger machines and reactors;

- in the edge model the pedestal width is fixed. This hypothesis is based on the necessity of fast simulations, but it represents a strong approximation. Nevertheless, many of the existing codes which calculate the pedestal transport make heuristic assumptions, similar to the one we have done. A sensitivity study on the pedestal width has been done, by changing its position up to $\rho_t = 0.96$ and the impact on the evolution of the global parameters has been found small. The two last arguments have supported the decision of assigning the pedestal width, without a strong impact on the predictive power.

Finally, few comments must be done for the SOL model. The 2-point model is generally valid for different machines, but it is too simple in its physics description and not valid for

detached state and more complex exhaust scenarios. Moreover, the particle balance developed in this thesis presents many aspects which are machine-related. For example many processes described involve the wall material, which depends on the specific machine, and the divertor configuration, which affects the structure of the model itself by setting what are the regions in which the SOL should be splitted. Moreover, the diffusion coefficients and enrichment factors are derived heuristically, trying to reproduce experimental observations. Such dynamic could depend on the specific device. Therefore, in order to reproduce the SOL evolution for different devices, the parameters included in the model should be refitted and the topology should be changed according to the divertor configuration.

All the listed limitations reduce the predictive precision of the model. However, in the flight simulator there should be a hierarchy based on the validation first of the global parameters, then of the kinetic profiles for standard cases. Once such validation is provided, other pulses, where specific physics mechanisms affect the kinetic profiles or global parameters either in a small or pronounced way, should be validated. However, we believe that in many AUG discharges the limitations found in this thesis play a secondary role. Therefore, in such discharges the predictions given by our models should deviate only slightly from the reality, giving still a reasonable temporal evolution of the temperature profiles and the global parameters. Different is the situation for discharges with non-standard behaviour (e.g. advanced scenarios). Here the precise description of the profiles is challenging and important, because the local effects (e.g. ITB [14]) can play a crucial role in the determination of the global parameters and profiles evolution. Therefore, in order to broaden the validation power, starting from the models derived in this thesis, improvements related to more and more physics elements shall be added in the future.

7.1 Future development lines

Advances in both experimental and theory understanding of the tokamak plasmas allow to increase the complexity of our modeling tools. Despite the even more complex nature of the real system, we consider that the application of our models is finally showing that we are on the right path to have a comprehensive discharge simulation tool which delivers a realistic prediction of the pulse evolution. Constant validation of the physics models used in our simulators against experimental data is the key process that allows to gain confidence in our predictive capability, and leads to further improvement of the models themselves. A certain degree of validation has been proved even with some limitations which affect the predictive capability. After the improvement of the particle transport, the most immediate next step is to validate the models against more AUG discharges in a wide range of configurations. Once a broader validation on AUG is guaranteed, a long-term crucial plan is to test the models on different devices and extrapolate them to future machines (e.g. ITER and DEMO). To this purpose, the core model has a general validity and can easily be extrapolated. In fact, the only major assumption is the local transport.

Different is the situation for the edge and SOL models, where the assumptions made (e.g. fixed pedestal width, divertor configuration) are in principle not valid for all the devices. However, several improvements of all the models should be provided. These are listed in the following:

- in the core the most important development must be performed for the physics-based particle transport. For example, the particle pinch model could be obtained by adding more details and physical ingredients in the analytical formula used to fit the TGLF simulations. Moreover, the gas puff has been observed to play a role in the determination of the transport properties in the edge [127], through its effect on turbulence and background gradients. By including this effect in the edge model, it would be easier to predict the density evolution of L-modes or scenarios with strong gas puff;

- in the edge a possible improvement could be driven by the implementation of a model to predict the pedestal width;

- the SOL model needs to be more physically robust. This can be done by fitting the parameters in the model, which are now freely assigned (e.g. enrichment factors), on the values calculated in SOLPS simulations. Another possible improvement is the inclusion of the treatment of neutral particles and consequent prediction of different recycling regimes or detachment. Moreover, a different configuration of the divertor could be modeled by changing the zones in which the SOL is splitted. Finally, other improvements from which Fenix could benefit are the inclusion of additional dynamics of the SOL (e.g. MARFE or X-point radiator) and models of phenomena not directly related to turbulent transport (e.g. MHD activity).

The modularity of the models, which is related to the environment in which they are developed (i.e. ASTRA) and their structure (e.g. SOL particle balance topology), opens the possibility of a constant updating, including the developments discussed in the list.

Acronyms

AUG ASDEX Upgrade.

CXRS Charge Exchange Recombination Spectroscopy.

DCS Discharge Control System.

DN Double Null.

DP Discharge Program.

ECRH Electron Cyclotron Resonance Heating.

ELM Edge Localized Mode.

ETB Edge Transport Barrier.

ETG Electron Temperature Gradient.

FLR Finite Larmor Radius.

GP Gas Puff.

H-mode High Confinement Mode.

HFS High Field Side.

HFSHD High Field Side High Density Front.

I-mode improved confinenemt mode.

ICRH Ion Cyclotron Resonance Heating.

IDA Integrated Data Analysis.

ITB Ion Transport Barrier.

ITG Ion Temperature Gradient.

JET Joint European Torus.

KBM Kinetic Ballooning Mode.

L-mode Low Confinement Mode.

LCFS Last Closed Flux Surface.

LFS Low Field Side.

LSN Lower Single Null.

MARFE Multifaceted Asymmetric Radiation From the Edge.

MHD Magneto-Hydrodynamic.

MTM Micro Tearing Mode.

NBI Neutral Beam Injection.

NN Neural Network.

OMP Outer Mid-plane.

PBM Peeling Ballooning Mode.

PCSSP Plasma Control System Simulation Platform.

PFC Plasma Facing Component.

PFR Private Flux Region.

PID Partial Integrated Derivative.

SOL Scrape Off Layer.

SPI Shattered Pellet Injection.

TEM Trapped Electron Mode.

TGLF Trapped Gyro Landau Fluid.

USN Upper Single Null.

VTA Vertikale Thomsonstreuung Acqiris (Thomson scattering).

Bibliography

[1] P. Pasolini, Scritti Corsari, Garzanti (1975)

[2] V.S. Mukhovatov and V.D. Shafranov, Nuclear Fusion 11 605 (1971)

[3] U. Stroth et al., Nucl. Fusion 62 042006 (2022)

[4] M. Bernert et al., Nucl. Fusion 61 024001 (2021)

[5] ITER Physics Expert Group on Confinement and Transport et al., Nucl. Fusion 39 2175 (1999)

[6] A.C.C. Sips et al., Nucl. Fusion 58 126010 (2018)

[7] A. Ho et al., Phys. Plasmas 28, 032305 (2021)

[8] F. Janky et al., Fusion Engineering and Design, 163 112126 (2021)

[9] E. Fable et al., Plasma Physics and Controlled Fusion 64 044002 (2022)

[10] M. L. Walker et al., Fusion Engineering and Design Vol 89, Issue 5, 518-522 (2014)

[11] G. Raupp et al., Fusion Eng. Des. 84 (7–11) 1575–1579 (2009)

[12] R. D. Hazeltine and H. R. Strauss, The Physics of Fluids 21, 1007 (1978)

[13] W Horton, Reviews of Modern Physics 71.3, p. 735 (1999)

[14] R. C. Wolf, Plasma Phys. Control. Fusion 45 R1–R91 (2003)

[15] Houlberg W.A., Shaing K.C., Hirshman S.P. and Zarnstorff M.C., Phys. Plasma 4 3230 (1997)

[16] E. A. Belli and J. Candy, Plasma Physics and Controlled Fusion 50, 095010 (2008)

[17] C. Angioni and O. Sauter, Physics of Plasmas 7, 1224 (2000)

[18] O. Sauter, C. Angioni and Y. R. Lin-Liu, Phys. Plasmas 6, 2834 (1999)

[19] D. Fajardo et al., Plasma Phys. Control. Fusion 64 055017 (2022)

[20] C. Bourdelle et al., Physics of Plasmas 14.11, 112501 (2007)

[21] X. Garbet et al., Plasma Phys. Control. Fusion, 46(9):1351–1373, (2004)

[22] G. M. Staebler, J. E. Kinseya and R. E. Waltz, Phys. Plasmas 12, 102508 (2005)

[23] G. M. Staebler, Phys. Plasmas 14, 055909 (2007)

[24] P. Manz et al., Phys. Rev. Lett. 103, 165004 (2009)

[25] D. R. Smith et al., Physics of Plasmas 20.5, p. 055903 (2013)

[26] P Manz et al., Plasma Physics and Controlled Fusion 56.3, p. 035010 (2014)

[27] Z. Yan et al., Phys. Plasmas 18, p. 056117 (2011)

[28] Z. Yan et al., Phys. Rev. Lett. 107, p. 055004 (2011)

[29] A. Diallo et al., Phys. Rev. Lett. 112, p. 115001 (2014)

[30] D. Dickinson et al., Phys. Rev. Lett. 108, p. 135002 (2012)

[31] D Dickinson et al., Plasma Physics and Controlled Fusion 55.7, p. 074006 (2013)

[32] S. Saarelma et al., Nuclear Fusion 53.12, p. 123012 (2013)

[33] J.M. Canik et al., Nuclear Fusion 53.11, p. 113016 (2013)

[34] D.R. Hatch et al., Nuclear Fusion 55.6, p. 063028 (2015)

[35] D. P. Fulton et al., Physics of Plasmas 21.4, p. 042110 (2014)

[36] D. Told et al., Physics of Plasmas 15.10, p. 102306 (2008)

[37] F. Jenko et al., Physics of Plasmas 16.5, p. 055901 (2009)

[38] Weigang Wan et al., Phys. Rev. Lett. 109, p. 185004 (2012)

[39] D.R. Hatch et al., Nuclear Fusion 56.10, p. 104003 (2016)

[40] D.R. Hatch et al., Nuclear Fusion 57.3, p. 036020 (2017)

[41] M. Greenwald, Plasma Phys. Control. Fusion 44 R27-R53 (2002)

[42] H. Alfvén, Nature 150.3805, pp. 405–406 (1942)

[43] T. Ozeki et al., Nucl. Fusion 30 1425 (1990)

[44] A. Loarte et al., Journal of Nuclear Materials 266-269 587-592 (1999)

[45] A.B. Mihailovskii, Plasma Phys. Rep. 23.10, p. 844 (1997)

[46] M. Hoelzl et al., Nucl. Fusion 61 065001 (2021)

[47] T. Luda et al., Nucl. Fusion 60 036023 (2020)

[48] P. B. Snyder et al. , Phys. Plasmas 16, 056118 (2009)

[49] S. Wiesen et al., Journal of Nuclear Materials 415 S535–S539 (2011)

[50] D. A. D'Ippolito et al., Contrib. Plasma Phys. 44, No. 1-3, 205 – 216 (2004)

[51] D. Carralero et al., Nucl. Fusion 57 056044 (2017)

[52] F. Reimold et al., Nuclear Materials and Energy 12 193–199 (2017)

[53] I. Yu Senichenkov et al., Plasma Phys. Control. Fusion 61 045013 (2019)

[54] S. Potzel et al., Journal of Nuclear Materials 463 541–545 (2015)

[55] Y. R. Martin et al., J. Phys.: Conf. Ser. 123 012033 (2008)

[56] M. Schmidtmayr et al., Nucl. Fusion 58 056003 (2018)

[57] V. Rohde et al., Plasma Phys. Control. Fusion 51 124033 (2009)

[58] B. Lipschultz et al., Nucl. Fusion 24 977 (1984)

[59] S. Wiesen et al., Journal of Nuclear Materials 463 480-484 (2015)

[60] V. Rozhansky et al., Nucl. Fusion 49 025007 (2009)

[61] S. I. Braginskii, Transport processes in a plasma, in Reviews of Plasma Physics, ed. by M. A. Lontovich, Vol 1, pag. 205–311, Consultants Bureau, New York, (1965)

[62] S.I. Braginskii, in Review of Plasma Physics , ed. by M.A. Leontovich, Vol. 1., New York: Consultants Bureau, (1965), p. 214

[63] P. C. Stangeby, The Plasma Boundary of Magnetic Fusion Devices, ed. by CRC Press, Boca Raton (2000)

[64] P. C. Stangeby, Plasma Phys. Control. Fusion 60 044022 (2018)

[65] A. Kallenbach et al., Nuclear Materials and Energy 18 166-174 (2019)

[66] R. J. Goldston et al., Plasma Phys. Control. Fusion 59 055015 (2017)

[67] R. J. Goldston, M. L. Reinke, and J. A. Schwartz, Plasma Physics and Controlled Fusion 59.5, p. 055015 (2017)

[68] M. Siccinio et al., Plasma Phys. Control. Fusion 58 125011 (2016)

[69] R. Fischer et al., Fusion Science and Technology 58.2, pp. 675–684 (2010)

[70] B. Kurzan and H. D. Murmann, Review of Scientific Instruments 82.10, p. 103501 (2011)

[71] E. Viezzer et al., Review of Scientific Instruments 83.10, p. 103501 (2012)

[72] M. Reich et al., Europhysics Conference Abstracts, vol. 36F, p. PD4.004 (2012)

[73] C. Rapson et al., Proceedings of 27th SOFT Conference, Liege (2012)

[74] B. Esposito et al., Nucl. Fusion 51 (8) (2011)

[75] W. Treutterer et al., Fusion Engineering and Design 89 146–154 (2014)

[76] W. Treutterer et al., Fusion Engineering and Design 96–97 712–715 (2015)

[77] G. V. Pereverzev et al., IPP Report 5/42 (August 1991)

[78] E. Fable et al., Plasma Phys. Contr. Fusion 55, 124028 (2013)

[79] Ivanov et al., 32nd EPS Conf. on Plasma Physics vol 29C (ECA) P-5.063 (2005)

[80] G. Raupp, G. Ambrosino, G. DeTommasi, D.A. Humphreys, M. Mattei, G. Neu, et al., Proceedings of 9th IAEA Technical Meeting on Control, Data Acquisition, and Remote Participation for Fusion Research, pp. O1–O5 (2013)

[81] E. Poli, A. G. Peeters, and G. V. Pereverzev, Computer physics communications 136.1, pp. 90–104 (2001)

[82] M. Weiland et al., Nucl. Fusion 58 082032 (2018)

[83] M. Muraca et al., Plasma Phys. Control. Fusion 65 035007 (2023)

[84] B. Sieglin et al., Fusion Engineering and Design Vol 161, 111958 (2020)

[85] F. L. Hinton and R. D. Hazeltine, Rev. Mod. Phys. 48, 239 (1976)

[86] C. Angioni, Modelling of electron transport and of sawtooth activity in tokamaks (PhD thesis), (2001)

[87] F. Ryter et al., Nucl. Fusion 43 1396 (2003)

[88] F. Imbeaux et al., Plasma Phys. Control. Fusion 43 1503 (2001)

[89] J. E. Kinsey et al., Phys. Plasmas 13, 022305 (2006)

[90] J. Citrin et al., Plasma Phys. Control. Fusion 57 014032 (2015)

[91] Kyuho Kim et al., Phys. Plasmas 24, 062302 (2017)

[92] J. Li et al., Nucl. Fusion 60 126038 (2020)

[93] A. Di Siena et al., Nucl. Fusion 58 054002 (2018)

[94] K. H. Burrell, Physics of Plasmas 4, 1499 (1997)

[95] J. E. Kinsey et al., Phys. Plasmas 14, 102306 (2007)

[96] G.M. Staebler et al., Nucl. Fusion 57 066046 (2017)

[97] J.F.Drake and Y. C. Lee, Phys. Rev. Lett. 39 453 (1977)

[98] L. Chen, P. H. Rutherford and W. M. Tang, Phys. Rev. Lett. 39 460 (1977)

[99] W. Guttenfelder et al., Phys. Rev. Lett. 106, 155004 (2011)

[100] M. Erba et al., Nucl. Fusion38 1013 (1998)

[101] F. Jenko et al., Physics of Plasmas 8, 4096 (2001)

[102] A. G. Peeters et al., Phys. Plasmas 12, 022505 (2005)

[103] F. Jenko et al., Physics of Plasmas 7, 1904 (2000)

[104] Z. Lin and L. Chen, Phys. Plasmas 12, 056125 (2005)

[105] N. T. Howard et al., Physics of Plasmas 23, 056109 (2016)

[106] N. Bonanomi et al., Nucl. Fusion 58 124003 (2018)

[107] Z. Lin et al., Phys. Rev. Lett. 83, 3645 (1999)

[108] M. B. Isichenko, A. V. Gruzinov and P. H. Diamond, Phys. Rev. Lett. 74, 4436 (1995)

[109] D. R. Baker and M. N. Rosenbluth, Physics of Plasmas 5, 2936 (1998)

[110] B. Coppi and C. Spight, Phys. Rev. Lett. 41, 551 (1978)

[111] J. Weiland and H. Nordman , Physics of Fluids B: Plasma Physics 5, 1669 (1993)

[112] C. Angioni et al., Phys. Plasmas 16, 060702 (2009)

[113] H. Zohm, Plasma Phys. Control. Fusion38 105 (1996)

[114] A. W. Leonard, Physics of Plasmas 21, 090501 (2014)

[115] J. W. Connor et al., Physics of Plasmas 5, 2687 (1998);

[116] P. B. Snyder et al., Physics of Plasmas 9, 2037 (2002)

[117] J. Puchmayr, Optimization of Pedestal Stability on ASDEX Upgrade, IPP report (2020-11)

[118] M. G. Dunne et al., Plasma Phys. Control. Fusion, 59(2), 025010 (2016)

[119] P. A. Schneider et al. Plasma Phys. Control. Fusion 54 105009 (2012)

[120] P.A. Schneider et al. Nucl. Fusion 53 073039 (2013)

[121] A.E. Hubbard et al, Nucl. Fusion 52 114009 (2012)

[122] M. Cavedon et al., Nucl. Fusion 62 066027 (2022)

[123] J. Karhunen et al., Nuclear Materials and Energy 19 279-286 (2019)

[124] R. Dux et al., Journal of Nuclear Materials Vol 390–391, 858-863 (2009)

[125] E. Fable et al., J. Phys.: Conf. Ser. 260 012009 (2010)

[126] E. Fable et al., Plasma Phys. Control. Fusion 55 124028 (2013)

[127] C.U. Schuster et al., Nucl. Fusion 62 066035 (2022)

Acknowledgments

This work could have not been possible without the direct or indirect participation of many people. Therefore, I want to thank who made this PhD an exciting experience.
Thanks to Dr Emiliano Fable for the constant supervision of our work, the patience shown for the many questions that I raised, and its availability for discussions. Its fresh, young and innovative mind gave birth to ideas which were a crucial part of the entire work. Thanks to Dr Clemente Angioni, whose door has always been opened to clarifications, even for the most basic concepts, and the clear physical pictures explained during the frequent discussions. Thanks to Prof Dr Hartmut Zohm for showing the maximum possible respect to my activity, answering in short time to any mail, and supervising regularly the progress of the PhD. These 3 great and humble scientists made me understand how work can be a passion, more than a duty.
I want to thank also my colleagues for the constant stimulating discussions: thanks to Dr Maximilian Reisner, with whom I shared the office during the Corona-virus pandemic, and Dr Teobaldo Luda, for introducing me to the working environment, and being the spiritual guide of us all. Thanks to my office mates, in particular Dr. Nicola Bonanomi for the heritage of jimmy jagger and the frequent explosions at his desk, Daniel Fajardo, porque es un parcerito de la ..., Tabea Gleiter, for supervising us all as head of the office and Paul Heinrich, for his constant presence in the office. Thanks to Dr. Oleg Samoylov for the really complicated humour he shared with me. All these people made our office a respectful and friendly environment. Thanks to the entire ASTRA team, in particular Dr. Giovanni Tardini, who helped me to debug and understand the details of the code. Thanks to the Fenix team, in particular Dr. Pierre David, for helping me in the debugging. Thanks also to many other people, not less important as scientists, colleagues and friends. Thanks to Brando Rettino, for the pasta al tonno breakfast, quoting so many movies and spending so much precious time together, thanks to Dr. Davide Silvagni for being so kind and open-minded, thanks to Dr. Dominik Brida for his humour, his the italian vibes and for being the human being with the highest number of positive feedback to any social activity, thanks to Antonio Magnanimo, a.k.a il gigante ischitano, for the fastest sprints ever recorded during football matches, thanks to Dr. Balasz Tal, for his funny attitude and the melody of his sentences, thanks to Sergei Makarov, for being my third boss and moi brtella at the same time, thanks to Michael Bergmann for being so cool and swag, thanks to Daniel Hachmeister because he finally põe mais tabaco, thanks to Dr Francesco Vannini for the meditation in the control room, thanks to Dr Nathan De Oliveira for the scarpe

di gomma, thanks to Dr Riccardo Casagrande for the millepiedi he found in the englisher garten. Thanks to the entire Institute for sharing a really kind and pleasant environment. Thanks to the football team, which helped me to relax after many tiring working days.
Outside the institute, I want to thank all the friends who visited me: Matteo Calvani, Dr Riccardo Cocci, Claudio Cipriani, Mattia Visca, Danilo Zia and Ing Tommaso Carnicella. I also want to thank all the people I met in Munich with whom I became great friend in time: Jidong Lyu, Adam Ghazalin and Annalisa Polimeni.
Last, but not least, I want to thank who privately gave me support in these 3 years: Alessia Ciociola, Maurizio Muraca, Roberta De Nardin and Marina Muraca. It is hard to write down what I feel for you. Neither the best dream of a partner, a son and a brother could show what you mean to me. You are the best people I have ever met in my life. Thanks.